2016

Micro-electro-opto-fluidic systems for biomedical drug screening and electromagnetic filtering and cloaking applications

Peng Liu
Iowa State University

Micro-electro-opto-fluidic systems for biomedical drug screening and electromagnetic filtering and cloaking applications

by

Peng Liu

A dissertation submitted to the graduate faculty

in partial fulfillment of the requirements for the degree of

DOCTOR OF PHILOSOPHY

Major: Electrical Engineering

Program of Study Committee:
Liang Dong, Major Professor
Jaeyoun Kim
Santosh Pandey
Sumit Chaudhary
Jiming Song

Iowa State University

Ames, Iowa

2016

TABLE OF CONTENTS

ACKNOWLEDGMENTS

First of all, I would like to extend my deepest gratitude to my major professor, Dr. Liang Dong for his dedicated guidance, encouragement and patience from the first day I came here. Your support was essential to my research work.

I also would like to thank all other committee members, Dr. Jaeyoun Kim, Dr. Santosh Pandey, Dr. Sumit Chaudhary and Dr. Jiming Song for their guidance and inspiration throughout the course of this research.

I also would like to thank my friends, colleagues, and lab-mates. Without your help and support, I would not made all this happen.

In addition, I would like to acknowledge the funding sources of this work. This work was supported in part by the U.S. National Science Foundation under awards no. ECCS-1102354 and ECCS-0954765, and China Scholarship Council.

Lastly, I would like to thank my family for their unconditional love and support.

ABSTRACT

Microfluidic is a multidisciplinary field that deals with the flow of liquid inside micro-meter size channels. In order to be considered as microfluidics, at least one dimension of the channel should be in the range of one micrometer or sub-millimeter. Microfluidic technology includes designing, manufacturing, formulating devices and processing the liquid. As numerous bio-science and engineering techniques have utilized microfluidics and highly integrated with this remarkable technology, the microfluidic platform technology has extended to several sub-techs: micro-scale analysis, soft-lithography fabrication, polymer science and processing, on-chip sensing and micro-scale fluid manipulation. Those sub-techs have been developed rapidly along with the booming microfluidics.

The advance of those techniques has promoted microfluidic system diverse and widespread applications. Some examples that employ this technology include on-chip drug screening, micro-scale analysis, flexible electronics, biochemical assays. Many engineering field, such as optics, electronics, chemicals and electromagnetics, have been integrated with the microfluidic system to form a completed system for sensing, analyzing or realizing some specific applications.

Through the fusion of those technologies with microfluidics, many emerging technologies are well initiated, such as optofluidics and electrofluidics. Despite of rapid advancement of each parent technology field, those intersected technologies are still in their infancy and many technological elements and even some fundamental concepts are just now being developed. Thus, it provides great opportunity to explore more about those emerging technologies. Some particular areas that mainly interest researchers including cost deduction,

effective fabrication, highly integration, portability and applicability. Due to the wide and diversity nature of the microfluidic technology and numerous combinations from the integration with other fields, it is very difficult to choose a single aspect or particular subject to research. Hence, we would like to focus on the application orientated microfluidic techniques that integrated with other engineering areas, in particular optics and electronics. Correspondingly, I will present four microfluidic platforms that integrated with optics, electronics for different application purpose.

First of all, fiber-optics was integrated into a microfluidic device to detect muscular force generation of microscopic nematodes. The integrated opto-fluidic device is capable of measuring the muscular force of nematode worms normal to the translational movement direction with high sensitivity, high data reliability, and simple device structure. The ability to quantify the muscular forces of small nematode worms will provide a new approach for screening mutants at single animal resolution.

Secondly, electronic grids were integrated into a microfluidic chip to realize on-chip tracking of nematode locomotion. The micro-electro-fluidic approach is capable of real-time lens-less and image-sensor-less monitoring of the locomotion of microscopic nematodes. The technology showed promise for overcoming the constraint of the limited field of view of conventional optical microscopy, with relatively low cost, good spatial resolution, and high portability.

Thirdly, electromagnetic spit ring resonator (SRR) structure was adopted as microfluidic channel filled with liquid metal to fabricate a tunable microfluidic microwave electronics called meta-atom. The presented meta-atom is capable of tuning its electromagnetic (EM) response characteristics over a broad frequency range via simple mechanical stretching. The meta-atom in

this study presents a simple but effective building block for realizing mechanically tunable metamaterials.

Finally, based on the meta-atom we previously developed, an array of electromagnetic SRR shaped microfluidic channels filled with liquid metal to form a flexible metamaterial-based microwave electronic “skin” or meta-skin. When stretched, the meta-skin performs as a tunable frequency selective surface with a wide resonance frequency tuning range. When wrapped around a curved dielectric material, the meta-skin functions as a flexible “cloaking” surface to significantly suppress scattering from the surface of the dielectric material along different directions.

The microfluidic platform will find great applications when it integrates with other technologies. The development of such integration will greatly intersect different research areas and benefit all of the intersected technologies and fields, thus broadening the future applications.

CHAPTER 1

GENERAL INTRODUCTION

1.1 Introduction

Microfluidics is a generalized technology rooted from microelectronics, intersecting engineering, physics, biochemistry, chemistry with practical application in many research areas. As the name states, the technology initially is design to process low volumes of fluidic to fulfill certain applications. To be considered as microfluidics, at least one dimension of the channel should be in the range of one micrometer or sub-millimeter [1]. Several core sub-techniques have been developed rapidly along with this emerging micro-fluidic field, such as soft-lithography fabrication, polymer science and processing, on-chip sensing and micro-scale fluid manipulation [2].

Soft lithography refers to a fabrication technique or strategy based on printing, molding and embossing with elastomeric materials. It has several advantages over conventional photo lithography, including lower cost, bio-compatible, flexible substrate, experimentally convenient and thus is well suited in microfluidics, biological application, flexible and tunable electronics, applications involve curved structures [3, 4]. The advance of soft lithography has transformed microelectronics.

Thanks to soft lithography, many polymers, such as Polydimethylsiloxane (PDMS), Poly(methyl methacrylate) (PMMA) and Polybutyrate (PBAT or Ecoflex), have replaced traditional semiconductor substrate (silicon, glass) in many microfluidic platforms [1]. There are two major factors to consider when choosing a material for a microfluidic platform: degree of integration and application requirement. Several material characteristics that may

be important when choosing a material such as: electrical property, bio compatibility, optical transparency and flexibility. PDMS is the most common microfluidic substrate for academic experimental use due to its reasonable cost, ease of implementation and mature processing protocol. Recently, another elastomer Ecoflex has drawn great attention to researchers due to its super elasticity and flexibility. It is a great alternative elastomer where the applications require higher flexibility [2].

On-chip sensing is a technique that integrate on-chip sensors with microfluidic platforms for various applications [5]. Many sensing techniques have been successfully integrated with microfluidics, including optical detection [6], electrochemical detection [7], acoustic detection [8], mass spectrometry and etc. [9]. Among them, optical and electrochemical methods are most commonly used. Optical methods have several advantages such as great sensitivity, contactless with analyte and transplantable for different objects. While electrochemical detection is great for miniaturization, portability and low-cost applications. Conductivity, amperometry and potentiometry are the most commonly used characteristics in electrochemical detection [10].

Micro-scale fluid manipulation is another important branch of microfluidic technology. Pumping, valves, and mixing are three essential elements of fluid manipulation. Integration of micropumps into the system can reduce the dead volumes from the interface with external pumps [11,12]. Valves are the core components of controlling and directing the movement of the fluid [12]. On-chip mixers are needed in favor of thorough and rapid mixing of different fluid [13,14].

The microfluidics has been developing substantially with applications intersecting across multiple fields and disciplines. The multidisciplinary nature of microfluidics demands

continued coordination between different engineering fields, in order to achieve its full potential. Several emerging technology areas have been well initiated and the most popular two are optofluidics and electrofluidics [10, 15]. As their name imply, each technology is created by the fusion of two technologies.

Optofluidics is combing the advantages of both optics and microfluidics to enable the simultaneous delivery of light and fluidics with microscopic precision. Two research directions both show great promising to solidify into the new field optofulidics. One is incorporating optical elements into microfluidic system, in which light manipulates fluid, to achieve fast and accurate sensing or manipulating of fluidic. The other direction is to use microfluidic elements as fundamental part of photonic device, where fluid manipulates light. Both of these two concepts outline a wide application of optofludics include smart display, biosensors and sustainable energy [10, 16].

Electrofludics is a new research field with a focus on the interaction in microfluidic and electronics. Similar to optofluidics, there are two research directions as well for electrofludics and both are shown great potential to advance the emerging field electrofludics. By integrating electronic device into microfluidic system, it opens up wide opportunity for on-chip sensing, actuation and fluidic manipulation. On the other hand, thanks to the introduction of high conductivity liquid metals with low toxicity, introducing microfluidic technique into electronics have been adopted and further developed to various devices such as wearable electronics, liquid transistors, stretchable RF antenna and flexible metamaterials [15, 17].

Despite the great progress that has been made in their parent fields, those intersected technologies are still in their infancy and many technological elements and even some

fundamental concepts are just now being developed. Thus, it provides great opportunity for us to explore more about those emerging technologies.

1.2 Literature Review of Current Technologies

Since the two concepts are introduced, they have gained considerable attention because of their great potential in many applications. Opportunity along with the problems are raised by many researchers. This part details several state-of-art concepts, techniques and applications of optofluidics and electrofluidics. Those work will be described in 4 sub categories as we discussed above: 1.Optofluidics with optics added to microfluidic systems, 2. Optofludics with fluidics added to microoptic systems, 3. Elecrofludics with electronics added to microfluidic systems, and 4. Electrofluidics with fluidics added to electronic systems. Of course, the present work may not only combine just two technologies, they may be mingled with each other: electro-optofluidics or integrated with other technologies, such as mechanical, thermal, acoustics, etc.

1.2.1 Optofluidics with optics added to microfluidic systems

With optical elements integrated into microfluidic, mostly in sensing and actuating parts, many novel compact and dense integrated optofluidic devices were developed. The fluid and particle manipulations can be improved by several optical techniques: optical tweezers [18-20], optically induced microfluidic field [21,22], near-field evanescent field [23,24]. Fig. 1.1 shows a novel fluidic manipulation method with photothermal effect. By illuminating photothermal nanoparticles (PNPs) inside the fluid near the liquid-air interface, heat is generated and evaporates the surrounding liquid. The vapor in the colder air condenses and droplets form very close to or even in contact with the interface. The droplet

then coalesce with each other and merge with the original liquid body due to the surface tension gradient and extend its contact line [22].

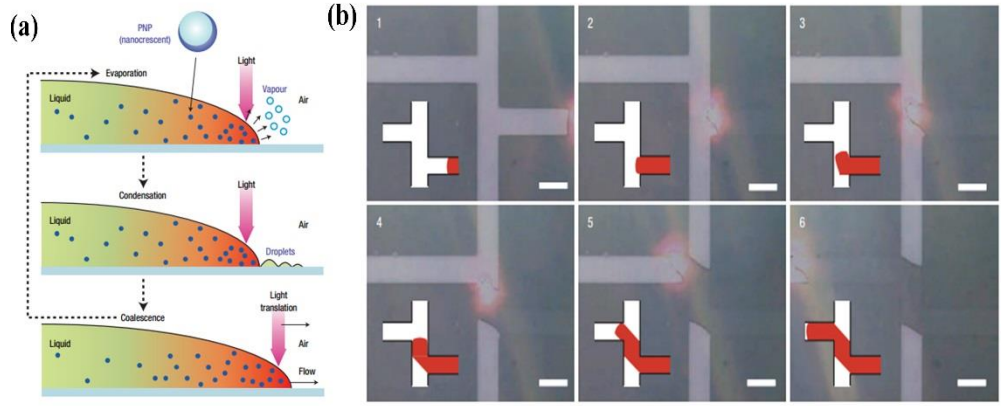

Fig. 1.1 (a) The principle of optically controlled advance of the liquid-air interface (b) The optically guided fluidic into left channel after two sharp turns (Reprinted by permission from Macmillan Publishers Ltd: [Nature Material] (ref 22). Copyright (2006)).

While in the sensing system of microfluidic platform, couple and integrate optical components into microfluidic devices are great to achieve sensitivity and scalability to smaller dimensions compare to other detection methods. The typical optical detection methods used in the microfluidic system are monitoring light properties including fluorescence [25,28], absorbance [26,28] and transmittance [27]. These methods usually involve techniques including fiber optics [27], evanescent waves [28] and optical waveguide [29]. A biomimetic mass-flow transducer producing responses in the form of optical pulse train was developed by Lee and her colleagues and shown in Fig. 1.2. By integrating one optical fiber cantilever with multiple polymer optical waveguides on a microfluidic platform, a pulse train can be generated by the mass-flow deflecting the optical fiber cantilever. The flow rate can be obtained by decode the pulse trains signal [27].

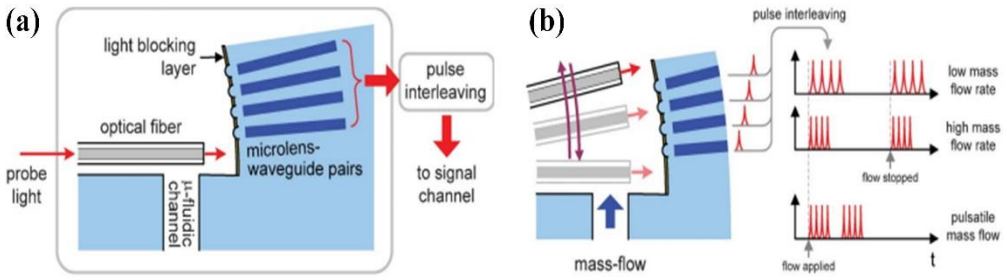

Fig. 1.2 (a) A schematic diagram of the optofluidic mass-flow transducer (b) When the mass-flow comes in, the fiber cantilever deflects and scan the waveguide array, generating pulse train depending on the scan speed and mass-flow strength (Reproduced from ref [27]. Copyright [2006] with permission of The Royal Society of Chemistry).

1.2.2 Optofluidics with fluidics added to microphotonic system

Microfluidic techniques are capable of providing tunability and flexibility to many photontic devices such as liquid waveguide [30], liquid lenses [31,32] and optofluidic lasers [33,34]. Wolfe et al. [30] reported a novel optical waveguide with both the light-guiding and cladding structures are liquid flowing in microchannels fabricated in PDMS. The major advantage of this device is the level of reconfigurability that solid-state waveguide can hardly obtain. The great reconfigurability can be achieved by several methods: easily adding dopants to control optical properties; switching between single-mode and multi-mode by modulating the size of the liquid core; switching the optical path by controlling the liquid streams. Fig. 1.3 shows the design and images of the liq/liq waveguide.

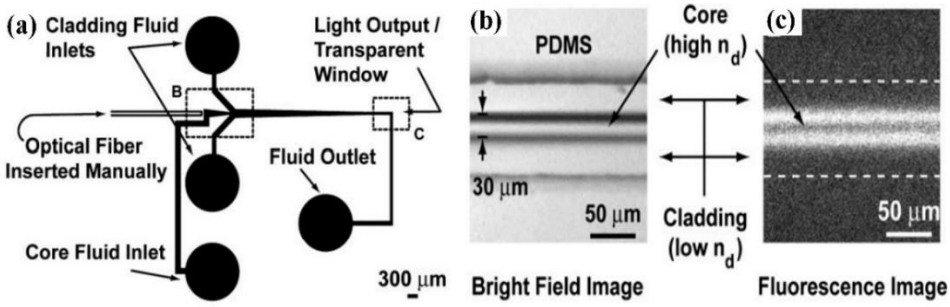

Fig. 1.3 (a) Diagram of the design of a microfluidic channel used in these experiments (b) Optical micrograph of the waveguide (c) Fluorescence micrograph of the same region of the channel as in (b) (from ref [30]. Copyright [2004] National Academy of Sciences).

Fig. 1.4 shows an adaptive liquid microlens developed by Dong et al. The basic design consists of a stimuli-responsive hydrogel ring placed within a microfluidic system. When exposed to an appropriate stimulus, the hydrogel ring responds by expanding or shrinking, owing to the absorption or release water, this leads to a curvature change of the water droplet located in the middle of the ring. By selecting different hydrogels, the lens can respond to different stimulus which could be PH, temperature, light and so on [32].

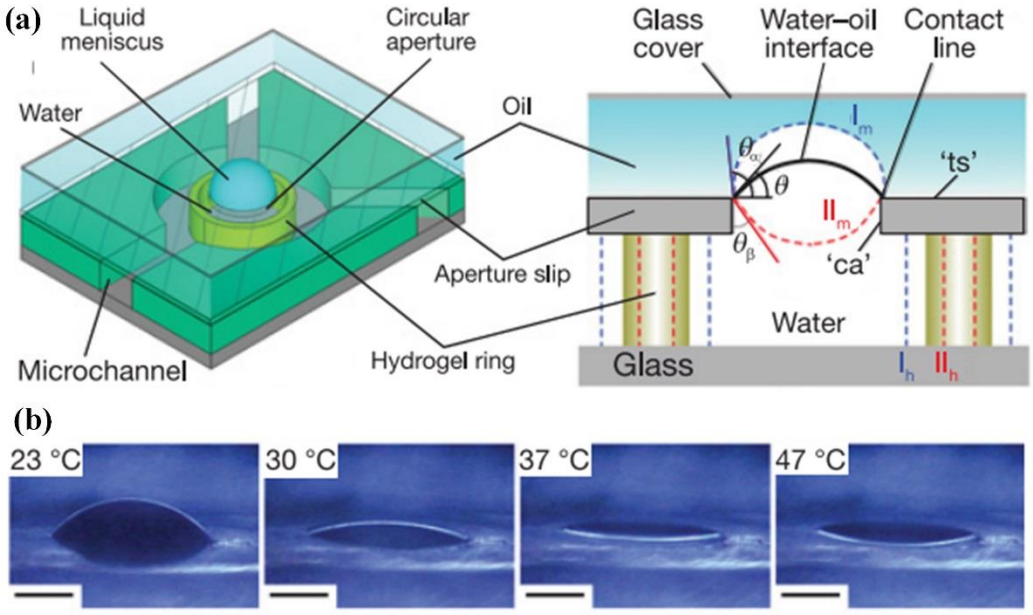

Fig. 1.4 (a) Diagram of the design and mechanism of the smart microlens using a pinned liquid-liquid interface (b) The shape of the liquid microlens varies with local environmental temperature (Reprinted by permission from Macmillan Publishers Ltd: [Nature] (ref 32). Copyright (2006)).

1.2.3 Electrofludics with electronics added to a microfluidic system

Electronics have been integrated into microfluidic system for decades. Similar to adding optics into microfluidic system, manipulating fluid and sensing are the two main constraints to further reduce the size of the microfluidic device. The most common electronic technique in manipulating fluidic includes electrochemical methods [35], electrostatic

actuation [36], electrowetting [37] and electrophoresis [38]. Pollack et al. [37] developed an electrowetting-based actuator of liquid droplets for microfluidic applications. Microactuation is achieved by direct electrical control of surface tension (wetting property) via two opposing planar electrodes. Fig 1.5 shows the scheme and the video frames of the working device.

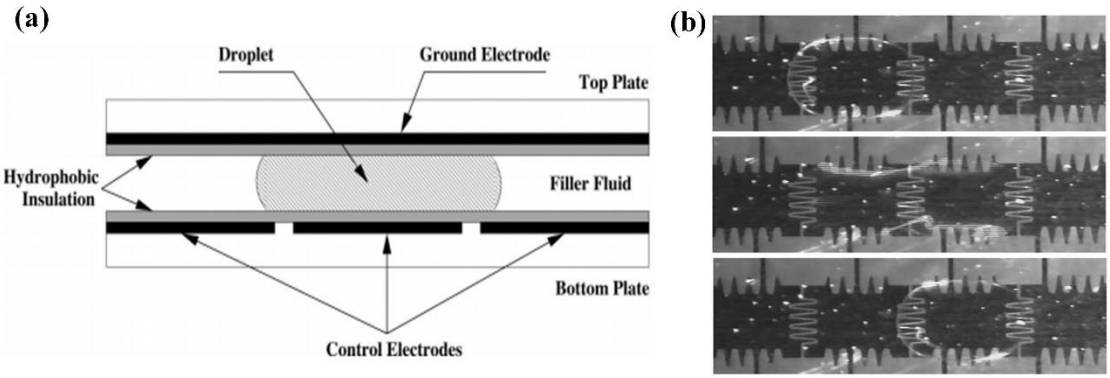

Fig. 1.5 (a) Schematic cross-section view of the electrowetting microactuator (b) Video frames of a moving droplet actuated by applying potential on the electrodes underneath the droplet (Reprinted with permission from ref [37]. Copyright [2000], AIP Publishing LLC.).

With the miniaturized manipulation parts placed on the microfluidic device, people developed several on-chip detectors for read-out and better integration. Amperometric detector [39,40], voltammetric detector [41], impedance detector [42] and conductivity detector [38] are the most popular ones. Fig. 1.6 shows a pioneer work of integrating conductivity detector into electrophoresis microfluidic system. It was developed in 2002 by Gallway et al with ease of integration and relatively simple and quick fabrication technique [38]. The conductivity detector consisted of a pair of platinum wires situated within the fluidic channel. Once the analyte enters the detection region, the pair of electrodes will contact with the analyte and read out the conductivity information.

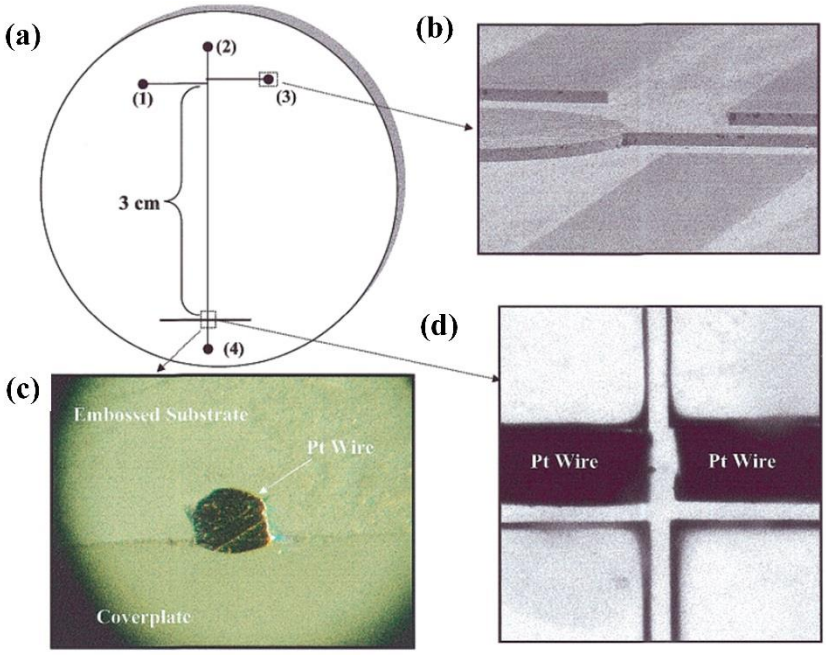

Fig. 1.6 (a) Schematic view of PMMA-based microchip with integrated conductivity detector (b) SEM near the waste reservoir (c) Optical micrograph of PMMA microfluidic chip that was assembled with a coverplate and electrodes and then cut down the center of the fluidic channel (d) Optical micrograph of the conductivity detector integrated to the PMMA microfluidic device (Reprinted with permission from ref [38]. Copyright (2002) American Chemical Society).

1.2.4 Electrofluidics with fluidic added to electronic system

Conductive material is essential in electronic system. In traditional microfluidics, ionic solutions are the most common liquid conductors that we have dealt with. However, poor electrical property may be caused by its relative low conductivity. Mercury is a well-known liquid metal with high conductivity. However, due to its high toxicity, it was not considered as a suitable material. Recently, the gallium-based alloys (Galinstan and EGaIn) stand out due to their low toxicity, non-reactive, liquid state in quite a broad temperature. Many liquid-state electronic devices have been developed using microfluidic platform technology including: transistors [43,44], capacitor [45], heterojunction sensors [46], wireless strain sensors [47], interconnector [48], switches [49] and radio-frequency electronics [50-52]. With the booming interest of microfluidic based liquid metal electronics,

conventional fabrication techniques with serial injection of liquid lacks of reliability and high throughput. Many advanced fabrication processes have been developed to take the especial care of viscous liquid metal such as direct writing with roller-ball pen [53], printing [54,55] and tape transfer [56].

Fig. 1.7 shows a schematic illustration and optical micrograph of a stretchable microfluidic radiofrequency antenna. The antenna consisted of liquid metal (EGaIn) enclosed in elastomeric microfluidic channels. A structurally simple half-wave antenna design was adopted to demonstrate the concept. The resonance frequency of the antenna was able to be reconfigured from 1.53 GHz to 0.738 GHz as the antenna was stretched [52].

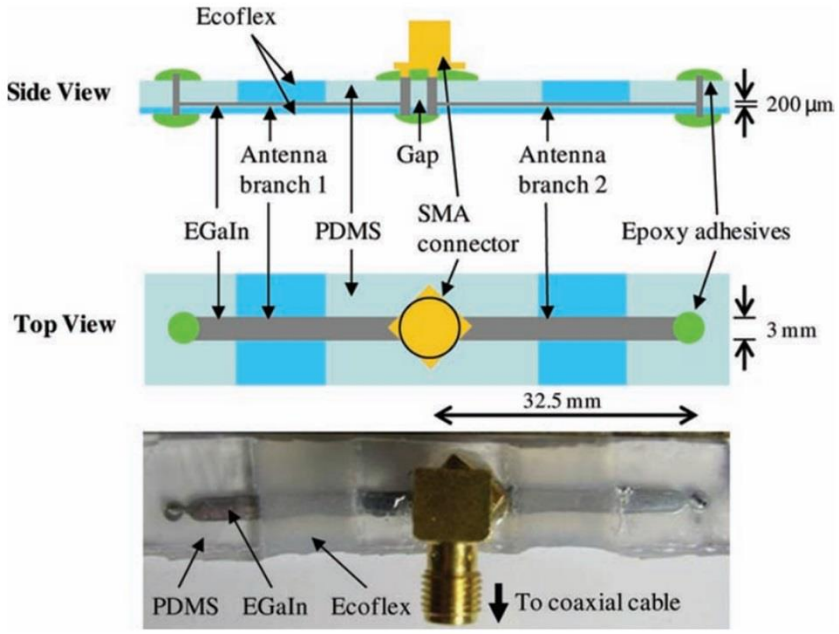

Fig. 1.7 Schematic illustrations and optical micrograph of the stretchable antenna (Reprinted with permission from ref [52]. Copyright (2010) John Wiley & Sons, Inc).

A novel fabrication technique with direct writing of liquid metal using a roller-ball pen was developed by Zhen et al. [53]. This paper demonstrates the feasibility of directly and

instantly writing out various conductive structures on flexible polymer substrate with the room temperature liquid metal.

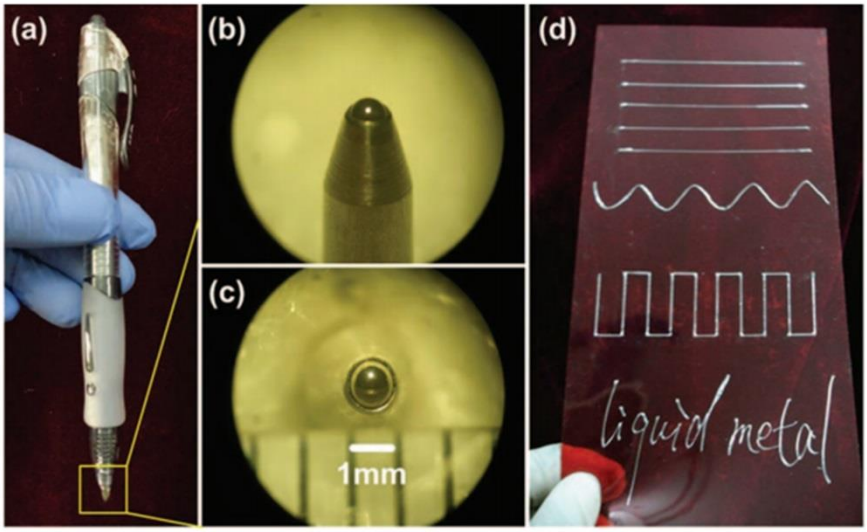

Fig. 1.8 (a) Optical image of a roller-ball pen loaded with liquid metal ink (b) and (c) Optical image of the side and top views of the pen tip (d) The conductive track written by the roller-ball pen (Reused from ref [53], 2013, used in accordance with the Creative Commons Attribution (CC BY) license).

With inclusion of liquid metal as active components has opened up new ways to realize flexible electronics. The development of the fabrication process dealt with liquid metal will dramatically accelerate the progress of integrating fluid into electronics.

The following table summarizes the state of the art devices and applications of micro-electro-opto-fluidic systems.

Table 1. State of The Art Devices and Applications

Device/Application	**Category**	**Integration technique and purpose**
Microfluidic sorting in an optical lattice [20]	Optofluidics with optics added to a microfluidic system	On-chip separating/ sorting nanoparticles by refraction of index using optical tweezers

Table 1 continued

Optofluidic control using photothermal nanoparticles[22]	Optofluidics with optics added to a microfluidic system	On-chip controlling and guiding the fluid flow using photothermal effect
Optical manipulation of nanoparticles and biomolecules [23]	Optofluidics with optics added to a microfluidic system	On-chip trapping and transporting of nanoparticles using near-field evanescent field
Temperature measurement using a temperature dependent dye [25]	Optofluidics with optics added to a microfluidic system	On-chip temperature measurement using a temperature dependent fluorescence dye
Optofluidic mass-flow transducer [27]	Optofluidics with optics added to a microfluidic system	On-chip mass-flow sensor using waveguide array to scan the deflection of fiber cantilever by measuring the transmittance
Multifunctional nanowire evanescent wave optical sensors [28]	Optofluidics with optics added to a microfluidic system	On-chip detecting molecules in solution with nanowire using optical absorbance
Liquid-core/liquid-cladding optical waveguides [30]	Optofluidics with fluidics added to microphotonic system	Tunable liquid optical waveguide with liquid stream as the core and cladding layer
Adaptive liquid micro-lenses [32]	Optofluidics with fluidics added to microphotonic system	Tunable micro liquid lenses with liquid as the lenses medium activated by stimuli-responsive hydrogel
Single mode optofluidic distributed feedback dye laser [33]	Optofluidics with fluidics added to microphotonic system	Optofluidic light source that employ fluids as the gain medium
Electrochemical principles for active control of liquids on submillimeter scales [35]	Electrofludics with electronics added to a microfluidic system	On-chip pumping and positioning of liquids using electrochemical methods

Table 1 continued

Electrowetting-based actuation of liquid droplets [37]	Electrofludics with electronics added to a microfluidic system	On-chip actuation and transportation of liquid droplets using electrowetting methods
Contact conductivity detection for analysis of mono- and polyanionic molecules [38]	Electrofludics with electronics added to a microfluidic system	On-chip separation of molecules using electrophoresis and on-chip detection using on-chip conductivity detector
Duel-electrode amperometric detection for electrophoresis microchip [39]	Electrofludics with electronics added to a microfluidic system	On-chip separation of molecules using electrophoresis and on-chip detection using on-chip amperometric detector
Cell-impedance sensing for monitoring single cancer cell migration [42]	Electrofludics with electronics added to a microfluidic system	Monitoring single cancer cell using integrated electrical cell-impedance sensing
Tunable organic microfluidic transistors [43]	Electrofluidics with fluidic added to electronic system	Tunable organic transistor that employ conducting fluidic as source and drain electordes
Highly deformable liquid-state heterojunction sensors [46]	Electrofluidics with fluidic added to electronic system	Fabrication of liquid-liquid ‘heterojunction’ sensors by choosing different sensing liquid
Stretchable microfluidic radiofrequency antennas [47]	Electrofluidics with fluidic added to electronic system	Stretchable and tunable microfluidic antenna that employ liquid metal as active material embedded in a microfluidic channel

1.3. Problems to be Solved

1.3.1 Drug screening based on nematodes using micro-electro-opto-fluidic systems

Parasitic nematodes remain a major problem in many area of the world because they cause disease in plants, animals and human. Control of these infections rely on regular chemotherapy. However, resistance developed to certain drugs can reduce the strength and effect of that drug thus has become the major threat to the production and wellness of animals and plants. Screening drug resistance of parasites is necessary for limiting spread of parasites and useful for discovery new drugs. The conventional method for detection of drug resistance is mesh system. The worms resistant to a certain anthelmintic are able to move through the mesh, whereas the sensitive worms are restricted. By counting the percentage of worms that were inhibited by the anthelmintic drug, one can get the information of the drug resistance. The disadvantage of the mesh system includes low resolution and low throughput. Currently, a lack of information on physiological changes of parasitic nematodes that occurred with drug resistance has prevented the development of successful molecular biology assays. A deep screening for drug sensitivity is urgently desired for monitoring the characteristic changes in the phenotypes of locomotion, muscular force and electrophysiological signals. The advantages of micro-electro-opto-fluidic system provide the potential of addressing the drawbacks of present mesh system and help to correlate any change in phenotype associated with resistance [57, 58]. My work focuses on developing deep drug screening platforms for monitoring two phenotype changes in locomotion and muscular force in a cost effective, reliable and simple way with the advanced micro-electro-opto-fluidic system.

1.3.2 Tunable and flexible microwave metamaterials using micro-electro-fluidic systems

Flexible electronics have gained considerable attention because of their potential application in artificial skins, flexible displays, wearable sensors, sustainable energy, etc. On the other hand, EM metamaterials have been intensively studied because they possess intriguing properties that can be hardly found in natural materials, such as negative permittivity, negative refractive index and index close to zero. Those unique properties allow metamaterials to be employed in many emerging applications such as sub-wavelength resolution imaging, filtering, and cloaking. And if the response characteristics are dynamically tunable, these devices will become more useful when adapting to different applications [59, 60]. Thus designing and fabricating devices that combine the advantages of flexible electronics and tunable metamaterials are important and will find many applications in frequency tuning, shielding and cloaking on curved surfaces. Liquid metal is a perfect bridge to connect the electronics with microfluidic platform technology. My work focuses on designing and fabricating flexible tunable microwave metamaterials with simple tuning mechanism using micro-electro-fluidic system.

1.4 Challenges and Approaches

So far, we have discussed the increasing interests and needs for integration of microfluidic technology with optics and electronics and two main problems that we focused on. Many challenges remain in this area. They require more efforts to dig deeper to solve them and provide great opportunities for researchers as well. The main challenges are cost deduction, integration improvement, easier fabrication, increase applicability, and pursuant of flexible and tunable electronics. All the challenges are impossible to be solved with one

simple technique, and usually, some features are sacrificed to improve others for application purpose. Therefore it is difficult to discuss the approaches solely without considering the application requirements. For all four application-orientated microfluidic platforms that will be presented later, I will discuss the challenges and approaches separately from the application point of view for each of them.

1) The current technology for measuring muscular force uses complicated strain gauge structure, or can't detect dynamic force of a worm in motion, or requires a high resolution microscope with automated stage. We developed a microfluidic device integrated with fiber optics is capable of measuring muscular force with high sensitivity. The simple and easy design of the structure is the key approach to achieve the ease of fabrication, high integration and improved applicability. Chapter 2 will detail the design, fabrication and results.

2) The optical microscopic imaging technique is essential for observing and extracting movement and locomotion information from live nematodes. Almost all of the existing technologies essentially utilize optical effects, such as shadow and interference patterns due to the presence of microorganisms, and thus, inevitably require a sophisticated imaging sensor chip, along with a light source for observation. We developed a micro-electro-fluidic device with low cost, simple architecture and high portability. The device consists of two identical linear array of thin-film microelectrodes that doesn't require any lens and image-sensors. Chapter 3 will detail the theory, fabrication, results and discussion.

3) While existing tunable metamaterial technologies have led to significant improvement toward broadening dynamic tuning ranges, there is still much room for

improvement such as simplifying tuning mechanism, extending tuning range and making device flexible enough to comply with surface irregularities on the underlying substrate. Thanks to liquid metal and microfluidic technique, we developed a novel stretchable meta-atom with liquid metal embedded in microfluidic SRR shaped channel. The meta-atom is capable of tuning its EM response over a broad frequency range via simple mechanical stretching. Chapter 4 will detail the theory, design, fabrication, results and discussion.

4) Although we successfully developed a stretchable meta-atom, it is impossible to use the meta-atom as filter or cloaking due to its small size. With the experience of developing stretchable meta-atom, we further improved our fabrication techniques to realize large-scale fabrication. Thus a wearable meta-skin with tunable frequency selective and cloaking effects was developed. The large-scale meta-skin consists of an array of meta-atoms fabricated with liquid metal injected within microfluidic channels. Chapter 5 will detail the design, fabrication, results and discussion.

1.5 Thesis Organizations

The following chapters are an accumulation of four published journal papers of which I am the primary author.

Chapter 2 describes development of an integrated fiber-optic microfluidic device for measuring muscular force of small nematode worms with high sensitivity, high data reliability and simple device structure. It is a great example of efficiently integrating optical elements into microfluidic platform with a great demonstration of application. The paper “An

integrated fiber-optic microfluidic device for detection of muscular force generation of microscopic nematodes" is published in *Lab on a Chip,* **12**, 2012.

Chapter 3 illustrates the development of a lens-less and image-sensor-less micro-electro-fluidic approach for real-time monitoring of the locomotion of microscopic nematodes. It is a great example of integrating electronics into microfluidic platform. The integration shows promise for overcoming the constraint of the limited field of view of conventional method, with low cost, good resolution and high portability. The paper "Micro-electro-fluidic grids for nematodes: a lens-less, image-sensor-less approach for on-chip tracking of nematode locomotion" is published in *Lab on a Chip,* **13**, 2013.

Chapter 4 presents a new type of tunable meta-atom in the x-band frequency range towards reconfigurable metamaterials. The meta-atom uses a liquid metal based split-ring resonator as its core constituent embedded in a highly flexible elastomer with simple tuning mechanism and high flexibility. It is a great example of adding fluidic to electronic device. The paper "Tunable meta-atom using liquid metal embedded in stretchable polymer" is published in *Journal of Applied Physics*, **118**, 2015.

Chapter 5 reports a flexible metamaterial-based "skin" or meta-skin with tunable frequency selective and cloaking effects in microwave frequency regime. The meta-skin is composed of an array of meta-atoms. It is a great example showing the advantage of microelectronics made with fluidic using microfluidic platform and technology. The paper "From Flexible Meta-Atom to Metamaterial: A Wearable Microwave Meta-Skin with Tunable Frequency Selective and Cloaking Effects" is published in *Scientific Report,* **6**, 2016.

Finally, the conclusion and future aspects will be summarized in Chapter 6.

1.6 References

1 Mark, D., Haeberle, S., Roth, G., von Stetten, F. & Zengerle, R. Microfluidic lab-on-a-chip platforms: requirements, characteristics and applications. *Chemical Society Reviews* **39**, 1153-1182, doi:10.1039/b820557b (2010).

2 Nge, P. N., Rogers, C. I. & Woolley, A. T. Advances in Microfluidic Materials, Functions, Integration, and Applications. *Chemical Reviews* **113**, 2550-2583, doi:10.1021/cr300337x (2013).

3 Qin, D., Xia, Y. & Whitesides, G. M. Soft lithography for micro- and nanoscale patterning. *Nature Protocols* **5**, 491-502, doi:10.1038/nprot.2009.234 (2010).

4 Xia, Y. N. & Whitesides, G. M. Soft lithography. *Annual Review of Materials Science* **28**, 153-184, doi:10.1146/annurev.matsci.28.1.153 (1998).

5 Lee, H., Xu, L., Koh, D., Nyayapathi, N. & Oh, K. W. Various On-Chip Sensors with Microfluidics for Biological Applications. *Sensors* **14**, 17008-17036, doi:10.3390/s140917008 (2014).

6 Kuswandi, B., Nuriman, Huskens, J. & Verboom, W. Optical sensing systems for microfluidic devices: A review. *Analytica Chimica Acta* **601**, 141-155, doi:10.1016/j.aca.2007.08.046 (2007).

7 Dungchai, W., Chailapakul, O. & Henry, C. S. Electrochemical Detection for Paper-Based Microfluidics. *Analytical Chemistry* **81**, 5821-5826, doi:10.1021/ac9007573 (2009).

8 Abd Rahman, M. F., Nawi, M. N. M., Abd Manaf, A. & Arshad, M. R. Characterization of Microfluidic-Based Acoustic Sensor for Immersion Application. *Ieee Sensors Journal* **15**, 1559-1566, doi:10.1109/jsen.2014.2363680 (2015).

9 Wang, X. *et al.* Microfluidics-to-mass spectrometry: A review of coupling methods and applications. *Journal of Chromatography A* **1382**, 98-116, doi:10.1016/j.chroma.2014.10.039 (2015).

10 Psaltis, D., Quake, S. R. & Yang, C. Developing optofluidic technology through the fusion of microfluidics and optics. *Nature* **442**, 381-386, doi:10.1038/nature05060 (2006).

11 Weibel, D. B., Siegel, A. C., Lee, A., George, A. H. & Whitesides, G. M. Pumping fluids in microfluidic systems using the elastic deformation of poly(dimethylsiloxane). *Lab on a Chip* **7**, 1832-1836, doi:10.1039/b714664g (2007).

12 Unger, M. A., Chou, H. P., Thorsen, T., Scherer, A. & Quake, S. R. Monolithic microfabricated valves and pumps by multilayer soft lithography. *Science* **288**, 113-116, doi:10.1126/science.288.5463.113 (2000).

13 Lee, C.-Y., Chang, C.-L., Wang, Y.-N. & Fu, L.-M. Microfluidic Mixing: A Review. *International Journal of Molecular Sciences* **12**, 3263-3287, doi:10.3390/ijms12053263 (2011).

14 Mansur, E. A., Ye, M., Wang, Y. & Dai, Y. A state-of-the-art review of mixing in microfluidic mixers. *Chinese Journal of Chemical Engineering* **16**, 503-516, doi:10.1016/s1004-9541(08)60114-7 (2008).

15 Lee, C. H. *et al.* Materials and Wireless Microfluidic Systems for Electronics Capable of Chemical Dissolution on Demand. *Advanced Functional Materials* **25**, 1338-1343, doi:10.1002/adfm.201403573 (2015).

16 Erickson, D., Sinton, D. & Psaltis, D. Optofluidics for energy applications. *Nature Photonics* **5**, 583-590, doi:10.1038/nphoton.2011.209 (2011).

17 Wu, Z., Hjort, K. & Jeong, S. H. Microfluidic Stretchable Radio-Frequency Devices. *Proceedings of the Ieee* **103**, 1211-1225, doi:10.1109/jproc.2015.2395716 (2015).

18 Grier, D. G. A revolution in optical manipulation. *Nature* **424**, 810-816, doi:10.1038/nature01935 (2003).

19 Ashkin, A., Dziedzic, J. M., Bjorkholm, J. E. & Chu, S. OBSERVATION OF A SINGLE-BEAM GRADIENT FORCE OPTICAL TRAP FOR DIELECTRIC PARTICLES. *Optics Letters* **11**, 288-290, doi:10.1364/ol.11.000288 (1986).

20 MacDonald, M. P., Spalding, G. C. & Dholakia, K. Microfluidic sorting in an optical lattice. *Nature* **426**, 421-424, doi:10.1038/nature02144 (2003).

21 Chiou, P. Y., Ohta, A. T. & Wu, M. C. Massively parallel manipulation of single cells and microparticles using optical images. *Nature* **436**, 370-372, doi:10.1038/nature03831 (2005).

22 Liu, G. L., Kim, J., Lu, Y. & Lee, L. P. Optofluidic control using photothermal nanoparticles. *Nature Materials* **5**, 27-32, doi:10.1038/nmat1528 (2006).

23 Yang, A. H. J. *et al.* Optical manipulation of nanoparticles and biomolecules in sub-wavelength slot waveguides. *Nature* **457**, 71-75, doi:10.1038/nature07593 (2009).

24 Xu, C., Lei, H., Zhang, Y. & Li, B. Backward transport of nanoparticles in fluidic flow. *Optics Express* **20**, 1930-1938, doi:10.1364/oe.20.001930 (2012).

25 Ross, D., Gaitan, M. & Locascio, L. E. Temperature measurement in microfluidic systems using a temperature-dependent fluorescent dye. *Analytical Chemistry* **73**, 4117-4123, doi:10.1021/ac010370l (2001).

26 Minas, G., Martins, J. S., Ribeiro, J. C., Wolffenbuttel, R. F. & Correia, J. H. Biological microsystem for measuring uric acid in biological fluids. *Sensors and Actuators a-Physical* **110**, 33-38, doi:10.1016/j.sna.2003.10.049 (2004).

27 Lee, J., Paek, J. & Kim, J. A biomimetic mass-flow transducer utilizing all-optofluidic generation of self-digitized, pulse code-modulated optical pulse trains. *Lab on a Chip* **12**, 3766-3773, doi:10.1039/c2lc40468k (2012).

28 Sirbuly, D. J., Tao, A., Law, M., Fan, R. & Yang, P. Multifunctional nanowire evanescent wave optical sensors. *Advanced Materials* **19**, 61-+, doi:10.1002/adma.200601995 (2007).

29 Chang-Yen, D. A. & Gale, B. K. An integrated optical oxygen sensor fabricated using rapid-prototyping techniques. *Lab on a Chip* **3**, 297-301, doi:10.1039/b305358j (2003).

30 Wolfe, D. B. *et al.* Dynamic control of liquid-core/liquid-cladding optical waveguides. *Proceedings of the National Academy of Sciences of the United States of America* **101**, 12434-12438, doi:10.1073/pnas.0404423101 (2004).

31 Tang, S. K. Y., Stan, C. A. & Whitesides, G. M. Dynamically reconfigurable liquid-core liquid-cladding lens in a microfluidic channel. *Lab on a Chip* **8**, 395-401, doi:10.1039/b717037h (2008).

32 Dong, L., Agarwal, A. K., Beebe, D. J. & Jiang, H. Adaptive liquid microlenses activated by stimuli-responsive hydrogels. *Nature* **442**, 551-554, doi:10.1038/nature05024 (2006).

33 Li, Z. Y., Zhang, Z. Y., Emery, T., Scherer, A. & Psaltis, D. Single mode optofluidic distributed feedback dye laser. *Optics Express* **14**, 696-701, doi:10.1364/opex.14.000696 (2006).

34 Suter, J. D., Sun, Y., Howard, D. J., Viator, J. A. & Fan, X. PDMS embedded opto-fluidic microring resonator lasers. *Optics Express* **16**, 10248-10253, doi:10.1364/oe.16.010248 (2008).

35 Gallardo, B. S. *et al.* Electrochemical principles for active control of liquids on submillimeter scales. *Science* **283**, 57-60, doi:10.1126/science.283.5398.57 (1999).

36 Zhou, H. & Yao, S. Electrostatic charging and control of droplets in microfluidic devices. *Lab on a Chip* **13**, 962-969, doi:10.1039/c2lc41060e (2013).

37 Pollack, M. G., Fair, R. B. & Shenderov, A. D. Electrowetting-based actuation of liquid droplets for microfluidic applications. *Applied Physics Letters* **77**, 1725-1726, doi:10.1063/1.1308534 (2000).

38 Galloway, M. *et al.* Contact conductivity detection in poly(methyl methacylate)-based microfluidic devices for analysis of mono- and polyanionic molecules. *Analytical Chemistry* **74**, 2407-2415, doi:10.1021/ac011058e (2002).

39 Martin, R. S., Gawron, A. J., Lunte, S. M. & Henry, C. S. Dual-electrode electrochemical detection for poly(dimethylsiloxane)-fabricated capillary electrophoresis microchips. *Analytical Chemistry* **72**, 3196-3202, doi:10.1021/ac000160t (2000).

40 Martin, R. S. *et al.* Carbon paste-based electrochemical detectors for microchip capillary electrophoresis/electrochemistry. *Analyst* **126**, 277-280, doi:10.1039/b009827m (2001).

41 Wang, J., Polsky, R., Tian, B. M. & Chatrathi, M. P. Voltammetry on microfluidic chip platforms. *Analytical Chemistry* **72**, 5285-5289, doi:10.1021/ac000484h (2000).

42 Tien Anh, N., Yin, T.-I., Reyes, D. & Urban, G. A. Microfluidic Chip with Integrated Electrical Cell-Impedance Sensing for Monitoring Single Cancer Cell Migration in Three-Dimensional Matrixes. *Analytical Chemistry* **85**, 11068-11076, doi:10.1021/ac402761s (2013).

43 Maltezos, G., Nortrup, R., Jeon, S., Zaumseil, J. & Rogers, J. A. Tunable organic transistors that use microfluidic source and drain electrodes. *Applied Physics Letters* **83**, 2067-2069, doi:10.1063/1.1609056 (2003).

44 Fujimoto, T. & Awaga, K. Electric-double-layer field-effect transistors with ionic liquids. *Physical Chemistry Chemical Physics* **15**, 8983-9006, doi:10.1039/c3cp50755f (2013).

45 Osman, R. A., Esa, S. R. & Poopalan, P. DESIGN AND FABRICATION OF MICROFLUIDIC DEVICES: MOSFET & CAPACITOR. *Iemt 2006: 31st International Conference on Electronics Manufacturing and Technology*, 321-327 (2006).

46 Ota, H. *et al.* Highly deformable liquid-state heterojunction sensors. *Nature Communications* **5**, doi:10.1038/ncomms6032 (2014).

47 Cheng, S. & Wu, Z. A Microfluidic, Reversibly Stretchable, Large-Area Wireless Strain Sensor. *Advanced Functional Materials* **21**, 2282-2290, doi:10.1002/adfm.201002508 (2011).

48 Kim, H.-J., Maleki, T., Wei, P. & Ziaie, B. A Biaxial Stretchable Interconnect With Liquid-Alloy-Covered Joints on Elastomeric Substrate. *Journal of Microelectromechanical Systems* **18**, 138-146, doi:10.1109/jmems.2008.2011118 (2009).

49 Sen, P. & Kim, C.-J. Microscale Liquid-Metal Switches-A Review. *Ieee Transactions on Industrial Electronics* **56**, 1314-1330, doi:10.1109/tie.2008.2006954 (2009).

50 Cheng, S., Rydberg, A., Hjort, K. & Wu, Z. Liquid metal stretchable unbalanced loop antenna. *Applied Physics Letters* **94**, doi:10.1063/1.3114381 (2009).

51 Jobs, M., Hjort, K., Rydberg, A. & Wu, Z. A Tunable Spherical Cap Microfluidic Electrically Small Antenna. *Small* **9**, 3230-3234, doi:10.1002/smll.201300070 (2013).

52 Kubo, M. *et al.* Stretchable Microfluidic Radiofrequency Antennas. *Advanced Materials* **22**, 2749-+, doi:10.1002/adma.200904201 (2010).

53 Zheng, Y., Zhang, Q. & Liu, J. Pervasive liquid metal based direct writing electronics with roller-ball pen. *Aip Advances* **3**, doi:10.1063/1.4832220 (2013).

54 Jeong, S. H. *et al.* Liquid alloy printing of microfluidic stretchable electronics. *Lab on a Chip* **12**, 4657-4664, doi:10.1039/c2lc40628d (2012).

55 Ladd, C., So, J.-H., Muth, J. & Dickey, M. D. 3D Printing of Free Standing Liquid Metal Microstructures. *Advanced Materials* **25**, 5081-5085, doi:10.1002/adma.201301400 (2013).

56 Jeong, S. H., Hjort, K. & Wu, Z. Tape Transfer Atomization Patterning of Liquid Alloys for Microfluidic Stretchable Wireless Power Transfer. *Scientific Reports* **5**, doi:10.1038/srep08419 (2015).

57 Carr, J. A. *et al.* A microfluidic platform for high-sensitivity, real-time drug screening on C. elegans and parasitic nematodes. *Lab on a Chip* **11**, 2385-2396, doi:10.1039/c1lc20170k (2011).

58 Chen, B. *et al.* Microfluidic bioassay to characterize parasitic nematode phenotype and anthelmintic resistance. *Parasitology* **138**, 80-88, doi:10.1017/s0031182010001010 (2011).

59 Schurig, D. *et al.* Metamaterial electromagnetic cloak at microwave frequencies. *Science* **314**, 977-980, doi:10.1126/science.1133628 (2006).

60 Zhu, J. *et al.* A holey-structured metamaterial for acoustic deep-subwavelength imaging. *Nature Physics* **7**, 52-55, doi:10.1038/nphys1804 (2011).

CHAPTER 2

AN INTEGRATED FIBER-OPTIC MICROFLUIDIC DEVICE FOR DETECTION OF MUSCULAR FORCE GENERATION OF MICROSCOPIC NEMATODES

A paper published in Lab on a Chip

Peng Liu, Depeng Mao, Richard J. Martin and Liang Dong

2.1 Abstract

This paper reports development of an integrated fiber-optic microfluidic device for measuring muscular force of small nematode worms with high sensitivity, high data reliability, and simple device structure. A moving nematode worm squeezed through multiple detection points (DPs) created between a thinned single mode fiber (SMF) cantilever and a sine-wave channel with open troughs. The SMF cantilever was deflected by the normal force imposed by the worm, reducing optical coupling from the SMF to a receiving multimode fiber (MMF). Thus, multiple force data could be obtained for the worm–SMF contacts to verify with each other, improving data reliability. A noise equivalent displacement of the SMF cantilever was 0.28 μm and a noise equivalent force of the device was 143 nN. We demonstrated the workability of the device to detect muscular normal forces of the parasitic nematodes Oesophagotomum dentatum L3 larvae on the SMF cantilever. Also, we used this technique to measure force responses of levamisole-sensitive (SENS) and resistant (LERV) O. dentatum isolates in response to different doses of the anthelmintic drug, levamisole. The results showed that both of the isolates generated a larger muscular normal force when exposed to a higher concentration of levamisole. We also noticed muscular force phenotype differences between the SENS and LERV worms: the SENS muscles were more sensitive to

levamisole than the LERV muscles. The ability to quantify the muscular forces of small nematode worms will provide a new approach for screening mutants at single animal resolution. Also, the ability to resolve small differences in muscular forces in different environmental conditions will facilitate phenotyping different isolates of nematodes. Thus, the present technology can potentially benefit and advance the current whole animal assays.

2.2 Introduction

Movement of multicellular organisms, such as the nematode *Caenorhabditis elegans,* exhibits a sinusoidal pattern induced by alternating dorsal and ventral muscle contraction when swimming/crawling across surfaces.[1,2] The waves of the muscle contraction produce local bending in the cuticle and generate lateral thrust or planar force.[3] Researchers have showed that the nematodes maintain their motion generation mechanism by producing lateral thrust in either natural or artificially structured surrounding environments.[4] There has been considerable attention devoted to organismal biomechanics of important nematode species.[5–9] Investigation of correlations between genes, neurons, sensory organs, muscular arms, and motion patterns of these nematodes is critical to understand: a) the coupling between signals in the neuromuscular system, b) the muscle dynamics, and c) the emergent mechanical behaviour of the whole animal.[10,11] Applications of organismal biomechanics include ameliorating human health problems (*e.g.*, prosthesis design and movement restoration),[12] and developing new therapy for neuromuscular diseases caused by mechanosensory degradation and defects.[13] Also, through genetic modification, mutants of *C. elegans* can be created, which affect the forces of motion and thus the phenotypic locomotive behavior of mutants.[14,15] Thus, screening these mutants at the single animal resolution needs a miniature force sensor suitable for detecting the muscular force of these mutants. Furthermore, as we

will see later, it is possible to screen drug resistance of parasitic nematodes by directly examining muscular forces of parasitic nematode species under different chemical or drug environmental conditions. This is because drug resistance of parasitic nematodes may be associated with changes in signalling-muscle-contraction pathways.[16,17]

Many tools have been developed to analyze cellular and molecular mechanics in the past two decades,[18] including optical tweezers,[19–21] atomic force microscopy,[22–24] magnetic twisting cytometry,[25,26] micropipette aspiration,[27,28] and micro-electro-mechanical systems (MEMS) sensors and actuators.[29,30] These tools have yielded important insights into fundamental biology research.[31,32] However, they are not suitable for use in the study of multicellular organismal biomechanics of small nematode worms. The advent of MEMS, microfluidics, and automated imaging techniques have led to a new class of miniature devices and systems to study neurophysiology and behaviour of nematode species via flexible manipulation, imaging and screening of the nematodes.[33–46] However, due to a lack of new muscular force sensing tools, the study of the multicellular organismal mechanics currently lags behind that of the cellular and molecular mechanics. Pruitt and co-workers pioneered the use of a piezoresistive cantilever-based indentation system for studying the mechanical properties of *C. elegans*.[3] This system offered advantages such as a wide range of force and displacements matched to different biological materials, and an ability to target a desired dynamic range and a high force resolution of 12 nN; but it was unable to detect the dynamic force of a worm in motion. To detect the dynamic force of moving nematodes, the researchers reported another remarkable nematode force measurement microsystem using an integrated strain gauge force sensor, with a force resolution of the device was 260 nN.[47] The device was constructed from multiple layers of SU-8 and metal on quartz substrates, capable

of measuring tactile sensitivity and interaction forces exerted during locomotion, but the device structure was relatively complicated. Subsequently, Ghanbari and co-workers developed a simple microfluidic device for measuring force generated by moving nematodes in real-time.[4,48] The device used an array of vertical polymeric pillars fabricated in a channel. The force applied by a moving nematode to each pillar was detected via a vision-based approach. This vision-based force sensing system was capable of performing robust force measurements with a 330 nN resolution.[4] This technique, however, required a high-resolution microscope with an automated stage, a video camera, and a special algorithm to track worm movement and resolve mechanical deflections of the pillars induced by the nematode-pillar contacts. Also, the deflections of the short pillars were limited by a relatively low manufacturable aspect ratio of the pillars, causing low sensitivity of the device.

2.3 Methods and Experimental Section

2.3.1 Device principle and design

Fig. 2.1 presents our fiber-optic microfluidic device for detecting muscular forces of small nematode worms. A worm enters a sine-wave channel at a worm inlet without applying any attractants. To minimize body contact between the worm and the sidewalls of the channel, the amplitude and wavelength of the sine-wave channel are designed to be similar to those of the worms under test. Also, the channel is wide enough to neglect constraints from the sidewalls on the worm's natural movement. The lower part of this sine-wave channel is open, where a silica SMF cantilever is suspended horizontally adjacent to the channel. The SMF cantilever is anchored at one end and free to bend at the other end, accepting an input light at the fixed end (from an external light source). A receiving MMF (unmoveable) is embedded in the channel and aligned with the SMF along central optical axis. As the worm contacts the SMF cantilever and squeezes through the troughs of the sine-wave channel, the

SMF cantilever is forced to deflect horizontally away from the channel by the normal force, F_n, of the worm (see inset in Fig. 2.1). This reduces light coupling from the SMF to the MMF and thus the transmitted optical power received by an external photodetector (connecting to the MMF). By this means, F_n of the worm exerted on the SMF cantilever was detected. The horizontal placement of the SMF has the advantage of a high aspect ratio of the SMF, and leads to a more sensitive detection of the responses of the SMF to F_n. As the worm swims through the whole sine-wave channel, the multiple worm-SFM contacts at the different detection points (DPs) generates multiple force data that can be cross-checked and/or averaged, thus improving the reliability of the force data.

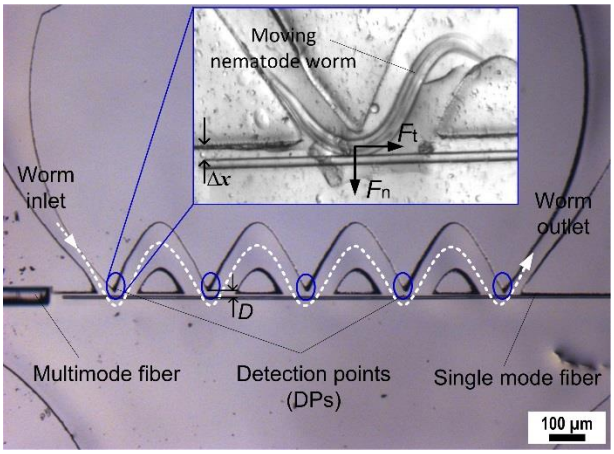

Fig. 2.1 Optical image of a fabricated fiber-optic microfluidic device for detecting force of a small nematode worm. The white dashed line represents a wave form of a sine-wave channel. The blue circles highlight multiple detection points (DPs) along a thinned single mode fiber (SMF) cantilever. Inset shows a worm (SENS *O. dentatum* larvae) pushing the cantilever away from the original while squeezing through one of five DPs formed between the SMF cantilever and the lowest edge of the channel's upper sidewall. Δx is deflection at the free end of the SMF cantilever. F_n and F_t represent the normal force and tangential force, respectively, of a worm applied to the SMF cantilever.

To obtain high mechanical sensitivity while allowing for good light propagation, the SMF cantilever was thinned down to the optical mode field diameter, d_f, of the fiber. The SMF (here, SMF-28, Corning) was etched to 10 µm in diameter to match the d_f (9.2 µm) at a

light wavelength of 1310 nm and the d_f (10.4 μm) at 1550 nm of the original fiber. The diameter of the MMF was 65 μm. The sine-wave channel was designed to have an amplitude of 160 μm and a wavelength of 450 μm to match the traveling wave patterns of the SENS and LERV larvae used in this work. The gap between the SMF and the lowest edge of the channel's upper sidewall, *D*, was 20 μm (see the denotation of *D* in Fig. 2.1; the influence of *D* on worm force generation will be discussed later). The fiber-to-fiber end distance was 50 μm. To ensure that the SMF cantilever deflection occurs only in planar direction, the central optical axis of the SMF was set to be 12.5 μm, or half the diameter (~25 μm) of the SENS and LERV worms used, above the bottom surface of the channel. The SMF cantilever was 2 mm long spanning over the 5 DPs. As we will see later, the length of the cantilever is limited by its elastic downward deflection in the vertical direction.

To simulate the deflection responses of the SMF cantilever to F_n applied at different DPs of the cantilever, finite-element analysis (FEA) was performed using the ANSYS software package.[49] As shown in Fig. 2.2a, the deflection at the free end of the cantilever Δx was proportional to magnitude of F_n, following a linear spring force-deflection model given by $F_n = k\Delta x$, where k is the stiffness of the cantilever.[50] As seen later (Figs. 2.6d and 2.7e), the SENS *O. dentatum* generates the same F_n while deflecting the SMF cantilever at different DPs. We therefore applied F_n = 9.16 μN at the five DPs in this simulation (Fig. 2.2b). As expected, a larger Δx was obtained as F_n was applied closer to the free end of the cantilever. Specifically, the simulated Δx was 18.6, 12.6, 6.28, 2.07, and 0.074 μm at the five DPs from left to right along the cantilever (Fig. 2.2b).

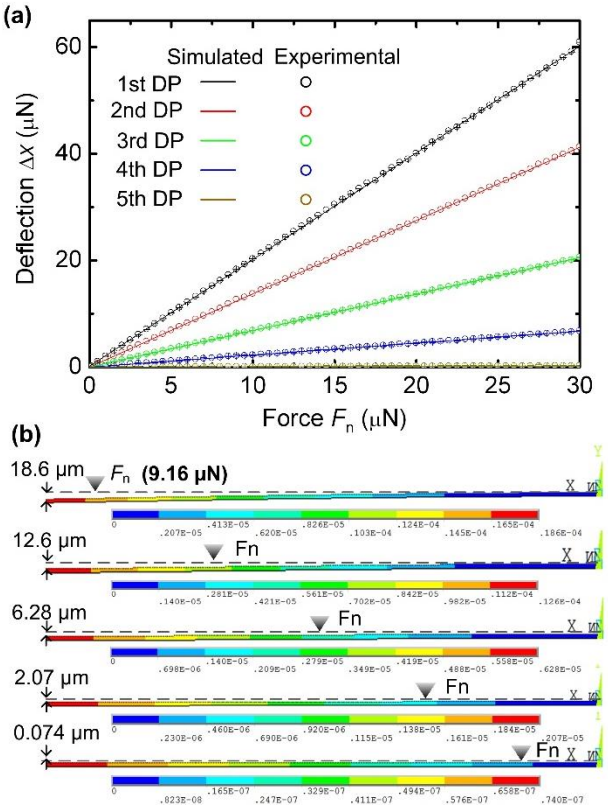

Fig. 2.2 (a) Finite element analysis (FEA) simulated and nanoindentation determined deflection, Δx, at the end of a SMF silica cantilever, as a function of normal force applied at five DPs along the SMF cantilever. The SMF cantilever used in the FEA simulation was 10 μm diameter and 2 mm long. The SMF cantilever used in the nanoindentation experiment was 10.07 ± 0.11 μm in diameter and 2 mm in length. (b) Deflection profile of the SMF cantilever under a given normal force of 9.16 μN applied at five DPs.

To confirm the accuracy of the model used in the F_n–Δx simulation, we used a nanoindenter (NANO Indenter XP, MTS Systems) to measure the deflections of the fabricated SMF cantilevers (see the fabrication processes in Fig. 2.5) under various applied forces (Fig. 2.2a). The SMF cantilevers under test were 10.07 ± 0.11 μm in diameter and 2 mm in length. The force and displacement resolution of the nanoindenter was 50 nN and 0.01 nm, respectively. The controlled forces F_n were applied to each DP (normal to the SMF cantilever). Each measurement was the mean ± standard deviation obtained from 9 data points. As shown in Fig. 2.2a, the measured displacement at the free end of the cantilever Δx had a good agreement with the simulated result, demonstrating the accuracy of the model

used in the FEA simulation. Specifically, when F_n = 9.16 μN, the displacement at the free end of the cantilever Δx was found to be 18.66 ± 0.21, 12.54 ± 0.25, 6.31 ± 0.14, 2.07 ± 0.24, and 0.074 ± 0.14 μm at the five DPs from left to right along the cantilever. Correspondingly, the average changing rate of Δx with respect to F_n was calculated to be 0.50 ± 0.009, 0.75 ± 0.011, 1.48 ± 0.015, 4.49 ± 0.026, and 124.7 ± 0.914 μm/μN at the five DPs from left to right along the SMF cantilever.

When the SMF cantilever and the fixed MMF were well aligned along their optical axis, the fiber-to-fiber end coupling efficiency reaches a maximum. However, the bending effect of the SMF caused a decrease in the coupling efficiency. Thus, to compute the optical power, P, detected at the output of the MMF as a function of Δx, we employed the three-dimensional finite-difference time-domain (FDTD) method based on the MEEP software package.[51] This method allowed us to include the dielectric (or refractive index) properties of all device components (the SMF cantilever, the MMF, and the surrounding environment) into the model. Thus, the simulation inherently took into account the effect of the light refraction at the fiber side–water and fiber end–water interfaces on the final optical readings. The computing region is shown in Fig. 2.3a. A 10 μm thick perfectly matched layer (PML) was applied at the boundaries of the entire computing region. A transverse electric (TE)-polarized line source was placed at the input of the SMF cantilever. Fig. 3b shows the optical field distributions of the device at different bending conditions. The simulation result includes two factors for determining the level of reduction in the output optical power, including the axial misalignment between the two fibers, and distortion of the SMF's fundamental mode field (due to small-angle bending). By combining the results shown in Figs. 2a and 3c, we

obtained the relationship between the normalized P and applied F_n (Fig. 2.3d). The result shows that P decreases with increasing F_n applied at each DP.

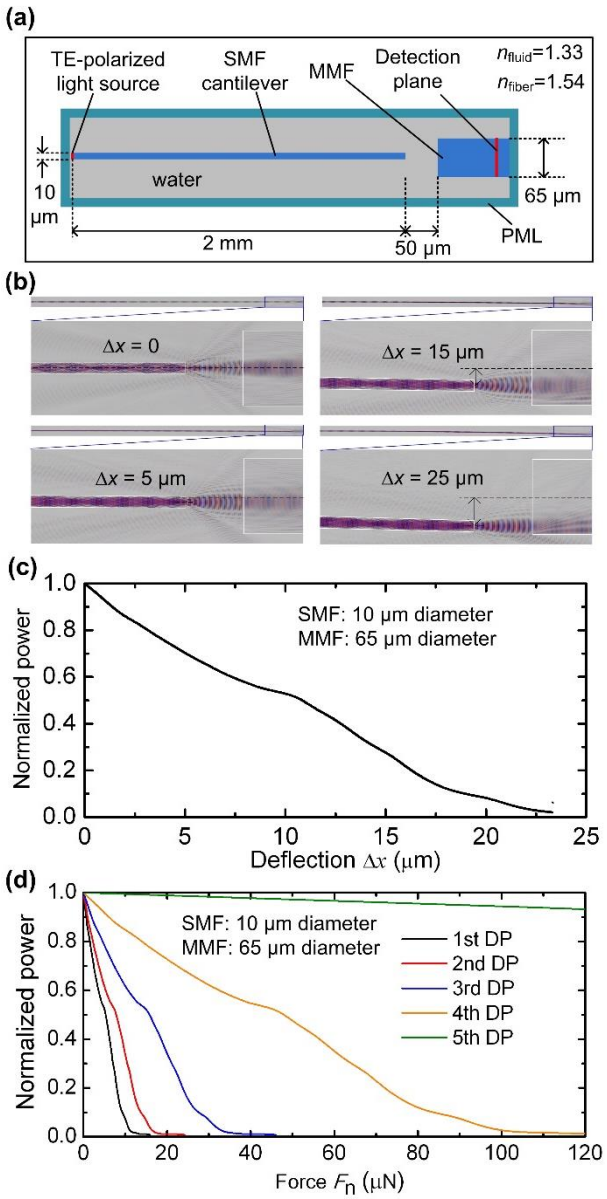

Fig. 2.3 (a) Top-view schematic of the computing region used in the 3D finite-difference time-domain (FDTD) simulation. (b) Optical field distributions in the optical coupling region between the SMF cantilever and MMF under different bending conditions: Δx = 0, 5, 15, and 25 μm. The fields were extracted in the horizontal plane at the optical axis of the two fibers. (c) FDTD simulation result of normalized optical power detected at the output of the receiving MMF, as a function of deflection Δx at the end of the SMF cantilever. (d) Simulation result of normalized optical power as a function of F_n applied to the SMF cantilever at different DPs.

It is desirable to employ longer SMF cantilevers to achieve higher mechanical sensitivity to an applied F_n, but practically, to prevent the worm under test from crossing over the SMF cantilever to the other side of the sine-wave channel, the SMF cantilever needed to be suspended horizontally in the channel. Thus, the length of the cantilever was actually limited by natural elastic deflection of the cantilever in the vertical direction. Our ANSYS simulation result indicates that the 2 mm long SMF cantilever (used in the previous figures) dropped about $\Delta z = 0.75$ μm at the free end of the cantilever from the horizontal direction. With this design, 10.66 % of 244 worms were observed to cross over the cantilevers at the 1st DP (see the Handling of Nematodes section). As mentioned in the Introduction section, nematodes generally maintain their motion generation mechanism by producing lateral thrust, We thus believe that there was little vertical force exerted to the 2 mm long SMF cantilever when the central optical axis of the cantilever was designed to be at half the worm diameter above the substrate. Fig. 2.4 shows a failure of the force test with a 4 mm long SMF cantilever having a relatively large drop of $\Delta z = 2.1$ μm at its free end. Since the head part of the worm was a little sharp relative to other parts and could move in more complex ways, the worm had a relatively high chance to first move its head on the upper part of the cantilever, and then, cross over the cantilever from the top of the cantilever via the lateral motion. According to our observation on 55 worms, ~52.7 % of the worms crossed over the 4 mm long SMF cantilever. Thus, the length of the SMF cantilever was chosen to be 2 mm for the present device.

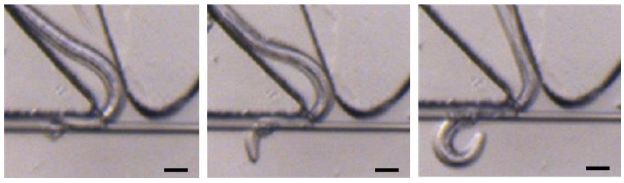

Fig. 2.4 Optical images for a SENS *O. dentatum* larvae crossing over the 4 mm long SMF cantilever from the top of the cantilever at the 1st DP of the device. Scale bars represent 20 µm.

2.3.2 Device fabrication

Figs. 2.5a-f shows the fabrication processes for the proposed device. First, poly(dimethylsiloxane) (PDMS) microstructures (e.g., the sine-wave channel, and the alignment structures for the fibers) are replica molded using conventional soft lithography techniques (Fig. 2.5a).[52] The silica SMF (SMF-28, Corning) and the MMF (62.5/125-CPC6, Corning) are immersed in 49 wt.% hydrofluoric (HF) acid solution at room temperature for 120 and 60 mins, respectively. This allowed us to pre-thin the SMF from 125 µm down to 25 µm, and the MMF from 125 µm to 65 µm. Then, the two fibers were inserted and positioned in the alignment structures, with the help of a micropositioner (Fig. 2.5b). To form a 10 µm-diameter SMF cantilever, we protected the MMF from being etched by a buffered HF (BHF, 10 vol./vol. %) solution. Thus, the channel was filled up with a precursor solution consisting of isobornyl acrylate (IBA), tetraethylene glycol dimethacrylate, and 2,2-dimethoxy-2-phenylacetophenone with a weight ratio of 32 : 1.7 : 1.0 (Fig. 2.5c).[53] The precursor solution was then selectively polymerized under ultraviolet light (10 mW/cm^2, 24.8 s) with a photomask. This allowed for formation of HF resistant poly-IBA structures around the MMF and fixing one end of the SMF (Fig. 2.5d). Next, the flexible part of the SMF was etched down to 10 µm diameter in the BHF solution for 75 mins (Fig. 2.5e). Note that the removal of the fiber cladding did not interfere with light guidance through the silica core, since the original refractive index cladding (n = 1.463) was replaced by water (n = 1.333).[54] Lastly, the

PDMS structure was bonded to a glass slide by oxygen plasma treatment (Fig. 2.5f). Thus, the fiber-optic microfluidic device was formed.

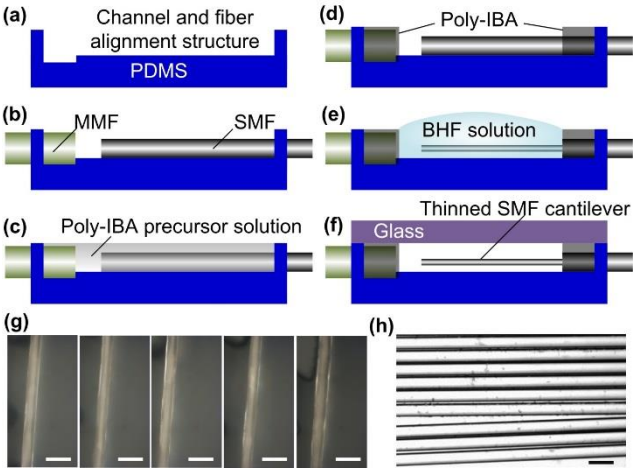

Fig. 2.5 (a-f) Fabrication processes for the device. (g) Optical images showing the SMF cantilever at five different locations. (f) Optical image showing nine SMFs fabricated in different runs using the same chemical wet etching method. Scale bars in (g) and (h) represent 20 μm.

It should be pointed out that the final diameter and uniformity of the SMF cantilever would significantly influence the mechanical properties and thus the actual readings of the muscular forces. The use of the low average etching rate of 0.2 μm / min during thinning the SMF from 25 to 10 μm ensured a relatively high uniformity in the final diameter of the SMF cantilever. As shown in Figs. 2.5h and 2.5g, the final diameter of the fabricated SMF cantilever was 10.03 ± 0.12 μm (mean ± standard deviation, obtained by averaging the measurement results over nine SMF cantilevers with each cantilever providing 5 data points). Note that these SMF cantilevers were fabricated in different runs by using the same chemical wet etching method, demonstrating the reproducibility of forming the desired thin SMF cantilever (the most important component of the device).

2.3.3 Optical measurement setup

In our optical measurement setup, a fiber pigtailed laser diode of 1310 nm nominal wavelength (LPS-1310, Thorlabs) was used as an external light source and coupled into the SMF cantilever. Real-time output signals from the MMF were detected by an optical power meter (1918-R, Newport) with built-in data acquisition software.

2.3.4 Velocity measurement

While the present force sensing scheme did not require using a microscope or a camera, we used a stereo microscope (MZ205, Leica) and a video camera (QICamera) to show the worm-SMF cantilever interactions and measure the average moving velocity of worms exposed to anthelmintic levamisole with different concentrations (Fig. 2.8). The worm average velocity was defined as the continuous forward linear distance travelled by a worm's head with respect to time. The stereo microscope-camera system captured a series of digital images (1392 × 1040 pixels) at a specified time interval of 100 ms. The images were sequenced and compressed into the Audio Video Interleave (.avi) video format. The .avi video was post-processed by a worm tracking program that was able to extract track signatures and locomotion (e.g., number and duration of stops, and cut-off region) of individual and/or worms.[45] Briefly, the program analyzed a large number of images to recognize a moving object (here worm) and then, extract motility parameters such as amplitude, wavelength, body postures, and path traversed by the worm.

2.3.5 Parasitic nematode *O. dentatum*

Many nematodes are ubiquitous soil-dwelling organisms and are crucial for maintaining soil nutrients and overall symbiotic relationships between plants and other organisms.[55] However, many of the more than 10,000 known nematode species are parasitic, infecting plants (e.g. corn, soybean, wheat, and other food grains), animals (e.g. pigs, sheep,

goats, and cows) and humans.[56] The parasitic nematode used in this research, *O. dentatum*, is a hog parasite that causes nodule growths in the pig's gut wall. These nodules repress growth and thereby reduce available pork yield. It is similar to the *Oesophagostomum* species parasites of humans.

Parasitic nematode larvae SENS (levamisole-sensitive) and LEVR (levamisole-resistant) *O. dentatum* were originally supplied by the Royal Veterinary and Agricultural School, Frederiksberg, Copenhagen and then reproduced at 6 – 9 month intervals by passage in pigs at the Iowa State University, Ames, Iowa. The L3 larvae isolates were maintained between passages in tap water refrigerated at 11 °C (changed every 2 – 4 months). They were about 6 months old and 400 – 500 µm long and about 25 µm diameter when used for our experiments.

2.3.6 Handling of nematodes

A conventional pipette was used to transfer *O. dentatum* worms to the sine-wave channel at the worm inlet of the device. No attractant was used to drive worms inside the channel. With the gap D between the SMF and the lowest edge of the channel's upper sidewall of 20 µm, 183 (75 %) out of 244 worms moved through all five DPs, 26 (10.66 %) crossed over the cantilever at the first DP, and 35 (14.34 %) were stuck at the first DP that could be sucked out by a pipette through the inlet of the device.

2.4 Results and Discussion

Fig. 2.6a shows time-lapse images for a SENS worm interacting with the SMF cantilever at different DPs of the device. Each measurement presented here was the mean ± standard deviation obtained from 22 observations. As the worm squeezed through the 1st, the 2nd, the 3rd and the 4th DP from left to right (Fig. 2.6a), the maximum deflection at the free end of the SMF cantilever was Δx = 19.3 ± 0.92, 11.6 ± 0.83, 6.9 ± 0.85, and 2.5 ± 0.81 µm

(Fig. 2.6b), respectively. The decreasing tendency of Δx was observed in the microscope and shows good agreement with the simulation result with F_n = 9.16 μN (Fig. 2.2b). Fig. 2.6c displays a typical time-varying optical power signal measured at the output of the MMF as the worm travelled through the whole channel. Interestingly, the optical power decreased respectively by 90.4 ± 3.92, 65.2 ± 4.22, 41.2 ± 3.88, and 20.2 ± 4.18 %. This resulted from decreasing the deflection of the cantilever as the worm-SFM contact occurred closer to the fixed end of the cantilever. By extrapolating from the F_n–P curve shown in Fig. 2.3d, the magnitude of F_n imposed by the worm onto the cantilever at the four DPs (from left to right) was found to be 9.02 ± 0.23, 8.87 ± 0.28, 9.23 ± 0.33, and 9.13 ± 0.36 μN, respectively (Fig. 2.6d). The force measurement result revealed that the worm generated almost an equal amount of F_n = 9.16 ± 0.32 μN, during squeezing through the multiple DPs (Fig. 2.6d). Therefore, the closer the DP was to the fixed end of the cantilever, the less the cantilever deflection was, as shown in Fig. 2.6b. The small standard deviation of F_n might be attributed to individual differences between the worms and/or slight geometric difference between the multiple DPs. We point out that the reduction of optical power due to the worm-SFM contact at the 5th DP was not large enough to be read by the photodetector, which will be discussed later. Nevertheless, by integrating multiple structurally similar DPs to the sine-wave channel along the SMF cantilever, the device provided multiple force data allowing additional validation.

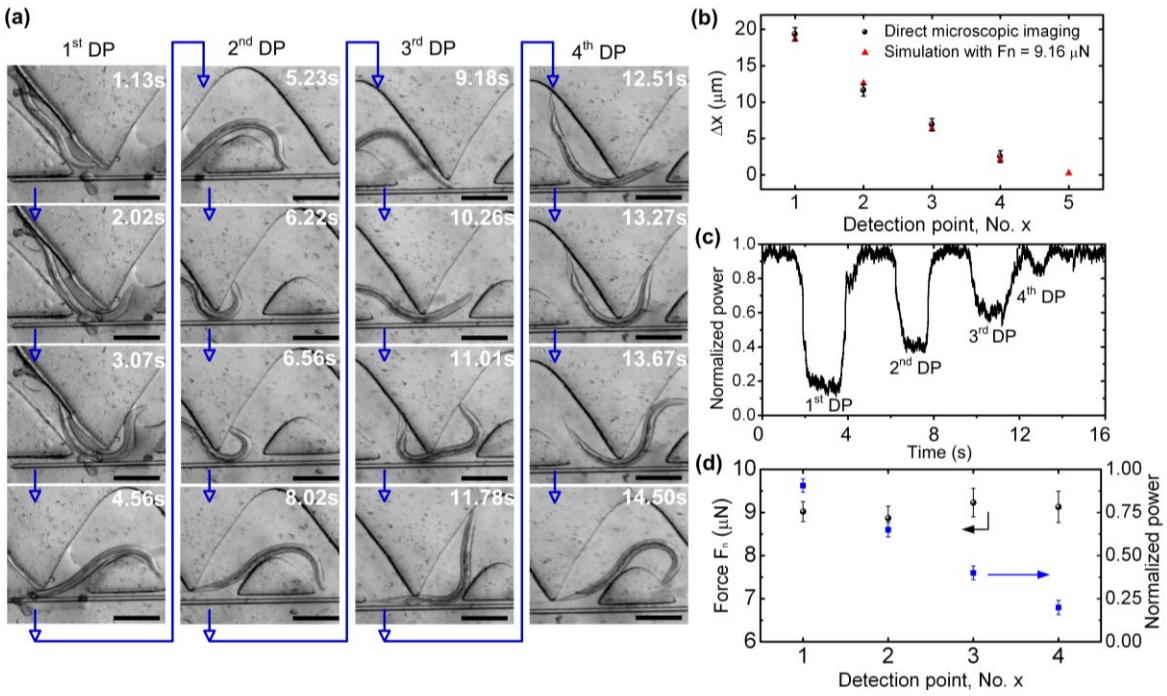

Fig. 2.6 (a) Time-lapse images for a SENS *O. dentatum* worm pushing the SMF cantilever away from the sine-wave channel at different four DPs from left to right shown in Fig. 2.1. Blue arrows indicate the time-varying sequence of images. Scale bars represent 100 μm. (b) Displacement Δx at the end tip of the SMF cantilever at different DPs. At the 5th DP, only simulation data is shown due to insufficient deflection of the SMF cantilever. Experimental data were obtained via direct microscopic imaging. Calculated data were obtained using ANSYS software. F_n = 9.16 μN was used in the simulation. (c) Normalized optical power measured at the output of the receiving MMF as a function of time. (d) Experimental normal force (left axis) measured when the worm-SMF interactions occurred at the first four DPs. No readable signal was found at the 5th detection point.

To examine the influence of the gap *D* between the SMF and the lowest edge of the channel's upper sidewall on force generation of the worms, we varied *D* from 5 to 50 μm with steps of 5 μm. The SENS worms were taken from the same batch as those used above, having the body diameter *d-worm* = ~25 μm. When *D* = 5 and 10 μm, the worms could hardly squeeze through the 1st DP, while instead they touched the cantilever and then oscillated locally. Thus, with this design, the device was not able to detect force of the worms. As the gap increased becoming comparable to or slightly less than the diameter of the

worm, about 75 % of the worms were able to get into the gap and push the cantilever away to pass through the sine-wave channel. Figs. 2.7a-c show the optical power signals detected at the output of the MMF for the worms with *d-worm* = ~25 µm when *D* = 15, 20, and 25 µm, respectively. As *D* increased, F_n of the worms increased (Fig. 2.7e). Each data point in Fig. 2.7e was obtained from measurement of 9 worms. An intuitive explanation is that the worms needed to generate a larger squeezing force to go through a narrower space. When *D* increased further to be greater than 30 µm, the worms were observed to have relatively random and insufficient contacts with the SFM cantilever, resulting in random optical power signals at the output of the MMF. In addition, we examined the influence of the body diameter of nematodes *d-worm* on their muscular force generation when the gap *D* was fixed. Fig. 2.7d shows the detected optical power signal as a large SENS (*d-worm* = ~30 µm) went through the DPs with *D* = 25 µm. Compared to the small worms (*d-worm* = ~25 µm) with F_n = ~5.58 µN, the large worms (*d-worm* = ~30 µm; 9 worms tested) generated a larger F_n = ~8.62 µN, which was 54.5 % more than the small ones (Fig. 2.7e), to pass through the same DPs.

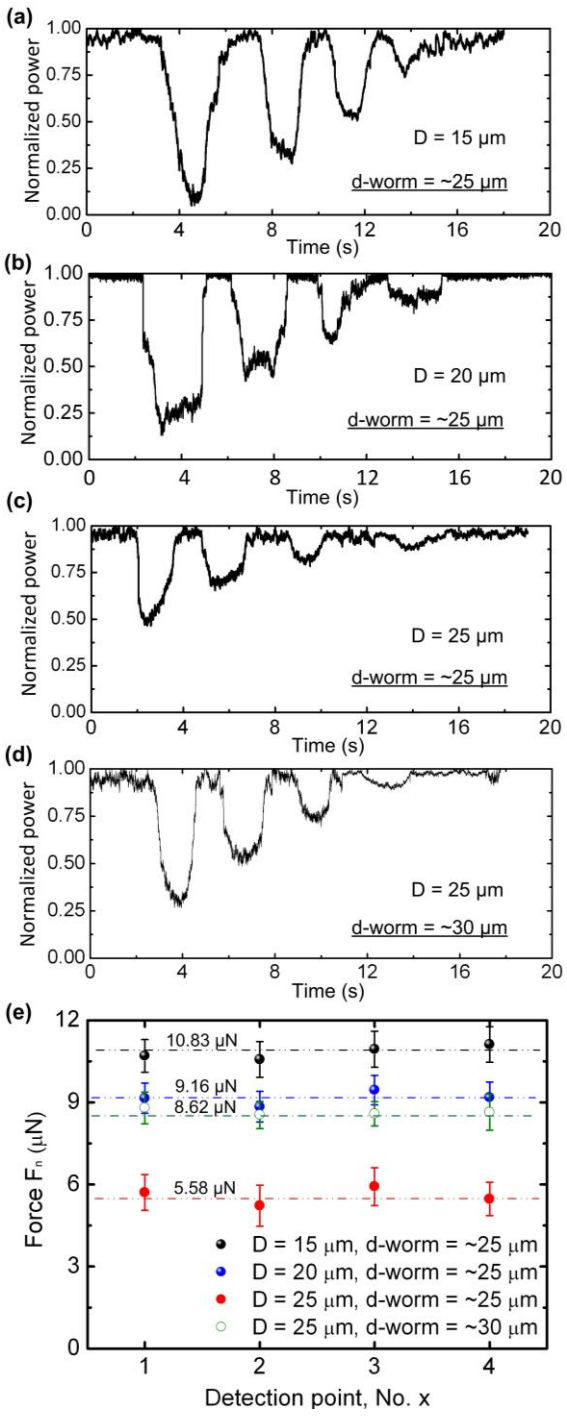

Fig. 2.7(a-c) Normalized optical power measured at the output of the MMF as function of time when the initial gap distance between the SMF cantilever and the lowest edge of the channel's upper sidewall *D* = 15 μm (a), 20 μm (b), and 25 μm (c) with the worm (SENS) diameter *d-worm* = ~25 μm, and *D* = 25 μm with *d-worm* = ~30 μm (d). (e) Normal force of the worms measured at the first four DPs with respect to *D* and *d-worm*.

According to the time-varying optical power measurement results shown in Figs. 2.6c and 2.7a-d, the mean background noise power level of the detection system, P_{ns}, was approximately 2.5 % of the maximum output optical power, P_{max}. Thus, by looking at Figs. 2.3c and 2.3d, a noise equivalent displacement (NED) of the cantilever and a noise equivalent force (NEF, at the 1st DP) of the device was found at 0.28 μm and 143 nN, respectively. When the worm-body contact occurred at the last or the 5th DP, the predicted deflection of the cantilever was only Δx = 0.074 μm (Fig. 2.2b). No obvious optical signal reduction or force data were thus detected at this DP.

As shown in Fig. 2.3d, the magnitude of the output optical signal was almost saturated at a low level when the SMF deflection goes beyond 23 μm from the central optical axis of the SMF. Thus, we defined the upper boundary of detection range of the device at each DP to be the force at which the saturation starts. It is also noteworthy that the upper limit of the detection range varied with numerical aperture of the MMF, and with the end-to-end distance between the SMF and MMF. Here we define the lower boundary of detection range to be two times the value of NEF at each DP. Table 1 summarizes the NEP and detection range of the device.

Table 1. Summary of the noise equivalent force and detection range of the device at each DP

Detection point	*Noise equivalent force (μN)*	*Detection range (μN)*
1st	0.143	0.28−12.48
2nd	0.21	0.42−16.65
3rd	0.42	0.84−34.02
4th	1.29	2.58−103.17
5th	36.02	72.04−3094.60

Many anthelmintic drugs act on the neuromuscular system of nematodes, causing neuromuscular contraction.[16] Drug resistance of parasitic nematodes may be related to effects on the signalling-muscle-contraction pathways by these drugs.[16] We conducted an initial pilot

experiment to explore the possibility of adapting the present force measurement technique to examine muscular force dose responses of the SENS and LEVR *O. dentatum* larvae to the anthelmintic levamisole. The levamisole solutions with different concentrations were prepared by dissolving levamisole stock solution with appropriate amounts of M9 buffer solution. The recipe for the M9 buffer (3 g KH_2PO_4, 6 g Na_2HPO_4, 5 g NaCl, 1 mL 1 M $MgSO_4$, and H_2O to 1 L) was a standard recipe. The devices used here had the same D = 20 μm as those used in the previous experiments. Each data point in Fig. 2.8 was obtained from measurement of 11 worms.

Fig. 2.8a shows that as the levamisole dose increased from 1 to 20 μM, F_n of the SENS isolate increased from 9.16 to 15.25 μN. The result is logical as the levamisole depolarized muscle and increased muscle contraction and thus the muscular force of the whole worm. No force data were obtained at 25 μM and higher concentrations because the SENS isolate became paralyzed at those high doses. On the other hand, for the LEVR isolate, there was only a slight increase in F_n as the levamisole concentration increased from 1 to 20 μ M. At the higher concentration of 25 μM, an obvious increase of F_n occurred to the LERV isolate. Also, the result in Fig. 2.8a indicates that in the presence of the same dose of levamisole below 20 μM, the drug effect on the SENS muscles in the normal direction (with respect to the movement) was greater than that on the LEVR muscles. Thus, we have observed the distinct phenotype differences in the muscular force of the SENS and LEVR isolates when exposed to levamisole. The result was consistent with the larval migration studies where SENS was inhibited more than LEVR by levamisole.[16] To relate the muscular force phenotype to the locomotive behavior of the worms, we tested the moving velocity of the SENS and LERV isolates on a 1 inch diameter Petri dish. The result in Fig. 2.8b shows

that although the average velocity of both of the isolates decreased with increasing levamisole concentration, the LERV was less sensitive to levamisole than the SENS in terms of the moving velocity. The cause of the velocity reduction may be associated with the increasing muscular force in the direction normal to the worm's translational movement and thus the resultant spastic paralysis. Thus, the device allowed for clear separation of the muscular force phenotype differences between nematode isolates. The drug response test conducted here not only verified the workability of the present technique further, but also demonstrated the useful capability to bridge the observations on the motility and the muscular force generation of individual worms when exposed to different drug environments.

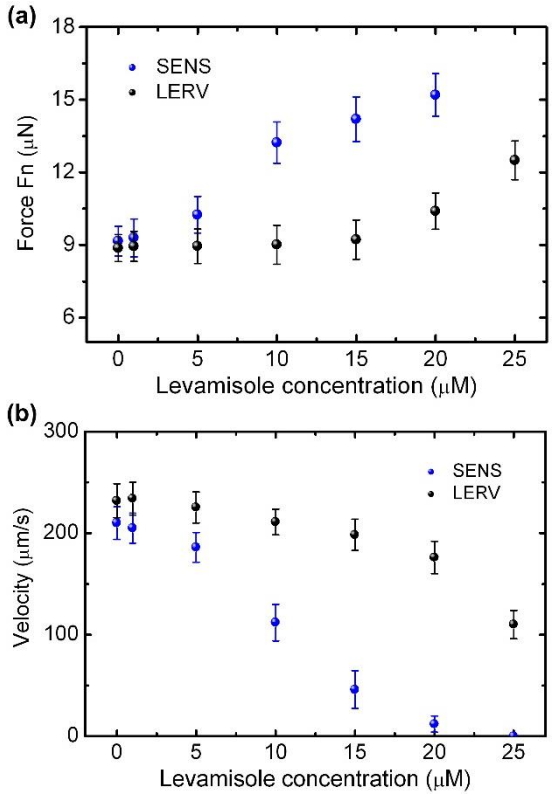

Fig. 2.8 Normal force (a) and moving velocity (b) of the SENS and LERV isolates as a function of levamisole concentration. The moving velocity is tested on plate

2.5 Conclusions

To summarize, we have developed an integrated fiber-optic microfluidic device capable of measuring the muscular force of nematode worms normal to the translational movement direction. Multiple identical DPs were formed along a thinned SMF cantilever horizontally placed adjacent to a sine-wave channel with multiple open troughs. Physical contacts between a moving worm and the SMF cantilever at the DPs bent the SMF cantilever, reducing light coupling from the SMF to the receiving MMF. Thus, the SMF cantilever transduced the normal force of the worm into optical transmission signals. We have demonstrated the workability of the device to detect normal forces exerted by the *O. dentatum* L3 larvae onto the SMF cantilever. It was important that the space dimension between the SMF cantilever and the sine-wave was comparable to or slightly less than the diameter of the worm. We have shown that the worm imposes an equal amount of normal force on the SMF cantilever at different DPs. The NEP of the device was 143 nN at the 1st DP. We have measured the force responses of the SENS and LERV *O. dentatum* larvae to different doses of the anthelmintic levamisole. The result showed that the both of the isolates generate larger muscular (normal) force when exposed to a higher concentration of levamisole, and the SENS muscles were more sensitive to levamisole than the LEVR muscles. We have noticed muscular force differences between the two isolates in the degree of their drug resistance.

The ability of the present device to measure muscular force of multicellular nematodes can benefit and advance the current whole animal assays. For example, conventional nematode motility assays (e.g., larval migration assay[57]) for detection of drug resistance uses a mesh system, where the worms resistant to a certain anthelmintic can move

through the mesh, whereas the sensitive worms are restricted. The output information obtained is thus only a percentage of worms that are inhibited by the applied drug. Recent microfluidic approaches, along with imaging systems and automated algorithm, have made it possible to provide important phenotypic parameters of nematodes such as average velocity and oscillation frequency.[58,59] However, these methods are limited by a lack of more direct measures of drug resistance. Since drug resistance of parasitic nematodes may be associated with the many different changes in signalling-muscle-contraction pathways, our technology will have the potential to provide a more direct measure of the effectiveness of drugs, by qualifying the muscular force of parasitic nematode species. Furthermore, this technology can provide a new insight into developing better quantitative models for revealing phenotypic differences in nematodes under various drug concentrations, as well as screening mutants at the single animal resolution.

2.6 Acknowledgements

This work is supported by the NSF under award no. ECCS-1102354, the McGee-Wagner Research Fund, the NIH grant: R56 AI047194–11 National Institute of Allergy and Infectious Diseases, and the China Scholarship Council. The content is solely the responsibility of the authors and does not necessarily represent the official views of the National Institute of Allergy and Infectious Diseases. The authors thank all members in the Laboratory for NEMS and Lab-Chips for helpful discussion.

2.7 References

1 E. Niebur and P. Erdos, *Biophys. J.*, 1991, **60**,1132–1164.

2 J. E. Harris and H. D. Crofton, *J. Exp. Biol.*, 1957, **34**,116–130.

3 S. Park, M. B. Goodman and B. L. Pruitt, *Proc. Natl. Acad. Sci. U. S. A.*, 2007, **104**, 17376–17381.

4 A. Ghanbari, V. Nock, R. Blaikie, X. Q. Chen, W.H. Wang, *The 6th Annual IEEE International Conference on Automation Science and Engineering*, 21–24 Aug. 2010, Toronto, Ontario, Canada, 198–203.

5 L. A. Herndon, P. J. Schmeissner, J. M. Dudaronek, P. A. Brown, K. M. Listner, Y. Sakano, M. C. Paupard, D. H. Hall and M. Driscoll, *Nature*, 2002, **419**, 808–814.

6 C. Fang-Yen, M. Wyart, J. Xie, R. Kawai, T. Kodger, S. Chen, Q. Wen and A. D. T. Samuel, *Proc. Natl. Acad. Sci. U. S. A.*, 2010, **107**, 20323–20328.

7 J. Korta, D. A. Clark, C. V. Gabel, L. Mahadevan and A. D. T. Samuel, *J. Exp. Biol.*, 2007, **210**, 2383–2389.

8 J. Sznitman, P. K. Purohit, P. Krajacic, T. Lamitina and P. E. Arratia, Biophys. J., 2010, 98, 617–626

9 J. Sznitman, X. Shen, P. K. Purohit and P. E. Arratia, Exp. Mech., 2010, **50**, 1303–1311

10 A. Sivasundar and J. Hey, *Genetics*, 2003, **163**, 147–157.

11 J. A. Dent, M. M. Smith, D. K. Vassilatis and L. Avery, *Proc. Natl. Acad. Sci. U. S. A.*, 2000, **97**, 2674–2679.

12 K. Nishikawa, A. Biewener, P. Aerts, A. N. Ahn, H. J. Chiel, M. A. Daley, T. L. Daniel, R. J. Full, M. E. Hale, T. L. Hedrick, A. K. Lappin, T. R. Nichols, R. D. Quinn, R. A. Satterlie and B. Szymik, *Intergr. Comp. Biol.*, 2007, **47**, 16–54.

13 M. Dimitriadi, J. Sleigh, A. Walker, H. C. Chang, A. Sen, G. Kalloo, J. Harris, T. Barsby, M. B. Walsh, J. S. Satterlee, C. Li, D. V. Vactor, S. A. Tsakonas and A. C. Hart, *PLoS Genet*, 2010, **6**, e1001172.

14 S. Brenner, *Genetics*, 1974, **77**, 71–94.

15 W. Wang, Y. Sun, S. Dixon, M. Alexander and P. J. Roy, *J. Lab. Autom.*, 2004, **14**, 269–276.

16 R. J. Martin, G. Bai, C. L. Clark and A. L. Robertson, Br. J. Pharmacol., 2003, 140, 1068–1076.

17 E. Devaney, A. Winter and C. Britton, *Trends Parasitol.*, 2010, **26**, 428–433.

18 G. Bao and S. Suresh, *Nat. Mater.*, 2003, **2**, 715–725.

19 J. Conia, B. Edwards and S. Voelkel, *J. Clin. Lab. Anal.*, 1997, **11**, 28–38.

20 K. C. Neuman and S. M. Block, *Rev. Sci. Instrum.*, 2004, **75**, 2787–2809.

21 K. Svoboda and S. M. Block. *Annu. Rev. Biophys. Biomol. Struct., 1994*, **23**, 247–285

22 G. T. Charras and M, A. Horton, *Biophys. J.*, 2002, **82**, 2970–2981.

23 M. G. Langer and A. Koitschev, Method. Cell. Biol., 2002, **68**, 141–169.

24 A. B. Mathur, A. M. Collinsworth, W. M. Reichert, W. E. Kraus and G. A. Truskey, *J. Biomech.*, 2001, **34**, 1545–1553.

25 J. N. Fass and D. J. Odde, *Biophys. J.*, 2003, **85**, 623–636.

26 J. Chen, B. Fabry, E. L. Schiffrin and N. Wang, *Am. J. Physiol. Cell Physiol.*, 2001, **280**, C1475–C1484.

27 R. M. Hochmuth, *J. Biomech.*, 2000, **33**, 15–22.

28 E. Evans and A. Yeung, *Biophys. J.*, 1989, **56**, 151–160.

29 C. G. Galbraith and M. P. Sheetz, *Proc. Natl. Acad. Sci. U. S. A.*, 1997, **94**, 9114–9118.

30 D.-H. Kim, P. K. Wong, J. Park, A. Levchenko and Y. Sun, *Annu. Rev. Biomed.*, 2009, **11**, 203–233.

31 C. L. Asbury, A. N. Fehr and S. M. Blcok, *Science*, 2003, **302**, 2130–2134.

32 J. M. Fernandez and H. B. Li, *Science*, 2004, **303**, 1674–1678.

33 N. Chronis, *Lab Chip*, 2010, **10**, 432–437

34 D. B. Weibel, W. R. DiLuzio and G. M. Whitesides, *Nat. Rev.Microbiol.*, 2007, **5**, 209–218.

35 A. C. Miller, T. R. Thiele, S. Faumont, M. L. Moravec and S. R. Lockery, J. Neurosci., 2005, **25**, 3369–3378.

36 J. Qin and A. R. Wheeler, *Lab Chip*, 2007, **7**, 186–192

37 S. R. Lockery, K. J. Lawton, J. C. Doll, S. Faumont and S. M. Coulthard, *J. Neurophysiol.*, 2008, **99**, 3136–3143.

38 C. B. Rohde, F. Zeng, R. Gonzalez-Rubio, M. Angel and M. F. Yanik, *Proc. Natl. Acad. Sci. U. S. A.*, 2007, **104**, 13891–13895.

39 K. Chung, M. M. Crane and H. Lu, *Nat. Methods*, 2008, **5**, 637–643

40 X. Heng, D. Erickson, L. R. Baugh, Z. Yaqoob, P. W. Sternberg, D. Psaltis and C. Yang, *Lab Chip*, 2006, **6**, 1274–1276

41 S. E. Hulme, S. Shevkoplyas, A. McGuigan, J. Apfeld, W. Fontana and G. M. Whitesides, *Lab Chip*, 2010, **10**, 589–597.

42 Y. Zhang, H. Lu and C. I. Bargmann, *Nature*, 2005, **438**, 179–184.

43 N. A. Croll, *J. Zool.*, 2009, **176**, 159–176.

44 C. J. Cronin, J. E. Mendel, S. Mukhtar, Y. M. Kim, R. C. Stirbl, J. Bruck and P. W. Sternberg, *BMC Genet.*, 2005, **6**, 5.

45 J. A. Carr, A. Parashar, R. Gibson, A. P. Robertson, R. J. Martin and S. Pandey, *Lab Chip*, 2011, **11**, 2385–2396

46 W. Shi , J. Qin , N. Ye and B. Lin, *Lab Chip*, 2008, 8, 1432–1435.

47 J. C. Doll, H. Nahid, N. Klejwa, R. Kwon, S. M. Coulthard, B. Petzold, M. B. Goodman and B. L. Pruitt, *Lab Chip*, 2009, 9, 1449–1454.

48 A. Ghanbari, V. Nock and W. Wang, *The 15th International conference on Mechatronics and Machine Vision in Practice*, 2–4 Dec. 2008, Auckland, New-Zealand, 680–685.

49 A. Kruusing, *Smart Mater. Struct.*, 2000, **9**, 186–196.

50 S. A. Syed Asif, K. J. Wahl and R. J. Colton, *Rev. Sci. Instrum.*, 1999, **70**, 2408–2413.

51 A. F. Oskooi, D. Roundy, M. Ibanescu, P. Bermel, J. D. Joannopoulos and S. G. Johnson, *Comput. Phys. Commun.*, 2010, **181**, 687–702.

52 Y. Xia and G. Whitesides, *Annu. Rev. Mater. Sci.*, 1998, **28**, 153–184.

53 L. Dong, A. K. Agarwal, D. J. Beebe and H. Jiang, *Nature, 2006,* **442**, 551–554.

54 V. Lien and F. Vollmer, *Lab Chip*, 2007, **7**, 1352–1356.

55 M. Albonico, V. Wright, M. Ramsan, H. J. Haji, M. Taylor, L. Savioli and Q. Bickle, *Int. J. Parasitol.*, 2005, **35**, 803–811.

56 A. Diawara, L. J. Drake, R. R. Suswillo, J. Kihara, D. A. Bundy, M. E. Scott, C. Halpenny, J. R. Stothard and R. K. Prichard, *PLoS Negl. Trop. Dis.*, 2009, **3**, e397.

57 H. P. Tang, C. Ho and S. S. Lai, *Rapid Commun. Mass Spectrom.*, 2006, **20**, 2565–2572.

58 P. Rezai, A. Siddiqui, P. R. Selvaganapathy and B. P. Gupta, *Lab Chip*, 2010,**10**, 220–226.

59 P. Rezai, A. Siddiqui, P. R. Selvaganapathy and B. P. Gupta, *Appl. Phys. Lett.*, 2010, **96**, 153702.

CHAPTER 3

MICRO-ELECTRO-FLUIDIC GRIDS FOR NEMATODES: A LENS-LESS, IMAGE-SENSOR-LESS APPROACH FOR ON-CHIP TRACKING OF NEMATODE LOCOMOTION

A paper published in Lab on a Chip

Peng Liu, Richard J. Martin and Liang Dong

3.1 Abstract

This paper reports on the development of a lens-less and image-sensor-less micro-electro-fluidic (MEF) approach for real-time monitoring of the locomotion of microscopic nematodes. The technology showed promise for overcoming the constraint of the limited field of view of conventional optical microscopy, with a relatively low cost, good spatial resolution, and high portability. The core of the device was microelectrode grids formed by orthogonally arranging two identical arrays of microelectrode lines. The two microelectrode arrays were spaced by a microfluidic chamber containing a liquid medium of interest. As a nematode (e.g., *Caenorhabditis elegans*) moved inside the chamber, the invasion of its body parts into some intersection regions between the microelectrodes caused changes in electrical resistance of these intersection regions. The worm's presence at or absence from a detection unit was determined by a comparison between the measured resistance variation of this unit and a pre-defined threshold resistance variation. An electronic readout circuit was designed to address all detection units and read out their individual electrical resistance. By this means, it was possible to obtain the electrical resistance profile of the whole MEF grids, and thus, the physical pattern of the swimming nematode. We studied the influence of a worm's body on the resistance of an addressed unit. We also investigated how the full-frame scanning and

readout rate of the electronic circuit and the dimensions of a detection unit posed an impact on the spatial resolution of the reconstructed images of the nematode. Other important issues, such as the manufacturing induced initial non-uniformity of the grids and the electrotaxic behaviour of nematodes, were also studied. A drug resistance screening experiment was conducted by using the grids with a good resolution of 30 × 30 μm^2. The phenotypic differences in the locomotion behaviours (e.g., moving speed and oscillation frequency extracted from the reconstructed images with the help of software) between the wild-type (N2) and mutant (*lev-8*) *C. elegans* worms in response to different doses of the anthelmintic drug, levamisole. The locomotive parameters obtained by the MEF grids agreed well with those obtained by optical microscopy. Therefore, this technology will benefit the whole-animal assays by providing a structurally simple, potentially cost-effective device capable of tracking the movement and phenotypes of important nematodes in various microenvironments.

3.2 Introduction

The microscopic nematode *C. elegans* is an important genetic model to address fundamental questions in developmental biology, neurobiology, and behavioural biology.[1,2] The locomotion behaviours of *C. elegans* are under complex neuronal regulation and affected by a plethora of factors such as chemicals, temperature, light, electric field, and age.[3] Tracking and analysis of the locomotive parameters (e.g., travelled distance, speed, amplitude, and oscillation frequency) of *C. elegans* and other important microscopic nematodes is crucial to provide the mechanistic correlation between the genotype and phenotype of the nematodes under various environmental conditions.[4] Optical microscopic imaging technique is essential for observing and extracting movement information from live

nematodes.[5-11] Conventional bench-top microscope, along with a digital camera and tracking software program, is a popular means of detecting the locomotive parameters of microscopic nematodes. The optical imaging system and the worm test vials or plates are independent of each other. This microscope-camera setup can provide very detailed information about the behaviours of nematodes. But, the relatively high cost and large footprint of the setup are not well suited for integration into a portable system-on-chip device. Besides, the limited field of view of the objective lens in the microscope makes it often difficult to simultaneously monitor multiple experiments in multi-well culture plates without an automated, high-resolution motorized moving stage.[12] This may become problematic when quantitative measurements are needed on a large number of nematodes at a single nematode resolution. Therefore, there is a great need of developing a cost-effective and structurally simple detection mechanism that potentially will have no any limitation to the field of view.

Microfluidics is an attractive technology with the potential to streamline workflows and processes in the biomedical and health sciences.[13-15] Due to the small size of microscopic nematodes such as *C. elegans*, there is growing interest in studying the nematodes in the area of microfluidics and lab on a chip.[16-41] Many promising microfluidic technologies have been reported for culturing, manipulating, and analysing nematodes, including an automated microfluidic compact disc cultivation system,[19] an artificial soil substrate for rapid delivery of fluid-borne stimuli to worms,[20] a microfluidic device for directing worm movement and sorting worms based on the electrotaxic effect,[21,22] a microdroplet technology for encapsulating individual worms for toxicology bioassays,[23,24] a miniature worm clamping device for facilitating imaging and laser-mediated microsurgery,[25-32] a microfluidic device for engineering various microenvironments for study of the sensory neuron and behavioral

activity of nematodes,[33-36] a force sensing pillar array for biomechanical measurements of nematodes,[37] a micro-maze for examining the behaviours of nematodes,[38] a microchamber array for behaviour-based chemical screening with precise temporal control of stimuli,[39] and a microfluidic device capable of recording electrophysiological signals of multiple worm immobilized inside microchannels.[40] Recently, we also developed an optofluidic device for detecting muscular force generation of nematodes in response to various chemical environments.[41] On the other hand, in order to monitor dynamic behaviours of live microorganisms with low cost and high throughput, several on-chip *optical* imaging technologies have recently been developed.[42-45] A remarkable technology is the optofluidic microscope (OFM).[42-44] The microorganism sample of interest is transferred into a channel and then imaged by a complementary metal-oxide-semiconductor (CMOS) or charge-coupled-device (CCD) image sensor chip. An array of small circular apertures is located on top of the image sensor chip, spanning across the whole channel. When the channel is illuminated by an external light source, the sample casts a shadow on the image sensor and the time resolved transmission signal is converted into the spatial information of the sample. Some variations of the OFM device have been developed such as the sub-pixel resolving OFM,[45] and the fluorescent OFM with a high submicron resolution.[46-48] Another excellent optical imaging technique for microfluidic applications is the digital in-line holography (DILH).[49-55] In this technology, a channel device contains the microorganism of interest and is placed between the light source and the recording plane of a CMOS/CCD image sensor. The light source is spatially filtered by a pinhole to increase the coherence length. The scattering wave from the sample interferes with a reference wave from the light source. Thus, a hologram or interference pattern is formed by the superposition of the two wave fronts for

digital recording. Another representative technique for optical imaging of microorganisms is the lens-less, wide-field monitoring array based on the shadow imaging principle, while also relies on using a CMOS/CCD image sensor.[56,57] The device has been shown to detect and count thousands of individual cells in real time. Despite the considerable progress in the development of compact on-chip imaging-based tracking systems for microfluidic applications, almost all of the existing technologies essentially utilize the optical effects, such as shadow and interference patterns due to the presence of microorganisms, and thus, inevitably require a sophisticated imaging sensor chip, along with a light source, for observation.

In this paper, we report on the development of a *non-optical*, integrated device for on-chip detection of the locomotion behaviours of nematodes, with a cost-effective and simple architecture, and fair spatial resolution. The present technology requires no lens or image sensor chip. The core of the device consists of two identical linear arrays of thin-film microelectrodes arranged orthogonally on two glass slides. Each microelectrode array has N periodically spaced electrode strips. Thus, $N \times N$ intersection regions are formed between the upper and lower microelectrode arrays. A microfluidic chamber is created between the two glass slides, where a worm under test will swim freely (see a video clip in Electronic Supporting Information). As the nematode moves inside the microfluidic chamber, its body may appear in several intersection regions of the microelectrodes. Because the electrical resistivity of the worm's body is often different from that of the surrounding medium, a resistance change is detected at an intersection region that indicates the presence of part of the worm's body near the intersection region. By electrically addressing all intersection regions and probing their individual resistances in a short time period (before the worm

changes its posture) using an electronic scanning and readout circuit, it is possible to get the electrical resistance profile, and thus, the physical pattern, of the moving nematode. Generally, microscopic nematodes such as *C. elegans* move relatively slow and exhibit a sinusoidal pattern induced by alternating dorsal and ventral muscle contraction. *C. elegans* swims with an oscillation frequency (f_{worm}) ranging from a fraction of one Hz to several Hz. As discussed later, by increasing the full-frame scanning frequency (f_{sc}) of the electronic circuit, the swimming nematode under test could be treated as a static object during a measurement cycle of $t_{sc} = 1 / f_{sc}$. This enabled us to obtain the movement patterns or behavioural information of the nematode in a quasi-real time manner. To prevent the electrotaxic behaviour of the worms (moving toward the cathode) and the electrokinetic effects (electrophoresis of the worms and electro-osmosis of the surrounding fluid) within the MEF grids, the electric field applied between two orthogonal microelectrodes for the resistance measurement was set to be lower than the threshold field strength of the electrostatic and electrokinetic effects, which will be discussed later.

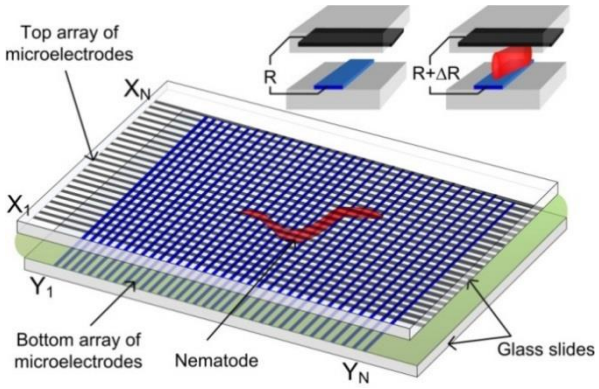

Fig. 3.1 Schematic of the proposed MEF grids for detecting the locomotion behaviours of microscopic nematodes.

3.3 Methods and Experimental Details

3.3.1 Theoretical estimation

We first theoretically estimated how the presence of part of the worm's body affected the electrical resistance of an addressed intersection region of the microelectrodes. The three-dimensional finite element analysis (FEA) method based on the commercial software COMSOL was employed for this simulation. The variables *W* and *D* denote the width of microelectrode and the spacing between two neighbouring microelectrodes, respectively (Fig. 3.2a). A detection unit or an image pixel was constructed by extending *D* / 2 from each side of an intersection region (see the white dashed line square in Fig. 3.2a), covering a square area with the side length of *D* + *W*. Thus, the centreline between any two neighbouring microelectrodes on the glass substrate served as the boundary of detection units. A microfluidic chamber was formed between the upper and bottom glass slides. The depth or height of the chamber was set to be *H* = 50 μm because generally, L1-L4 stage *C. elegans* larvae is no more than 50 μm in diameter. The side length of detection unit was set to be *D* + *W* = 30 μm. For simplification of the FDTD analysis, *D* = *W* = 15 μm.

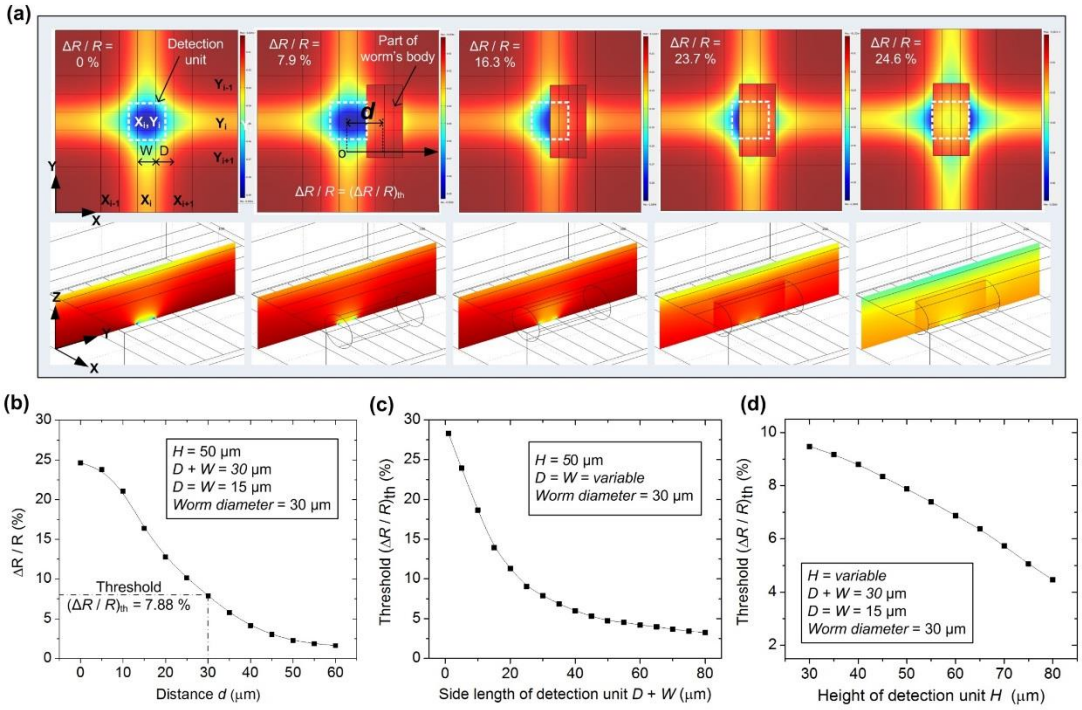

Fig. 3.2 (a) Simulated electric field distributions at the X-Y plane (upper row) and Z-Y plane (lower row) of the MEF grids as the worm's body part appears at different locations relative to an addressed detection unit. *d* is denoted as the planar centre-to-centre distance *d* between the worm's body part and the intersection region. From left to right: $d = \infty$, 30 μm, 15 μm, 5 μm, and 0. For simplification, part of a nematode's body was modelled by a 60 μm long, 30 μm diameter cylinder laid on side within the grids. The height or depth of the grids was set to be H = 50 μm. The side length of detection unit was set to be $D + W$ = 30 μm with $D = W$ = 15 μm. The field distributions in the upper row were observed at the planar central plane H / 2 above the lower substrate of the device. The field distributions in the lower row were observed at the Z-Y plane across the spatial centre of the unit (Xi, Yi). (b) Simulated relative resistance variation $\Delta R / R$ as a function of *d*. (c) Simulated threshold relative resistance variation $(\Delta R / R)_{th}$ as a function of a side length $D + W$ of a detection unit with $D = W$ and H = 50 μm. (d) Simulated $(\Delta R / R)_{th}$ as a function of a depth of the grids or H with $D + W$ = 30 μm and $D = W$.

Modelling a whole nematode flexibly moving inside the MEF grids was fairly difficult due to the changing body posture of the nematode over time. Here, we used a 60 μm long and 30 μm diameter cylinder (laid on side within the grids) to represent just part of the worm's body interacting with a selected detection unit. The planar coverage area of the cylinder (30 μm × 60 μm) was thus twice that of the detection unit (30 μm × 30 μm). We found that the simulation results with a cylindrical object longer than 60 μm was almost the

same as those with the 60 μm long cylinder used here. The electrical resistivity of the worm's body and of the M9 buffer (or the medium in the microfluidic chamber) was ~350 Ω·cm and ~104 Ω·cm, respectively. Fig. 3.2a shows that as the worm's body part moved toward the spatial centre of the selected detection unit, the electric field distributions inside and outside of this unit significantly changed and the electrical resistance R measured at this unit increased ($\Delta R > 0$). When the body part completely overlapped the intersection region, the simulated maximal relative resistance variation $\Delta R / R$ reached 24.6 %. However, to distinguish between the worm's presence at and absence from a detection unit, we defined the threshold relative resistance variation $(\Delta R / R)_{th}$ as the critical $\Delta R / R$ detected when the worm reached the boundary of the selected unit (see the 2nd panel of Fig. 3.2a). The simulated value of $(\Delta R / R)_{th}$ was ~7.9 %, below which the body part could be interpreted to be outside of the unit, and above which the body part was considered to be inside the unit. As we can see later, there inevitably existed a certain level of the manufacturing induced initial resistance variation between all detection units. Therefore, only if the absolute value of $(\Delta R / R)_{th}$ or $|(\Delta R / R)_{th}|$ was greater than the original resistance variation, the MEF grids device would be able to detect the presence of a worm's body part at a detection unit. Figs. 3.2c and 3.2d show the influence of the side length $D + W$ and the height H of the detection unit on $(\Delta R / R)_{th}$. The results indicate that having a small $D + W$ would lead to a high $(\Delta R / R)_{th}$. This could make it easier and more accurate to detect the presence/absence of a worm's body part. Also, as the depth of the detection unit increased from 30 μm to 80 μm, the simulated $(\Delta R / R)_{th}$ was found to significantly decrease from 9.4 % to 4.3 %. Although using a low H was preferable, the minimum H was determined by the body diameter of the worm under test. It is also important to point out that the proposed lens-less, image-sensor-less detection

approach can work not only for larval stage (L1-L4) *C.elegans*, but for young adult and older ones (that can get as thick as ~100 μm) by increasing *H*.

3.3.2 Fabrication for microelectrode grids

To fabricate a microelectrode array, a 10 nm thick titanium (Ti) layer and a 250 nm thick gold (Au) layer were deposited on a glass slide using e-beam evaporation. The Ti layer was used to improve adhesion between the Au layer and the glass slide. The Ti-Au composite layers were then patterned by conventional photo-lithography, followed by chemical wet etching with Au etchant (GE-8148, Transene). Two identical microelectrode arrays were formed on two respective glass slides by using this method. To control the depth of a microfluidic chamber between the two arrays, SU-8 photoresist (SU-8-50, MicroChem) was used to form a fence along the edges of one glass slide. Lastly, the MEF grids were formed by placing the two microelectrode arrays face-to-face and orthogonal to each other (Fig. 3.3a).

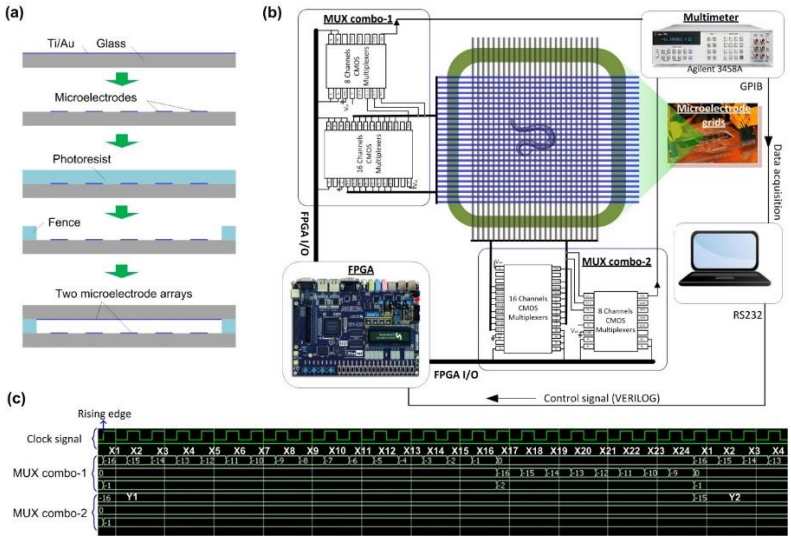

Fig. 3.3 (a) Fabrication processes for the microelectrode grids: deposition of Ti and Au → patterning of microelectrodes → patterning of photoresist fence → assembly of the device by orthogonally stacking two identical microelectrode arrays under microscope. (b) Architecture of the electronic circuit for the grids. (c) Representative digital signals for addressing detection units on the chip.

3.3.3 Full-frame scanning and readout electric circuit

Fig. 3.3b shows the architecture of the electronic circuit designed for the fabricated MEF grids (24 rows and 24 columns). A field programmable gate array or FPGA (Altera Cyclone II) was used and programmed to respectively control a vertical and a horizontal multiplexer (MUX) combo for addressing individual detection units. The electrical resistance of an addressed detection unit was readout by a multimeter (3458A, Agilent) with 100000 readings s^{-1}. The multimeter communicated with data acquisition and analysis software through the parallel general purpose interface bus (GPIB) transceiver. To adjust *timing* with the multimeter, the FPGA was interfaced with the software using the series RS232 communication protocol.

To verify the timing properties of the hardware design, the timing simulation was performed on the ModelSim platform. Fig. 3.3c shows part of the timing result as an example. The horizontal microelectrode Y_1 was selected by the MUX combo-2. The vertical microelectrodes from X_1 to X_{24} were sequentially selected by the MUX combo-1 at each raising edge of the clock. Thus, the 24 detection units ((X_1, Y_1), (X_2, Y_1), …, (X_{24}, Y_1)) in row Y_1 were addressed one by one. This allowed the multimeter to read out their electrical resistance. To obtain the full-frame resistances, this process described above needed to repeat 24 times, taking a period time of $t_{sc} = 24 \times 24 \times T_{CLK}$ where T_{CLK} was the clock period. We note that T_{CLK} can be adjusted by the hardware (FPGA) and software (Verilog hardware description language). The typical value of T_{CLK} was 10 μs, obtained by dividing the on-board oscillator frequency f_{osc} (Cyclone II FPGA has f_{osc} = 50 MHz) by an integer m (m = 500 was chosen here) via coding in Verilog.

3.3.4 Image reconstruction and parameter extraction

The electrical resistance matrix $R_{i,j}$ of order $N \times N$ was obtained by reading out the resistances of all detection units, where $R_{i,j}(t)$ ($i, j = 1, 2, \ldots, N$) represented the resistance of the detection unit at the intersection of line i and row j at time t. Then, the resistance variation matrix $\Delta R_{i,j}(t)$ was calculated by $\Delta R_{i,j}(t) = R_{i,j}(t) - R_{i,j}(t_0)$, where $R_{i,j}(t_0)$ was the original resistance matrix at $t_0 = 0$ without worm introduced. Lastly, the relative resistance variation matrix $\Delta R_{i,j}(t) / R_{i,j}(t)$ was obtained for the image reconstruction. To convert the matrix $\Delta R_{i,j}(t) / R_{i,j}(t)$ to a grayscale image, we used the function "mat2gray" in the MATLAB image processing toolbox to apply a linear scaling and offset to the matrix. The minimum value was mapped to 0 (black) and the maximum value was mapped to 1 (white). Other values in the matrix were linearly scaled into corresponding grayscale values. Thus, the grayscale image of the matrix $\Delta R_{i,j}(t) / R_{i,j}(t)$ was formed. To convert the matrix $\Delta R_{i,j}(t) / R_{i,j}(t)$ to a binary image, each element value in the matrix was compared with the threshold $(\Delta R/R)_{th}$. When $\Delta R_{i,j}(t) / R_{i,j}(t) < (\Delta R / R)_{th}$, a binary 0 (black) appeared at the pixel of the reconstructed image. In contrast, when $R_{i,j}(t) / R_{i,j}(t) > (\Delta R/R)_{th}$, a binary 1 (white) appeared at the pixel. To display a pseudocolour map of the matrix for an input data set, the function "corrmap.m" of the MATLAB was used.

The motility parameters were analysed by using the worm tracking program we previously developed for a microscope-camera tracking system.[41,58] Briefly, the binary images were sequenced and compressed into the Audio Video Interleave (.avi) video format. The .avi video was post-processed by a worm tracking program that was able to extract track signatures and locomotion (e.g., number and duration of stops, and cut-off region) of individual and/or worms. The program analysed a large number of images to recognize a moving object (here worm), and then, extract motility parameters such as amplitude,

wavelength, oscillation frequency, body postures, path traversed by the worm, and average moving velocity.

3.3.5 Optical tracking system for comparison purposes

To compare the reconstructed images based on the MEF grids approach and their corresponding optical images, we used a stereo microscope (MZ205, Leica) equipped with a video camera (QICamera) to capture a series of digital images (1392 × 1040 pixels) at a specific time interval of 66.7 ms. The motility parameters of worms were extracted by using the worm tracking programmed aforementioned.

3.3.6 Nematodes and liquid medium

C. elegans worms (wild-type N2 and levamisole resistant ZZ15 *lev-8*) were obtained from the *Caenorhabditis* Genetics Centre at University of Minnesota (St. Paul, MN). They were cultivated at 25 °C on Nematode Growth Medium plates seeded with *Escherichia coli* OP50 bacteria. For the experiments, the worms were picked using a sterilized platinum wire and transferred to the microfluidic chamber through an opening in the top glass slide of the MEF grids.

To test how nematodes changed their locomotion behaviours in the anthelmintic drug levamisole. The levamisole solutions with different concentrations were prepared by dissolving levamisole stock solution with appropriate amounts of the M9 buffer solution. The recipe for the M9 buffer (3 g KH_2PO_4, 6 g Na_2HPO_4, 5 g NaCl, 1 mL 1 M $MgSO_4$, and H_2O to 1 L) was a standard recipe taken from the Wormbook.[59]

3.3.7 Resistivity of nematodes

In the FEA simulation mentioned above, the electrical resistivity of nematodes was set to be 350 Ω·cm. This resistivity value was estimated by inversely calculating from the

measured total resistance of a detection unit when the worm's body was positioned at the planar spatial centre of the detection unit (as we will see later in Fig. 3.5). Specifically, different values of electrical resistivity for the worm's body were fed into the FEA software COMSOL to approach the measured total resistance of the detection unit. When the discrepancy between the simulated and experimental resistance of the detection unit was less than ± 1 %, the corresponding resistivity of the worm used in the simulation was regarded as the actual resistivity of the worm. It should be noted that no obvious change was found in the body resistivity of the worms at different stages (L1-L4).

3.4 Results and Discussion

Fig. 3.4 shows the original distribution of the electrical resistance of the 24 × 24 MEF grids with the M9 buffer as a medium but with no worm introduced. The microelectrodes used here were 15 µm wide and 15 µm spaced. The readout time for this whole resistance matrix was t_{sc} = 5.76 ms at f_{sc} = 174 Hz. The result shows that the initial relative variation between the maximum and minimum resistance was ~3.3 %, reflecting the manufacturing-induced non-uniformity of the microelectrode geometry and dimensions.

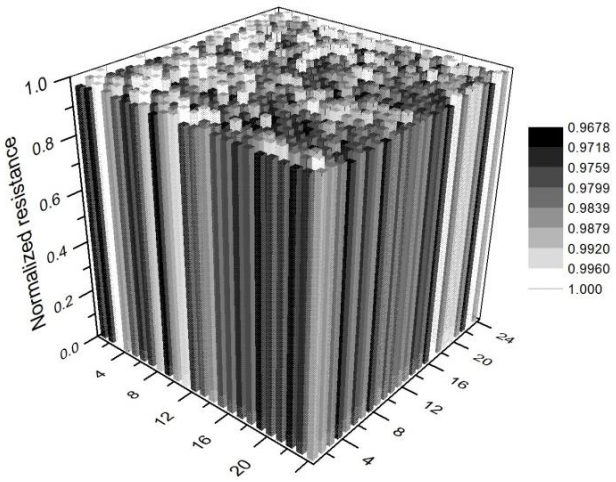

Fig. 3.4 Initial electrical resistance distribution of the fabricated 24 × 24 grids with $W = D$ = 15 µm. No worm was introduced to the grids.

To obtain an actual value of $(\Delta R / R)_{th}$ for a nematode *C. elegans* swimming in the M9 buffer solution, a L3-stage worm (~30 μm diameter, and ~591 μm long) was introduced to the MEF grids operating at f_{sc} = 174 Hz. Particularly, we examined the electrical resistances detected at different detection units near the nematode at a time point. The distance between an addressed unit and certain body part of the worm was measured by using the optical image recorded by the stereo microscope at the same time point. Fig. 3.5a shows that when the body edge of the worm was on the boundary line of the unit, the experimental value of $(\Delta R / R)_{th}$ was found to be 8.1 ± 1.7 % (mean ± standard deviation, obtained from 60 resistance data obtained at 5 detection units). It is also obvious that as the nematode invaded deep into an addressed detection unit, the measured $\Delta R / R$ of this unit increased. The maximum value of $\Delta R / R$ = 22.4 ± 1.8 % occurred when the detection unit was completely covered by the worm. Compared to the simulated plot of the $\Delta R / R$ vs. distance given in Fig. 3.2b, the experimental result showed a relatively good agreement with the simulated result. The discrepancy was probably caused by the simplified model used in the FEA study and the measurement error in the locations of the worm's body part and its distance to an addressed unit. The histogram of the distribution of $(\Delta R / R)_{th}$ over 226 grids is given in Fig. 3.5b, showing a Gaussian-like distribution between 6.5 % and 10.5 %. We note that although there were a total of 24 × 24 = 576 grids in the MEF device, it was almost impossible for a worm to swim over with all grids.

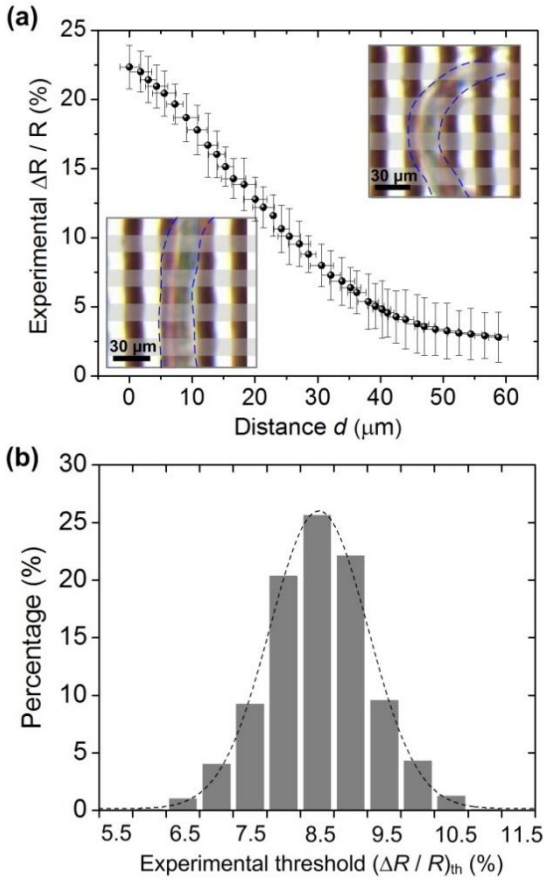

Fig. 3.5 (a) Experimental result of $\Delta R / R$ as a function of d. d is the planar centre-to-centre distance between the worm's body part and the intersection region. Two insets show the close-ups of a nematode swimming inside the MEF grids. The blue dashed lines outline part of the worm's body parts. X and Y error bars represent standard deviations of the mean value of d and $\Delta R / R$, respectively, from 60 resistance data obtained at 5 detection units. (b) Histogram of the distribution of $(\Delta R / R)_{th}$ in the MEF grids. The distribution was plotted based on the value of $(\Delta R / R)_{th}$ obtained at 226 grids.

It should be pointed out that the experimental $(\Delta R / R)_{th}$ of 8.1 % was much higher than the manufacturing induced maximum original resistance variation of 3.3 %. Thus, we used $(\Delta R / R)_{th}$ = 8.1 % to distinguish between the presence and absence of a nematode relative to a detection unit during reconstructing a binary image of the nematode. In fact, one could also subtract the manufacturing-induced "background" profile (Fig. 3.4) from the actual resistance profile of the grids to blank out the heterogeneity of the original resistance. This, in principle, would allow for a better representation of the reconstructed nematode

image. Here, because the value of $(\Delta R / R)_{th}$ was much higher than the maximum original resistance variation of the grids, we did not do subtraction operation in this work. It should be also pointed out that the reconstruction of the grayscale and pseudo colour images of a nematode was independent of the actual value of $(\Delta R / R)_{th}$.

Fig. 3.6 shows the time-lapse optical images and corresponding reconstructed pseudo colour, grayscale, and binary images of a moving *C. elegans* (L3) in the MEF grids. The device operated at f_{sc} = 174 Hz and tracked the changes in shape and position of the worm over time. The reconstructed images were then analysed by the worm tracking program. It was found that the oscillation frequency and moving speed of the worm was f_{worm} = 1.8 ± 0.3 Hz and v_{worm} = 270 ± 21 μm s^{-1}, respectively (mean ± standard deviation, n = 12 worms). For comparison purposes, the optical microscope-camera setup was used to track the nematodes of the same developmental stage swimming in a 1-inch Petri dish containing the same M9 buffer. The optical measurement revealed that f_{worm} = 1.9 ± 0.3 Hz and v_{worm} = 266 ± 17 μm s^{-1} (mean ± standard deviation, n = 12 worms), which were almost the same as those obtained by the MEF grids. Therefore, the present device was able to obtain the locomotion information for reconstructing the real-time images of nematodes for post-analysis of locomotive parameters.

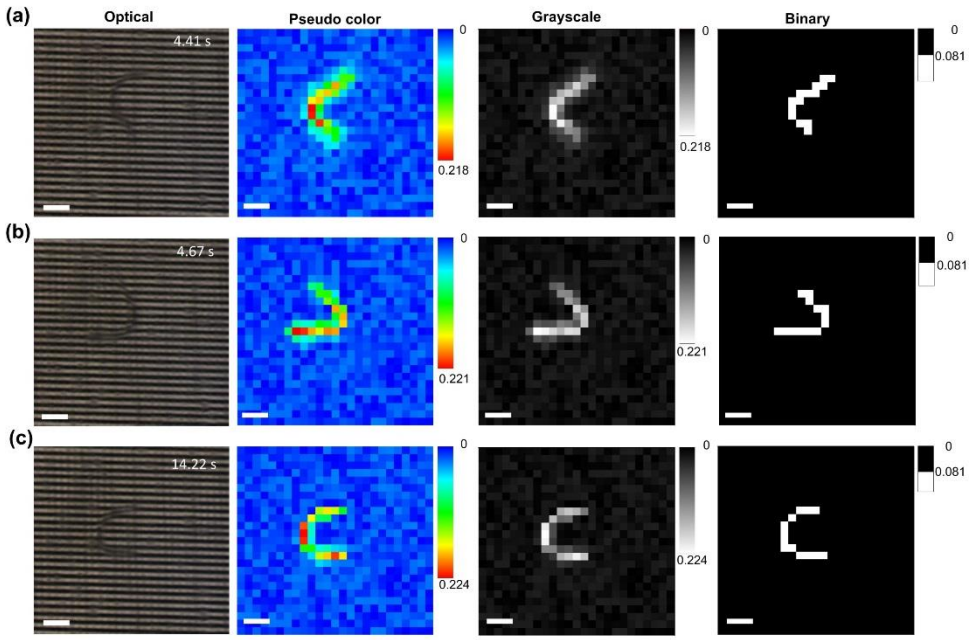

Fig. 3.6 Optical images and corresponding reconstructed pseudo colour, grayscale, and binary images of a *C. elegans* swimming in the MEF grids. The full-frame scanning frequency was f_{sc} = 174 Hz. The pseudo colour, grayscale and binary images were obtained from the electrical measurements. Scale bars represent 100 μm.

The accuracy of detecting the position and shape of a moving nematode highly depended on the full-frame scanning rate f_{sc} of the electronic circuit designed. Suppose that the device has $N \times N$ grids and the multimeter used in the system has a reading speed of n readings s^{-1}. Thus, the allowable maximum f_{sc} is $n / (N \times N)$ Hz or the electronic circuit takes $(N \times N) / n$ seconds to read out all $N \times N$ resistances. Furthermore, suppose that the nematode under test has the moving speed of v_{worm} and the body wavelength of λ that can maximally crosses x number of microelectrodes in a direction. Thus, $\lambda = x\,(D + W)$. As a result, the electronic circuit spends $t_{act} = (x / N) \times (N \times N / n) = x \times N / n$ seconds on reading out the resistances of the detection units across over the nematode. Within the time period of t_{act}, the worm may shift a maximum distance of $\Delta l = v_{worm} \times t_{act} = (v_{worm} \times \lambda \times N) / (n \times (D + W))$. It is obvious that the lower the value of Δl, the higher the accuracy of detecting the position and shape of the moving object. By using a smaller number of microelectrodes N in the grids, the

electronic circuit can complete reading the $N \times N$ resistance matrix faster, thus decreasing the value of Δl. However, it is noted that the minimum number of microelectrodes on each glass slide is determined by λ of the nematodes. Generally, larval stage *C. elegans* has the *total* body length of $L \leq 1$ mm and moves at a speed of $v_{worm} \leq 500$ μm s^{-1}. The present device was designed by taking half the total body length as the body wavelength or $\lambda \leq$ ~500 μm. Therefore, by choosing $N = 24$ and $D = W = 15$ μm, the grids could cover an area of 720 × 720 μm^2 that allowed larval stage *C. elegans* to move within the grids. Because the multimeter used here had $n = 100000$ readings s^{-1}, the maximum f_{sc} was set to be 174 Hz, resulting in a theoretical maximum value of Δl = ~2 μm. We note that it was quite hard to obtain experimental Δl in a short time of $t_{act} = x \times N / n = (500 / (15 + 15)) \times 24 / 100000 = 4$ ms. According to Fig. 3.5, a lateral shift of ~2 μm from the boundary of a detection unit may cause an erroneous variation in $\Delta R / R$ of ~0.4 %, which was much lower than the experimental $(\Delta R / R)_{th} = 8.1$ %. Therefore, by appropriately setting the operation frequency of the device, the body movement induced erroneous variation during a full scanning cycle had little influence on the accuracy of tracking the nematodes, which was already demonstrated in Fig. 3.6. In fact, for a given electronic readout circuit, operating the device at the maximum $f_{sc} = n / (N \times N)$ Hz could be easily achieved, simply by programming the hardware language (Verilog) on the computer. Fig. 3.7 demonstrates that the quality of reconstructed images varied with changing f_{sc}. We found that when $f_{sc} < 10 \times f_{worm}$, the nematode was displayed as the scattered white spots in the reconstructed binary image (Fig. 3.7a). This is because the nematode moved considerably during a full scanning cycle. Thus, no valuable information about worm activities was obtained. Increasing f_{sc} to 70~80 × f_{worm} allowed these distributed spots to get closer, but the reconstructed image of the nematode

was still fragmented (Fig. 3.7b). When f_{sc} increased to be more than 80 × f_{worm}, a continuous body shape of the nematode was obtained (Fig. 3.7c).

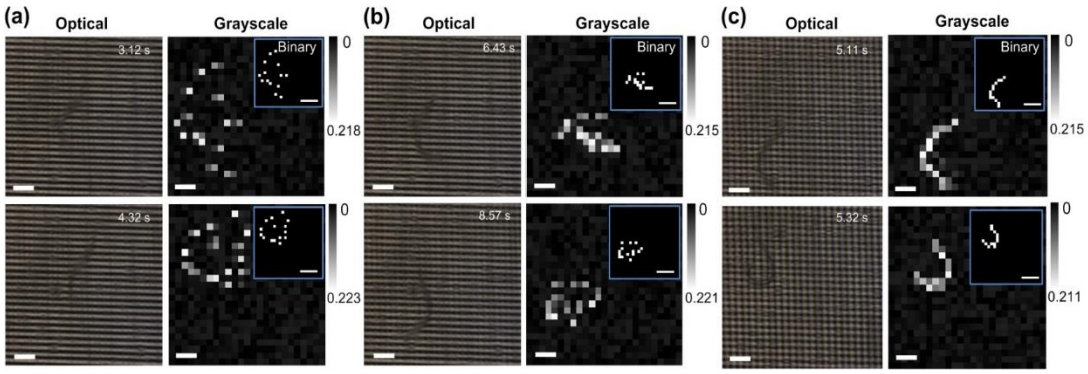

Fig. 3.7 Optical images and reconstructed grayscale, and binary images of a *C. elegans* swimming in the MEF grids at two different time points with different full-frame scanning frequency f_{sc} = 8 Hz (a), 70 Hz (b), and 100 Hz (c). The grayscale and binary images were obtained from the electrical measurements. Scale bars in the optical and grayscale images represent 100 µm. Scale bars in the binary images (see insets) represent 200 µm.

The pixel resolution of the reconstructed images decreased with increasing the value of $D + W$. Here, we designed another MEF grids device with $D = W$ = 50 µm, 24 microelectrodes on each glass slide, and 50 µm gap between the two glass slides. The device still operated at f_{sc} = 174 Hz. A L3-stage *C. elegans* was introduced in the microfluidic chamber containing the M9 buffer. Similarly, by using the same method mentioned above, $(\Delta R / R)_{th}$ was found to be 3.8 ± 0.9 % in this case, which was close to the simulated ~3.5 % and greater than the manufacturing induced intrinsic resistance variation of ~3 % of this device ($D = W$ = 50 µm). Thus, this device could determine the presence/absence of the nematode in the detection units as shown in Fig. 3.8b. However, although the movement of the nematode was detected, the use of the large-size detection unit resulted in the coarse images with only 5-7 pixels to outline the nematode in each image. Detailed information about the shape of the nematode was lost. We note that with the relatively low spatial resolution, the worm tracking program could identify the position of the worm and analyse

its average moving speed, but was difficult to derive important locomotive parameters such as oscillation frequency, amplitude, and wavelength.

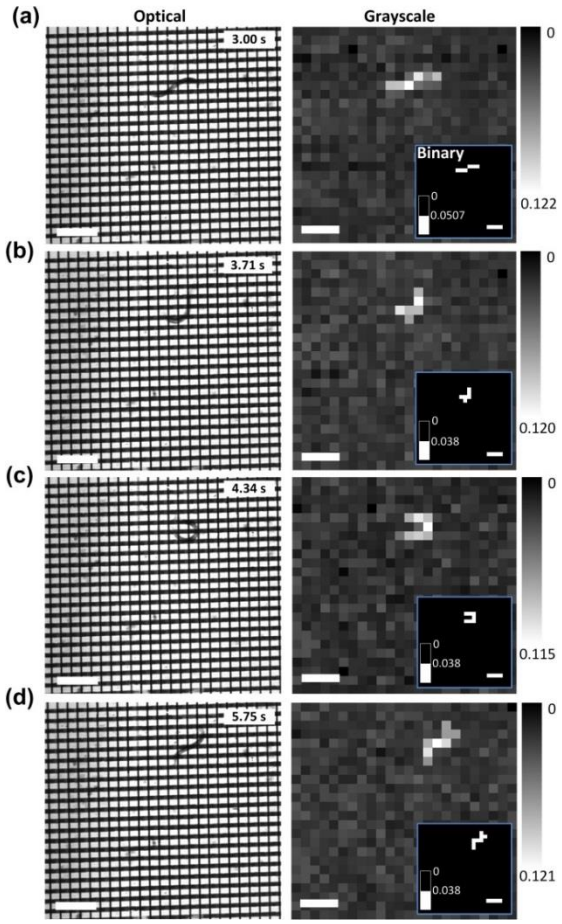

Fig. 3.8 Optical images and corresponding reconstructed grayscale and binary (inset) images of a *C. elegans* (L3) moving in the grids. The detection frequency was set to be at f_{sc} = 174 Hz. The grayscale and binary images were obtained from the electrical measurements. Scale bars represent 400 μm.

Other research has revealed that *C. elegans* at different developmental stages respond differently to electric field [21,22]. For example, early stage (L1 and L2) wild type *C. elegans* was little responsive to electric field with strength less than 13 V cm^{-1} before electrokinetic flows occurred. Whereas, L3, L4, and adult stage worms respond to electric field robustly starting from the threshold field strength of 4, 4, and 2 V cm^{-1}, respectively, by swimming towards the cathode. Thus, in order to use the present device for different larval

stage *C. elegans* without physiological and behavioral side effects, we adjusted the test voltage of the multimeter (the actual voltage applied to the microelectrodes was 8 mV), by using external series connected resistors and a potentiometer. This could ensure the electric field applied between the top and bottom microelectrodes to be as low as ~1.5 V cm^{-1}. Furthermore, we verified the responses of L1-L4 wild-type *C. elegans* to this electric field strength. Specifically, one of the bottom microelectrodes was set to be grounded, and also, an upper microelectrode was selected. Ten nematodes of each stage were respectively flowed to the microfluidic chamber. No directed swimming of the nematodes was observed at all five different stages. Fig. 3.9 shows f_{worm} and v_{worm} of the L1-L4 nematodes detected by both the present grids and the optical microscope-camera setup. The locomotive parameters were also derived and analysed by the worm tracking program. Since the two methods provided almost the same result, it was confirmed that the worms moving inside the grids were not affected by the applied low electric field and that the present electrical resistance measurement approach was effective and reliable to detect the locomotion behaviors of the nematodes.

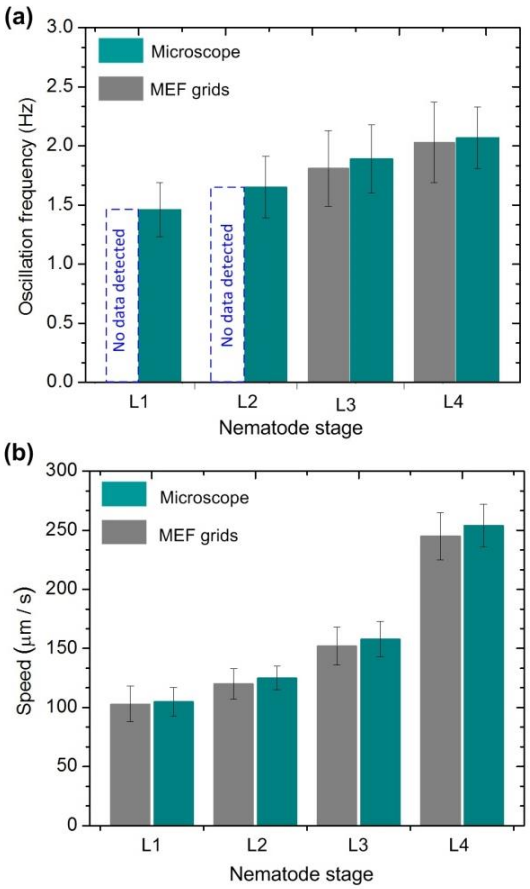

Fig. 3.9 Oscillation frequency (a) and moving speed (b) of wild-type *C. elegans* worms at different developmental stages (L1-L4) detected by using the present MEF grids and optical microscope. Due to the large D and W ($D = W = 15$ μm), the device was *not* able to detect the oscillation frequency of the L1-L2 stage worms. Error bars represent standard deviations of the mean oscillation frequency (a) and moving speed (b), respectively, from 12 worms.

To demonstrate further the workability of the present device, a drug resistance screening experiment was conducted by using the device with $D = W = 15$ μm and operating at $f_{sc} = 174$ Hz. In this experiment, the microfluidic chamber of the device was pre-filled by the anthelmintic levamisole with specific concentrations. The L3-stage wild-type N2 and mutant *lev-8 C.elegans* was respectively introduced into the chamber. Similarly, to verify the dose responses obtained by the MEF grids, the optical imaging-based locomotion tracking experiment was conducted in a Petri dish containing the same levamisole concentration solution. It is noted that even as the concentration of levamisole solution increased to a

considerably high value of 500 µM, the electrical resistivity of the worm and levamisole solution was little changed. Thus, we still used $(\Delta R / R)_{th} = 8.1$ % to distinguish the presence/absence of the worm's body part in a detection unit.

Fig. 3.10 displays the responses of the two different nematodes as a function of levamisole dose in terms of f_{worm} and v_{worm}. The result demonstrates that the response curves obtained by the present device were almost the same as those obtained by the microscope-camera method. Specifically, at the levamisole concentrations lower than 1.0 µM for N2 and 5.0 µM for *lev-8* nematodes, little reduction in f_{worm} or v_{worm} was observed. Increasing levamisole concentration caused to restrict their movement. The cut-off concentration was 105.4 µM for N2 and 155.3 µM for *lev-8,* at which almost all worms were paralyzed. The EC_{50} value (defined as the concentration that provokes a response half way between the basal and maximal response, of the agonist and compare for differences between isolates or strains) for levamisole was found to be ~20.2 µM for N2 worms, and ~38.7 µM for *lev-8* worms by the fitting curves in Figs. 3.11c-d. Therefore, the present grids device can play a useful role in many phenotypic bioassays that require real-time observation of the behavioural patterns of some microorganisms.

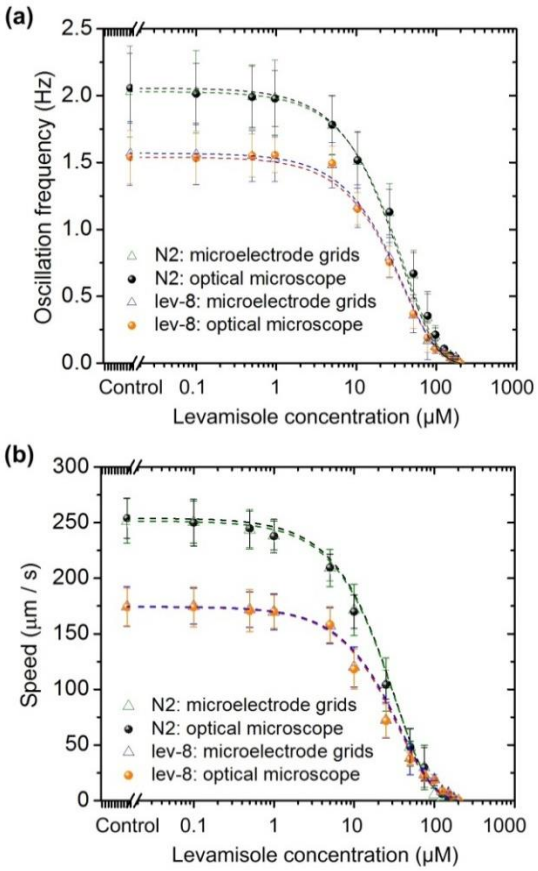

Fig. 3.10 Oscillation frequency (a) and moving speed (b) of L3-stage wild-type N2 and mutant *lev*-8 *C. elegans*. Error bars represent standard deviations of the mean oscillation frequency (a) and moving speed (b), respectively, from 15 worms.

There is much room to improve the performances of the MEF grids device. At the moment of this work, the obtained spatial detection resolution of the device was at the level of 30 × 30 μm^2, limited by our fabrication capability. The worm tracking program was able to extract the behavioural parameters such as moving speed and oscillation frequency based on the reconstructed images obtained over time. But, due to the limited spatial resolution, it was relatively difficult to extract other important parameters such as nematode's body amplitude. As a result, no accurate waveform of nematodes was obtained by this present device. Scaling down the grids will enable us to obtain higher resolution constructed worm images. It is interesting to address that using smaller detection units can result in a higher

value of $(\Delta R / R)_{th}$, making it easier and more accurate to detect the presence and absence of a worm's body. Specifically, by manufacturing the microelectrodes with the submicron feature size, our locomotion behaviour detection technology could overcome the optical diffraction limit in conventional optical microscopy. Furthermore, due to the limited area coverage by a small number of microelectrodes, the current version of the MEF grids device allowed a single worm to move freely inside the grids. Obviously, layout of more microelectrodes will allow for simultaneous abd high-throughput monitoring of multiple worms with no body interference between worms. However, in order to incorporate a large number of finer (e.g., submicron feature) microelectrodes into the next version of the device (with an aim of achieving a higher spatial resolution and larger capacity for detecting multiple worms), the electronic detection system needs a faster processing speed to read out more electrical resistance elements in parallel. The device presented here used a multimeter, in conjunction with the addressing circuit, to read the electrical resistance matrix of the MEF grids. A large-scale resistance readout circuit specific for the grids device is under development. Generally, it is possible to measure the electrical resistance of a resistor on a ~ns time scale by using integrated circuit technology. As revealed in Fig. 3.7, the whole-frame scanning frequency of $f_{sc} \geq 80$ Hz was required to track a moving nematode. It is thus possible to extend the number of microelectrodes on each glass slide to be $N = \sim (10^9 / f_{sc})^{1/2} = \sim 3500$. For example, a scaled-up MEF grids device with spatial resolution of 5×5 μm^2 will cover a large detection area of 1.75×1.75 cm^2. Moreover, thanks to the simplicity of the electrical measurement approach, we can further increase the detection area by using multiple of such MEFs in parallel. Finally, we believe it is also possible to detect nematode

locomotion information by finding out electrical capacitance profile of the MEF grids. The details of the results will be reported in another article.

3.5 Conclusions

In summary, we have demonstrated the MEF method of tracking the movement of nematode *C. elegans* based on the electrical resistance measurement for all grids. The 24 × 24 orthogonal grids were realized by conventional microfabrication techniques. Each microelectrode was 15 μm wide and each detection unit was 30 × 30 μm^2 across. We found that as a worm moved closer to an addressed detection unit, the electrical resistance of this unit increased. The presence of part of the nematode's body at the selected detection unit caused a minimal electrical resistance change of ~8.1 % (vs. the simulated result of ~7.9 %), which was much higher than the manufacturing induced initial resistance variation of 3.3 % between all detection units. We designed an electronic circuit to address individual detection units and reading out their electrical resistance at the full-frame scanning frequency of 174 Hz. The circuit allowed tracking the time-varying shape and position of the worms and analysed the locomotive parameters of the nematode (e.g., oscillation frequency and moving speed) with the help of the worm tracking program. We also found that the shape and position of the nematodes could be identified when the full-frame scanning frequency of the electronic circuit increased to be more than 80 times the nematode's oscillation frequency. Furthermore, as the size of the detection unit increased, the spatial resolution of the reconstructed images decreased. In addition, we verified that no electrotaxic effect occurred at the worms since the electric field strength applied was set to be as low as ~1.5 V cm^{-1}. Lastly, the workability of the device was demonstrated by performing a drug resistance screening experiment on the MEF device. The device was able to differentiate the

locomotion behaviours of the wild-type N2 and mutant *lev-8 C. elegans* in response to a wide dose range of levamisole. We believe that the present MEF device can give potential to provide a cost-effective, potentially high throughput solution to tracking the behavioural phenotype changes of important nematodes for different bioassays on a chip level and large scale analysis.

3.6 Acknowledgements

This work is supported by the National Science Foundation under award no. ECCS-1102354, the McGee-Wagner Research Fund, the NIH grant: R56 AI047194–11 National Institute of Allergy and Infectious Diseases, and the China Scholarship Council. The content is solely the responsibility of the authors and does not necessarily represent the official views of the National Institute of Allergy and Infectious Diseases. The authors thank all members in the Laboratory for the NEMS and Lab-Chips for helpful discussion.

3.7 References

1 L. Guarente and C. Kenyon, *Nature*, 2000, **408**, 255–262.

2 T. Kaletta and M. O. Hengartner, *Nat. Rev. Drug Discovery*, 2006, **5**, 387–398.

3 G. Tsechpenakis, L. Bianchi, D.N. Metaxas and M. Driscoll, *IEEE Trans. Biomed. Eng.*, 2008, **55**, 1539–1549.

4 R. Sznitman, M. Gupta, G. D. Hager, P.E. Arratia and J. Sznitman, *PLoS ONE*, 2010, **5**, e11631.

5 W. Wang, Y. Sun, S. J. Dixon, M. Alexander and P. J. Roy, *J. Lab. Autom.*, 2009, **14**, 269–276.

6 D. Ramot, B. E. Johnson, T. L. Berry Jr, L. Carnell and M. B. Goodman, *PLoS ONE*, 2008, **3**, e2208.

7 C. J. Cronin, Z. Feng and W. R. Schafer, *Methods Mol. Biol.*, 2006, **351**, 241–251.

8 B. Potsaid, F. P. Finger and J. T. Wen, *IEEE Trans. Autom. Sci. Eng.*, 2009, 6, 525–535.

9 C. J. Cronin, J. E. Mendel, S. Mukhtar, Y. M. Kim, R. C. Stirbl, J. Bruck and P. W. Sternberg, *BMC Genet.*, 2005, **6**, 5.

10 S. H. Simonetta and D. A. Golombek, *J. Neurosci. Methods*, 2007, **161**, 273–280.

11 W. Geng, P. Cosman, C. C. Berry, Z. Feng and W. R. Schafer, *IEEE Trans. Biomed. Eng.*, 2004, **51**, 1811–1820.

12 J. Wu, G. Zheng and L. M. Lee, *Lab Chip*, 2012, **12**, 3566–3575.

13 G. M. Whitesides, *Nature*, 2006, **442**, 368–373.

14 A. J. deMello, *Nature*, 2006, **442**, 394–402.

15 D. Psaltis, S. R. Quake and C. H. Yang, *Nature*, 2006, **442**, 381–386.

16 M. M. Crane, K. Chung, J. Stirman and H. Lu, *Lab Chip*, 2010, **10**, 1509–1517.

17 K. H. Chung, M. M. Crane and H. Lu, *Nat. Methods*, 2008, **5**, 637–643.

18 N. Chronis, *Lab Chip*, 2010, **10**, 432–437.

19 N. Kim, C. M. Dempsey, J. V. Zoval, J.-Y. Sze and M. J. Madou, *Sens. Actuators, B*, 2007, **122**, 511.

20 S. R. Lockery, K. J. Lawton, J. C. Doll, S. Faumont, S. M. Coulthard, T. R. Thiele, N. Chronis, K. E. McCormick, M. B. Goodman and B. L. Pruitt, J. *Neurophysiol.*, 2008, **99**, 3136–3143.

21 P. Rezai, A. Siddiqui, P. R. Selvaganapathy and B. P. Gupta, *Lab Chip*, 2010, **10**, 220–226.

22 P. Rezai, S. Salam, P. R. Selvaganapathy, and B. P. Gupta, Lab Chip, 2012, 12, 1831–1840.

23 W. W. Shi, J. Qin , N. Ye and B. Lin, Lab Chip, 2008, 8, 1432–1435.

24 J. Clausell-Tormos, D. Lieber, J.-C. Baret, A. El-Harrak, O. J. Miller, L. Frenz, J. Blouwolff, K. J. Humphry, S. Koster, H. Duan, C. Holtze, D. A. Weitz, A. D. Griffiths and C. A. Merten, *Chem. Biol.*, 2008, 15, 427–437.

25 S. E. Hulme, S. S. Shevkoplyas, A. P. McGuigan, J. Apfeld, W. Fontana and G. M. Whitesides, *Lab Chip*, 2010, **10**, 589–597.

26 C. B. Rohde, F. Zeng, R. Gonzalez-Rubio, M. Angel and M. F. Yanik, *Proc. Natl. Acad. Sci. U. S. A.*, 2007, **104**, 13891–13895.

27 S. E. Hulme, S. S. Shevkoplyas, J. Apfeld, W. Fontana and G. M. Whitesides, *Lab Chip*, 2007, **7**, 1515–1523.

28 T. V. Chokshi, A. Ben-Yakar and N. Chronis, *Lab Chip*, 2009, **9**, 151–157.

29 F. Zeng, C. B. Rohde and M. F. Yanik, *Lab Chip*, 2008, **8**, 653–656.

30 K. Chung and H. Lu, *Lab Chip*, 2009, **9**, 2764–2766.

31 M. F. Yanik, H. Cinar, H. N. Cinar, A. D. Chisholm, Y. Jin and A. Ben-Yakar, *Nature*, 2004, **432**, 822.

32 S. X. Guo, F. Bourgeois, T. Chokshi, N. J. Durr, M. A. Hilliard, N. Chronis and A. Ben-Yakar, *Nat. Methods*, 2008, **5**, 531–533.

33 N. Chronis, M. Zimmer and C. I. Bargmann, *Nat. Methods*, 2007, **4**, 727–731.

34 S. H. Chalasani, N. Chronis, M. Tsunozaki, J. M. Gray, D. Ramot, M. B. Goodman and C. I. Bargmann, *Nature*, 2007, **450**, 63–70.

35 Y. Zhang, H. Lu and C. I. Bargmann, *Nature*, 2005, **438**, 179–184.

36 J. M. Gray, D. S. Karow, H. Lu, A. J. Chang, J. S. Chang, R. E. Ellis, M. A. Marletta and C. I. Bargmann, *Nature*, 2004, **430**, 317–322.

37 J. C. Doll, N. Harjee, N. Klejwa, R. Kwon, S. M. Coulthard, B. Petzold, M. B. Goodman and B. L. Pruitt, *Lab Chip*, 2009, **9**, 1449–1454.

38 J. H. Qin and A. R. Wheeler, *Lab Chip*, 2007, **7**, 186–192.

39 K. Chung, M. Zhan, J. Srinivasan, P. W. Sternberg, E. Gong, F. C. Schroeder and H. Lu, *Lab Chip*, 2011, **11**, 3689–3697.

40 S. R. Lockery , S. E. Hulme , W. M. Roberts , K. J. Robinson , A. Laromaine , T. H. Lindsay , G. M. Whitesides and J. C. Weeks, *Lab Chip*, 2012,**12**, 2211–2220.

41 P. Liu, D. Mao, R. J. Martin and L. Dong, *Lab Chip*, 2012, **12**, 3458–2466.

42 X. Heng, D. Erickson, L. R. Baugh, Z. Yaqoob, P. W. Sternberg, D. Psaltis and C. Yang, *Lab Chip*, 2006, **6**, 1274–1276.

43 X. Cui, L. M. Lee, X. Heng, W. Zhong, P. W. Sternberg, D. Psaltis and C. Yang, *Proc. Natl. Acad. Sci. U. S. A.*, 2008, **105**, 10670–10675.

44 L. M. Lee, X. Cui and C. Yang, *Biomed. Microdevices*, 2009, **11**, 951–958.

45 G. Zheng, S. A. Lee, S. Yang and C. Yang, *Lab Chip*, 2010, **10**, 3125–3129.

46 E. Schonbrun, A. R. Abate, P. E. Steinvurzel, D. A. Weitz and K. B. Crozier, *Lab Chip*, 2010, **10**, 852–856.

47 X. Heng, F. Hsiung, A. Sadri and P. Patt, *Anal. Chem.*, 2011, **83**, 1587–1593.

48 J. Wu, X. Cui, L. M. Lee and C. Yang, *Opt. Express*, 2008, **16**, 15595–15602.

49 A. F. Coskun, T.-W. Su and A. Ozcan, *Lab Chip*, 2010, **10**, 824–827.

50 O. Mudanyali, D. Tseng, C. Oh, S. O. Isikman, I. Sencan, W. Bishara, C. Oztoprak, S. Seo, B. Khademhosseini and A. Ozcan, *Lab Chip*, 2010, **10**, 1417–1428.

51 S. O. Isikman, W. Bishara, S. Mavandadi, S. W. Yu, S. Feng, R. Lau and A. Ozcan, *Proc. Natl. Acad. Sci. U. S. A.*, 2011, **108**, 7296–7301.

52 S. O. Isikman, W. Bishara, U. Sikora, O. Yaglidere, J. Yeah and A. Ozcan, *Lab Chip*, 2011, **11**, 2222–2230.

53 T.-W. Su, S. O. Isikman, W. Bishara, D. Tseng, A. Erlinger and A. Ozcan, *Optics Express*, 2010, **18**, 9690–9711.

54 C. Oh, S. O. Isikman, B. Khadem, and A. Ozcan, *Optics Express*, 2010, **18**, 4717–4726.

55 S. O. Isikman, I. Sencan, O. Mudanyali, W. Bishara, C. Oztoprak and A. Ozcan, *Lab Chip*, 2010, **10**, 1109–1112.

56 A. F. Coskun, T.-W. Su and A. Ozcan, *Lab Chip*, 2010, **10**, 824–827.

57 A. Ozcan and U. Demirci, *Lab Chip*, 2008, **8**, 98–106.

58 J. A. Carr, A. Parashar, R. Gibson, A. P. Robertson, R. J. Martin and S. Pandey, *Lab Chip*, 2011, **11**, 2385–2396.

59 S. Shaham, ed., WormBook: Methods in Cell Biology (Jan. 02, 2006), *WormBook*, ed. The *C. elegans* Research Community, WormBook, doi/10.1895/wormbook.1.49.1, http://www.wormbook.org.

CHAPTER 4

TUNABLE META-ATOM USING LIQUID METAL EMBEDDED IN STRETCHABLE POLYMER

A paper published in Journal of Applied Physics

Peng Liu, Siming Yang, Aditya Jain, Qiugu Wang, Huawei Jiang, Jiming Song, Thomas Koschny, Costas M. Soukoulis, and Liang Dong

4.1 Abstract

Reconfigurable metamaterials have great potential to alleviate complications involved in using passive metamaterials to realize emerging electromagnetic (EM) functions, such as dynamical filtering, sensing, and cloaking. This paper presents a new type of tunable meta-atoms in the X-band frequency range (8-12 GHz) toward reconfigurable metamaterials. The meta-atom is made of all flexible materials compliant to the surface of an interaction object. It uses a liquid metal-based split-ring resonator (SRR) as its core constituent embedded in a highly flexible elastomer. We demonstrate that simple mechanical stretching of the meta-atom can lead to the great flexibility in reconfiguring its resonance frequency continuously over more than 70% of the X-band frequency range. The presented meta-atom technique provides a simple approach to dynamically tune response characteristics of metamaterials over a broad frequency range.

4.2 Introduction

Flexible electronics have gained considerable attention because of their potential applications in artificial skins, flexible displays, wearable sensors, sustainable energy, etc. Many flexible electronic devices have recently been developed, such as stretchable integrated circuits,[1-5] microfluidic antennas,[6-8] three-dimensional energy devices,[9] printed thin film

transistors,[10-13] and biomimetic pressure sensors.[14] On the other hand, EM metamaterials have been intensively studied because they possess intriguing properties unattainable with naturally existing materials, such as negative permittivity and permeability.[15-27] SRR is a popular building block of many metamaterial-based resonant devices in the microwave regime.[28-31] But, these resonant devices often have a limited bandwidth. If the response characteristics are dynamically tunable, these resonant devices will become more useful when adapting to different applications. To this end, many tunable metamaterial technologies have been demonstrated, based on changing unit cell's effective circuit parameters,[32-36] constituent material properties,[37-42] or geometries.[43-49] Specifically, the circuit tuning method uses variable capacitors and switches to change individual impedances of unit cells.[32-36] Tuning of the constituent materials relies on using phase change materials or liquid crystal to change properties of materials that make up unit cells.[37-42] The micro-electro-mechanical systems and microfluidics based approaches change structures and locations of unit cells relative to a fixed part of metamaterials.[43-49]

While the existing tunable metamaterial technologies have led to significant improvement toward broadening dynamic tuning ranges of the EM properties of microwave metamaterials, there is still much room for improvement, such as simplifying resonance tuning mechanism, extending tuning range, and making metamaterials flexible enough to comply with surface irregularities on the underlying substrate. For example, a switchable metamaterial has recently been developed, capable of tuning its resonance frequency by pumping mercury into and out of SRR-shaped microchannels via a relatively complex microfluidic control system.[41] A tunable liquid metal-based antenna has also been realized by injecting a liquid metal alloy into a microchannel made of a stretchable elastomer.[6] This

device could be stretched to more than double of its original length, thus obtaining a wide frequency tuning range.

In this paper we present a novel stretchable SRR-based meta-atom capable of tuning its EM response characteristics over a broad frequency range via simple mechanical stretching. The presented meta-atom uses a liquid metal as the resonator material. The liquid metal is patterned to be a SRR structure and embedded inside a highly stretchable silicone elastomer. Due to its liquid nature, the SRR can flow in response to applied strains, and thus, is not prone to fatigue or cracking. When the encasing elastomer is stretched and twisted, the SRR will be sufficiently compliant to yield all necessary deformation. Therefore, by changing the shape of the SRR via mechanical stretching, the split gap capacitance and the inductance of the SRR can be adjusted, thus tuning the resonance response of the meta-atom.

4.3 Design and Fabrication

To test the concept of mechanically tunable meta-atom, we designed a liquid metal SRR to operate in the X-band frequency range (Fig. 4.1). While many types of liquid metal may be used, the SRR in this study employed eutectic gallium-indium or EGaIn (75.5% gallium and 24.5% indium; a liquid at room temperature and a solid at 14 ^{o}C) because of its favorable attributes, such as high electrical conductivity, low toxicity, and light weight. The liquid metal SRR had the inner radius of a = 1.5 mm, the outer radius of b = 2.0 mm, the thickness of h = 0.5 mm, and the gap distance of g = 1.0 mm. The SRR was encased by Ecoflex, a highly stretchable silicone elastomer with the maximal elongation at break of 900%. It's noteworthy that Ecoflex is thermally curable and suitable for replica molding from a master mold, just like polydimethylsiloxane, a commonly used elastomer used in soft

lithography. The length, width, and thickness of the Ecoflex encasing membrane were l = 11.0 mm, d = 7.5 mm, and t = 1.45 mm, respectively.

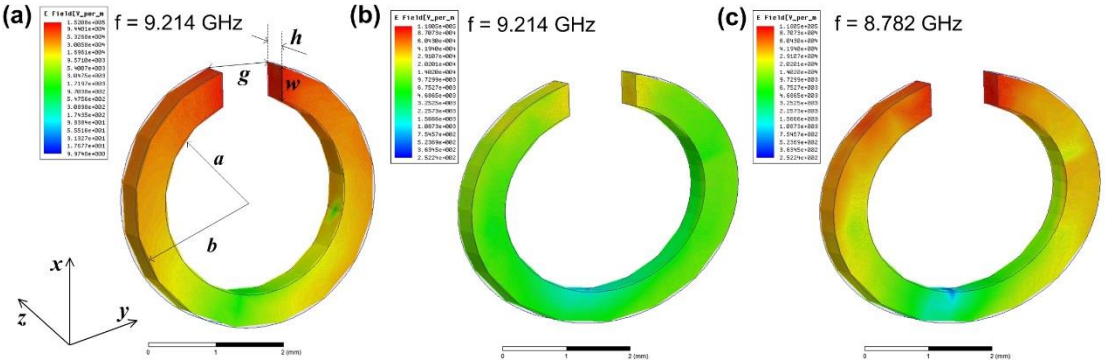

Fig. 4.1. Simulated magnitude of the electric field (E) distributions in the tunable liquid metal SRR at the resonance frequency of 9.214 GHz when not stretched (a), at 9.214 GHz when stretched by 30% along the *y* direction (b), and at a new resonance frequency of 8.782 GHz at the stretched state (c) .

The resonant response of a SRR can be equivalently regarded as a LC resonator with a resonance frequency of $f_o = 1/(2\pi\sqrt{LC})$, where the inductance L results from the current path of the SRR, and the capacitance C is determined by the split gap and the dielectric properties of the substrate along with the material that fills the gap. In this study, when the SRR was stretched, both of the capacitance and inductance would change, thus shifting the resonance frequency. To illustrate the influence of mechanical stretching on the resonance of the SRR, we conducted EM simulations using the Ansys High Frequency Structure Simulator (HFSS) software. As shown in Fig. 4.1, the SRR was fixed in the *x*-*y* plane inside a waveguide and the magnetic field (H) was parallel to the *z* direction and penetrated through the SRR, thus exciting the magnetic resonance. When the split gap of the SRR was aligned along the *y* direction, the resonance frequency before stretch was at 9.214 GHz (Fig. 4.1a). Applying the stretch of 30% along the *y* direction led to an increase in the split gap along the same direction (Fig. 4.1b). As a result, the SRR was brought out of resonance at 9.214 GHz and resonated at a new frequency of 8.782 GHz (Fig. 4.1c). We note that the simulation here

only conceptually illustrated the proposed tuning mechanism. The more quantitative simulation results are presented and discussed later, together with the experimental results.

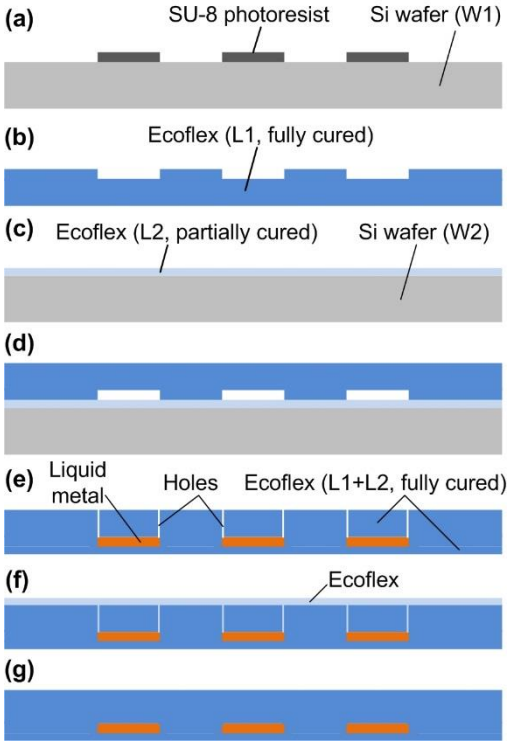

Fig. 4.2. Fabrication process for the tunable liquid metal SRR.

Fig.4.2 shows the fabrication process flow for the tunable meta-atom. First, to form the SRR-shaped microchannels, an 800-µm-thick Ecoflex layer L1 was cast upon a master mold made of SU-8 photoresist on a silicon (Si) wafer W1, and then, was fully cured at 60 ^{o}C on a hotplate for 30 mins (Fig. 4.2a,b). In a parallel process, a 100-µm-thick Ecoflex thin layer L2 was spin-coated on another Si wafer W2, followed by partial curing at 50 ^{o}C on a hotplate for 40 s (Fig. 4.2c). Subsequently, the layer L1 was peeled off from the master mold and adhered to the partially cured layer L2. The two layers L1 and L2 were then permanently and thermally bonded together on a hotplate at 90 ^{o}C for 30 mins (Fig. 4.2d). After the two bonded layers were peeled off from the wafer W2, the liquid metal EGaIn was injected into the embedded microchannels through two 100-µm-diameter holes mechanically punched at

the two ends of each microchannel. There were some residues of the eutectic alloy remaining around the holes on the top surface of the Ecoflex structure. To clean the top surface, a cotton swab was dipped in a solution of hydrochloric acid (50%, v/v) and then carefully wiped off any residues from the top surface (Fig. 4.2e). To encapsulate the liquid metal inside the Ecoflex elastomer, a new Ecoflex prepolymer solution was poured onto the cleaned top surface, followed by a full curing process performed at 80 ^{o}C on a hotplate for 30 mins (Fig. 4.2f,g). Therefore, the liquid metal SRRs were formed inside the elastomer. The total thickness of the elastomer was 1.45 mm as mentioned. The SRRs were located nearly at half the thickness of the elastomer. Lastly, individual SRRs were diced out of the whole elastomer for testing.

4.4 EM Measurement Configurations

After the meta-atom was formed, we carried out the EM measurements over the X-band using a WR90 rectangular waveguide (22.86 × 10.16 mm) terminated by a UG39/U cover flange. When the waves propagated in the waveguide, the directions of E and H were along the short edge and the long edge of the waveguide, respectively. The walls of the waveguide acted as reflective mirrors and made the SRR cell behave as an element in a 2D quasi-periodic structure with normal incidence wave. The SRR sample was attached onto a wood slab (low-loss microwave substrate material) and centered in the middle of the waveguide. Multiple cotton wires were inserted through the holes prepunched at the opposite ends of the Exoflex elastomer. The elastomer was then stretched to a specified strain level (17%, 28%, 53%, or 72%). To hold the sample in place, the cotton wires passed through the holes predrilled in the wood slab and then rolled and tied on the wood posts at the backside of the slab. The spectra were measured using a programmable vector network analyzer

(Agilent E8364). A full 2-port calibration was performed to set an accurate reference plane before the measurement.

There were six possible arrangements for the SRR inside the waveguide, as illustrated in Fig. 4.3. But only three of them (Fig. 4.3a,c,d) were able to excite the resonance of the circular ring current in the SRR (magnetic dipole resonance). Fig. 4.3a displays that the incident wave was normal to the plane of the ring and the E field was parallel to the gap direction. The electric dipole formed across the split gap allowed coupling of the E field of the waveguide mode to the magnetic dipole resonance of the SRR because of the broken symmetry of the ring with respect to the E-field direction. In the case shown in Fig. 4.3c, both the electric moment across the gap driven by the incident E field and the magnetic moment of the circular ring induced by the incident H field current jointly excite the resonance of the ring. Fig. 4.3d shows that the H field is normal to the plane of the ring, which induces the circulating current in the ring and generate magnetic moment. Neither electric nor magnetic dipole moment could couple to the incident waveguide mode in the other three configurations shown in Fig. 4.3b,e,f.

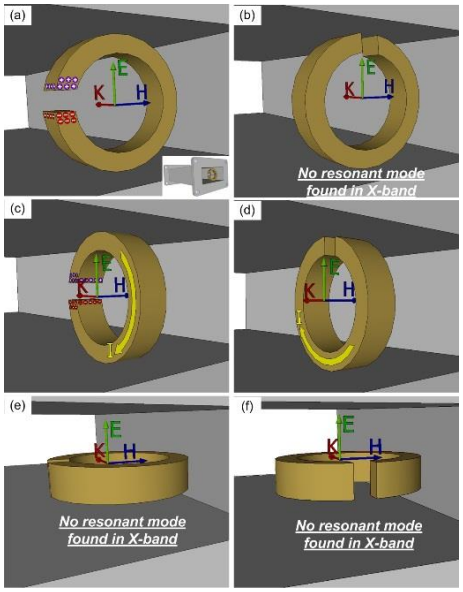

Fig. 4.3. Six possible configurations of the SRR inside a testing waveguide. The inset in (a) shows the relative location of the ring to the waveguide. The electric dipole formed by opposite electric charges accumulating across the gap of the ring couples the SRR resonance to the E field of the incident waveguide mode in (a) and (c). The magnetic dipole moment due to the loop current couples to the incident H field normal to the ring plane in (c) and (d). No coupling to the resonance was found in (b), (e), and (f) in X-band.

4.5 Results and Discussion

In the first measurement configuration (Fig. 4.3a), the SRR was stretched along the H-field direction with different stretch ratios. The E field was formed across the split gap to excite the electric resonance that corresponded to a transmission dip at the resonance frequency in the transmittance spectrum (see *Appendix* Fig. S1 for the reflectance spectrum). The experimental result in Fig. 4.4a shows that by stretching the SRR, the resonance was progressively tuned to the lower frequencies. For the stretch ratio of 17%, 28%, 53%, and 72%, the resonance frequency red shifted from 10.54 GHz to 9.78 GHz, 9.05 GHz, 8.52 GHz, and 7.67 GHz, respectively. The deformation of the SRR under different stretch levels was observed consistent with the simulated deformation using the finite element method analysis (FEA) with the COMSOL Multiphysics (Fig. 4.4b). The embedded liquid metal was also

found to remain continuous while being compliant to the changing shape of the surrounding elastomer.

We modeled the SRR and conducted simulations for its resonance response to different stretching magnitudes using the full-wave 3D EM simulation tool in the CST Studio. The structural parameters of the deformed SRR were extracted from the images of the SRR. In this simulation, the SRR was placed in a rectangular waveguide with four metal walls, the same as the experimental measurement setup. The simulated transmittance spectra of the SRR were presented with dashed lines along with the experimental result in Fig. 4.4a.

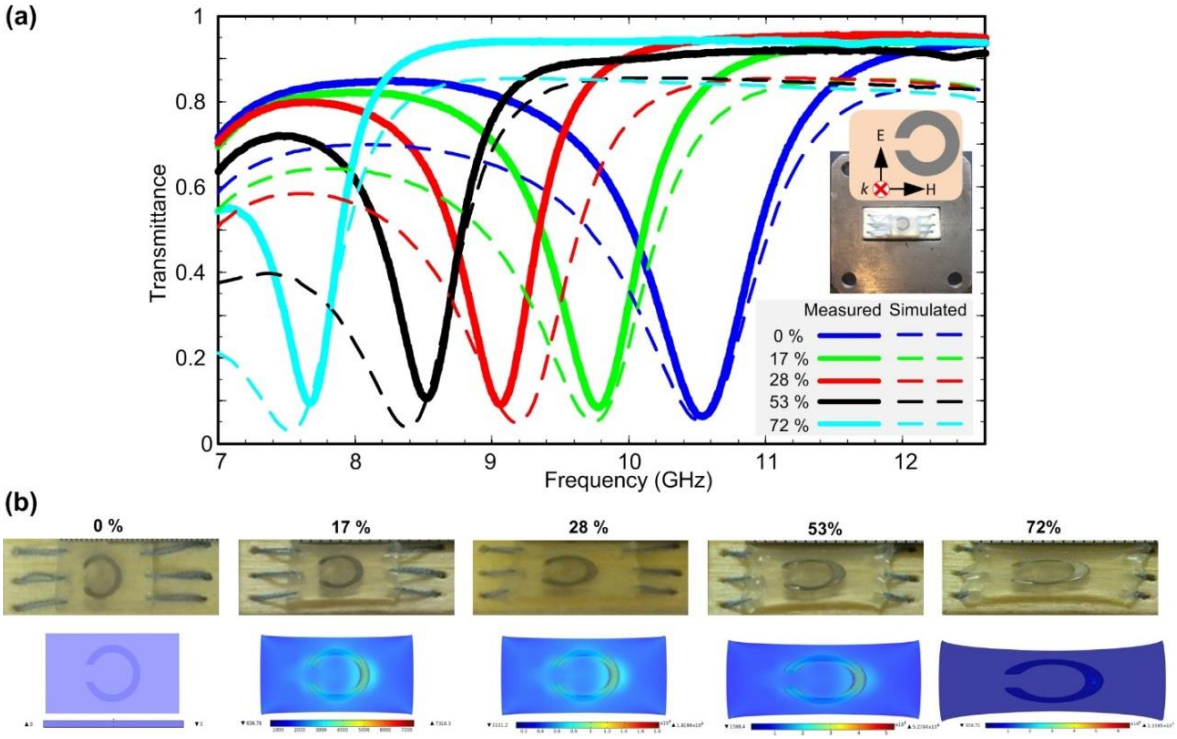

Fig. 4.4. (a) Measured and simulated transmittance spectra of the tunable liquid metal SRR meta-atom at different stretching ratios of 0, 17%, 28%, 53%, and 72%, when the meta-atom was placed inside the waveguide as shown in the inset. Also, refer to Fig. 4.3a for the measurement arrangement. The conductivity of liquid metal was 3.46×10^6 S/m. The dielectric constant and loss tangent of Ecoflex silicone rubber was 2.5 and 0.01, respectively. The SRR was placed on a wood substrate with the dielectric constant of 1.22 and the loss tangent of 0.1. (b) Experimental (left) and corresponding simulated (right) results for the stretch-induced mechanical deformations of the tunable meta-atom.

In the second measurement configuration (Fig. 4.3c), the resonance was excited by both of the E and H fields. At the stretch level of 17%, 28%, 53%, and 72%, the resonance frequency was observed to red shift from 10.21 GHz to 9.58 GHz, 9.37 GHz, 8.58 GHz, and 7.37 GHz, respectively (Fig. 4.5a). In the third measurement configuration (Fig. 4.3d), the resonance was induced by the circulating current in the ring caused by the H field. The measurement result shows that at the stretch level of 17%, 28%, 53%, and 72%, the resonance frequency also red shifted from 9.58 GHz to 9.24 GHz, 8.79 GHz, 8.32 GHz, and 7.32 GHz, respectively (Fig. 4.6a). Similarly, Fig. 4.5b and 4.6b shows the experimental and simulated geometric changes of the SRR at different stretching levels in the second and third configurations, respectively (see *Appendix* Fig. S2 and S3 for the reflectance spectrum of the second and the third measurement configurations, respectively).

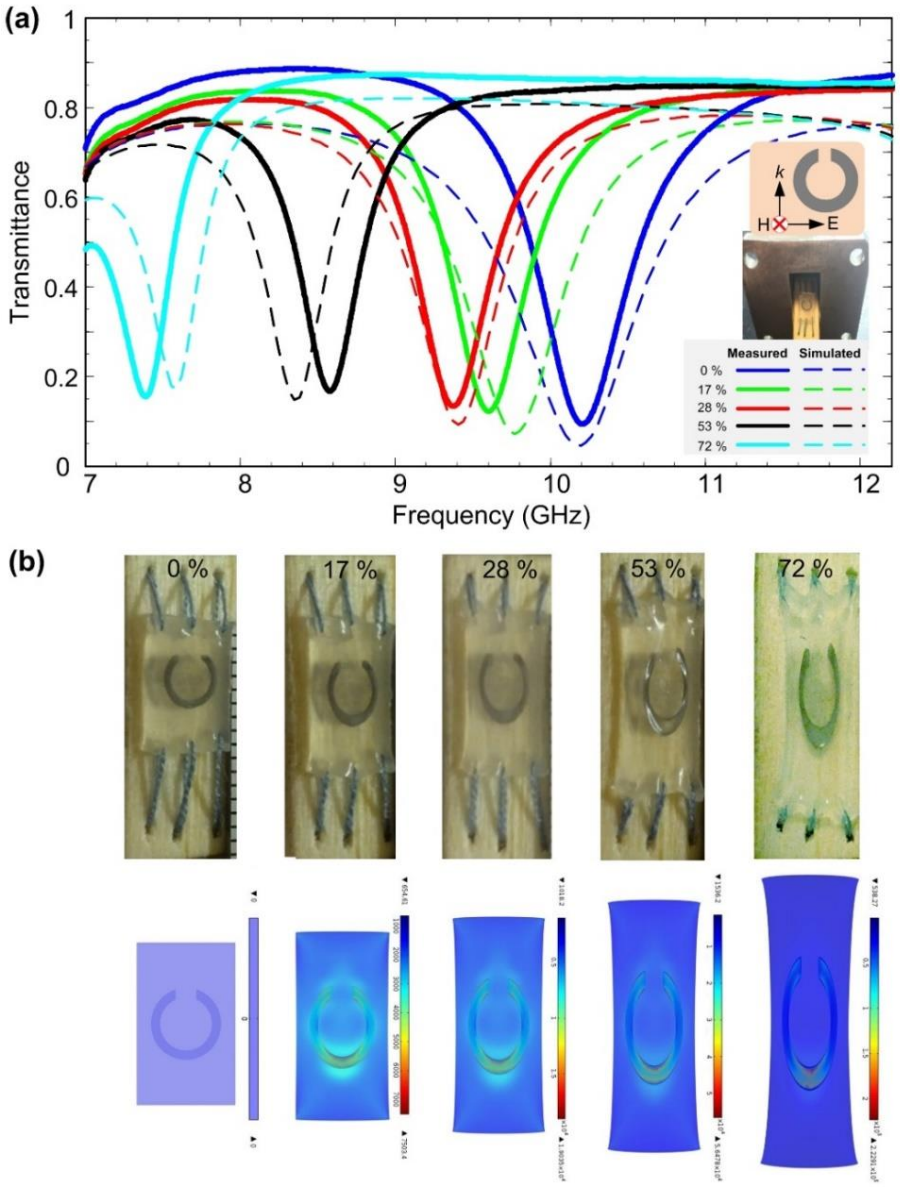

Fig. 4.5. (a) Measured and simulated transmittance spectra of the tunable liquid metal SRR meta-atom at different stretching ratios of 0, 17%, 28%, 53%, and 72%, when the meta-atom was placed inside the waveguide as shown in the inset. Also, refer to Fig. 4.3c for the measurement arrangement. (b) Experimental (upper) and corresponding simulated (lower panel) results for the stretch-induced mechanical deformations of the tunable meta-atom.

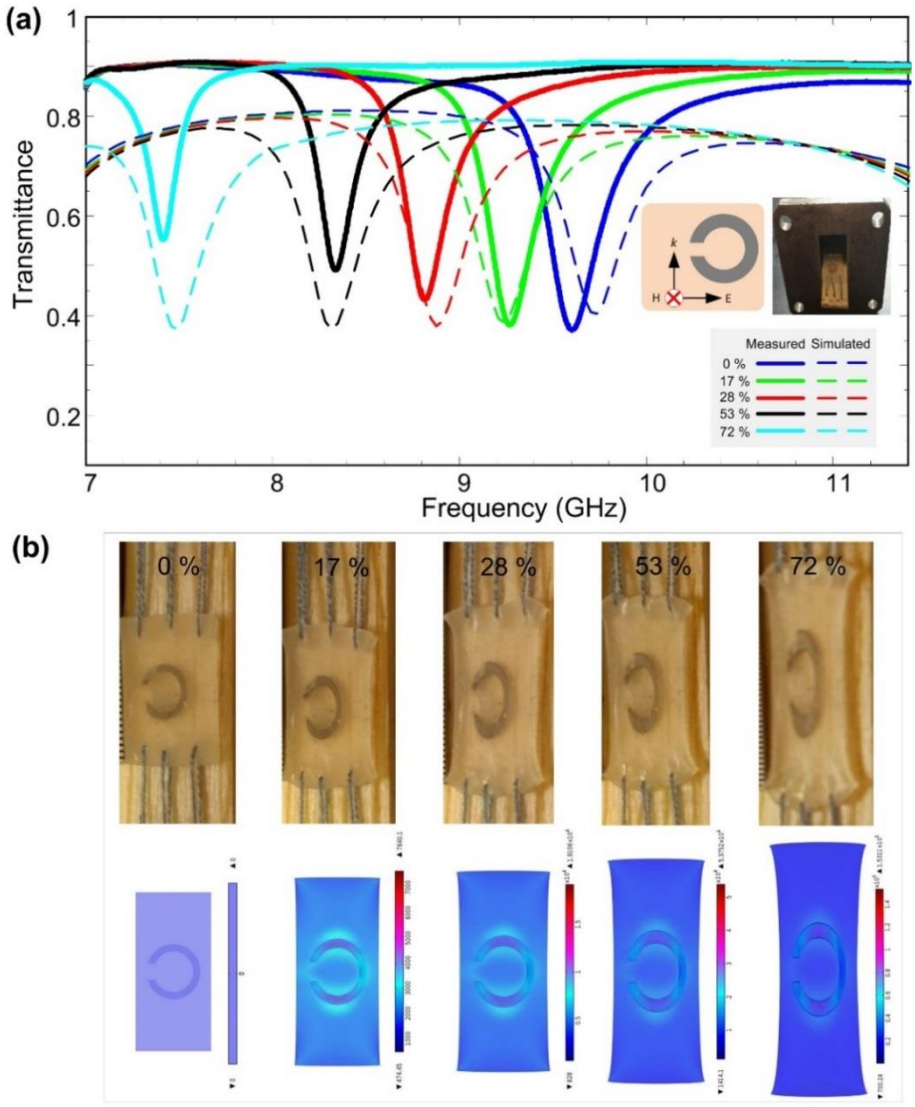

Fig. 4.6. (a) Measured and simulated transmittance spectra of the tunable liquid metal SRR meta-atom at different stretching ratios of 0, 17%, 28%, 53%, and 72%, when the meta-atom was placed inside the waveguide as shown in the inset. Also, refer to Fig. 4.3d for the measurement arrangement. (b) Experimental (upper) and corresponding simulated (lower panel) results for the stretch-induced mechanical deformations of the tunable meta-atom.

For all three of the aforementioned configurations, the experimental EM measurement results show good agreement with the simulated results. The slight discrepancy between the simulated and testing results is presumably attributed to the limited accuracy of the EM modeling. Here, the modeling accuracy mainly depends on the geometric parameters extracted from the images of the deformed SRRs and Ecoflex elastomer (Fig. 4.4b, 4.5b, and

4.6b), and the material parameters (e.g., dielectric constant and tangent loss of the wood slab and Ecoflex) used in the simulation. Also, the convergent criterion for the simulation affects the results. To achieve a balance between accuracy and efficiency, we set the convergent criterion to 0.01. As demonstrated, when the same stretch of 72% was applied to the SRR in all the three measurement configurations, the resonance frequency of the SRR were tuned by a net shift of 2.87 GHz (Fig. 4.4a), 2.83 GHz (Fig. 4.5a), and 2.26 GHz (Fig. 4.6a), or a relative shift of 27.2%, 27.8%, and 23.5%, with respect to the original resonance frequency of 10.54 GHz, 10.20 GHz, and 9.58 GHz, respectively. Fig. 4.7 summarizes the relationships between the stretch ratio and the resulting resonance frequency shift.

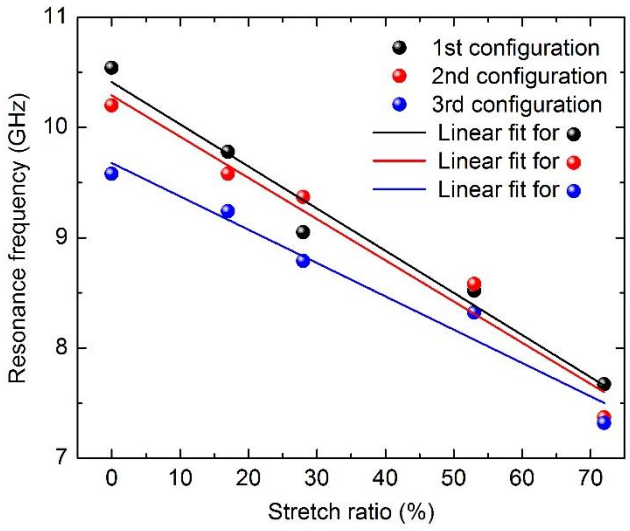

Fig. 4.7. Resonance frequency as a function of the stretch ratio for the tunable meta-atom in the three measurement configurations shown in Fig. 4.4-4.6.

Although the obtained experimental and CST-based simulation results have demonstrated the ability to tune the resonance frequency of the SRR via mechanical stretching, it is worthwhile to further understand how the equivalent capacitance and inductance of the SRR were influenced by their geometric deformation. The equivalent capacitance is dominated by the split gap capacitance C_{gap} which is a function of the gap

geometry (see Equation A.1 in the *Appendix* for the closed-form equation). The equivalent inductance consists of self-inductance of the conducting loop and the mutual inductance induced by the boundary conditions of a given waveguide that are imposed on the SRR for certain orientations (quasi-periodic structure). The self-inductance of an unstretched circular loop L_0 and a stretched elliptical loop L_e are geometrically dependent (see Equation A.2 and A.3 in *Appendix* for the closed-form equation). The mutual inductance depends on not only the self-inductance but the SRR orientations with different mirror effects imposed by the waveguide. We note that in the previous experiments the resonance modes of the SRR were excited inside a waveguide where mutual interactions with the inner walls of the waveguide existed. But, to simplify the simulation while still illustrating a changing trend of resonance frequency shift, the effect of the mutual interaction into the free-space simulation was excluded, because compared with the effect from the mutual interaction with the walls, the geometric deformation of the SRR could be considered to contribute most to the resonance frequency change. Therefore, we performed EM simulations for a single SRR using HFSS in the free space. Specifically, a delta-gap source was set along the gap direction to excite the unit cell (Fig. 4.8a) and the impedance was monitored while sweeping the frequency. To describe the resonance behavior of the stretching SRR, we designed a one-port equivalent circuit taking into account the equivalent inductance L and capacitance C, the dielectric loss R_d from the substrate, and the metallic loss R_m from the liquid metal (Fig. 4.8b). The lumped L and C were obtained by optimizing the impedance of the equivalent circuit based on the simulated impedance around the resonant frequency with less than 3% of relative error for each stretching case.

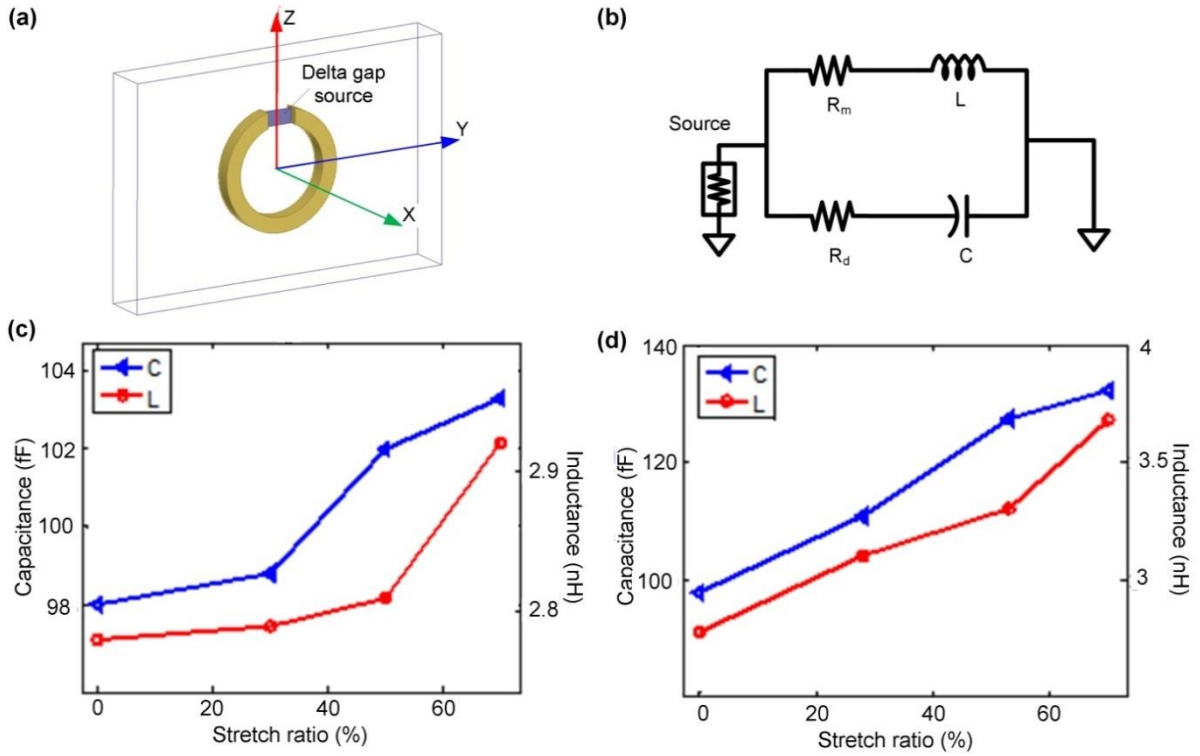

Fig. 4.8. (a) Schematic of the tunable SRR in the free space. A delta-gap source was set along the split gap. (b) Equivalent circuit of the SRR shown in (a). (c) Simulated capacitance and inductance as a function of the stretch ratio when the SRR was stretched perpendicular to the split gap direction. (d) Simulated capacitance and inductance as a function of the stretch ratio when the SRR was stretched along the gap direction.

The simulation results (Fig. 4.8c,d) show that as the unit cell was stretched perpendicular to (the first and the second configurations in Fig. 4.4, 4.5) or along (the third configuration in Fig. 4.6) the gap direction, the equivalent capacitance and inductance increased with increasing the stretch ratio. Since the mechanical stretching in any one of the configurations increased the perimeter of the SRR loop, it is obvious that the inductance would increase with stretching. As for the capacitance, in the first and the second configurations, the stretching caused to decrease the distance between the two arms of the SRR, and also caused to increase the effective metal area that allowed holding more charges. Therefore, the equivalent capacitance of the SRR in these two configurations was increased as increasing the stretch ratio. In the third configuration, despite that the distance between the

arms was increased, the stretching also increased the area of liquid metal in the arms region near the split. By further considering the fringing effect, the ability of the SRR to store charges was actually enhanced, thus increasing the equivalent capacitance as well. The simulation result also indicates that the perpendicular stretching (Fig. 4.8d) was more effective than the parallel stretching (Fig. 4.8c). This is because when the SRR was stretched in the perpendicular direction, the gap distance rapidly decreased to make the delta-gap source more effective.

The present meta-atom exhibited good repeatability in the resonance modulation, as demonstrated with 500 stretching response tests. During each test, the meta-atom was stretched to a same strain level outside the waveguide and then placed back into the waveguide for EM measurement. We note that further elongation of the SRR beyond 72% would move the resonance frequency to below the cutoff frequency of the waveguide used in this study. Nevertheless, even with the applied moderate stretch amplitude, this tunable meta-atom method provided a considerable frequency tuning range covering 71.75% (2.87 GHz divided by 4.0 GHz) of the whole X-band frequency range (8.0 – 12.0 GHz). Furthermore, by changing its overall size and geometric parameters of the SRR, the original resonance frequency of the SRR can be set to be at the upper limit of the X-band frequency range. By doing that, tuning in the whole X-band frequency range may be achieved with sufficient stretching. Our experiments showed that the present SRR could be stretched by more than twice (> 200%) the original size in any directions, while keeping the embedded liquid metal structure continuous, flexible, and recoverable, without breaking of the encasing polymer layer or occurring of structural hysteresis.

4.6 Conclusion

A liquid metal SRR-based tunable meta-atom was demonstrated in the X-band frequency range. The meta-atom consisted of a liquid metal resonator encased by a flexible elastomer skin. By stretching the meta-atom, the resonance frequency of the meta-atom was tuned continuously over more than 70% of the whole X-band frequency range. The meta-atom in this study presents a simple but effective building block for realizing mechanically tunable metamaterials. Also, since the constituent materials of the present meta-atom are relatively ecofriendly, reusable and durable, the metamaterials made of such meta-atoms potentially will find many applications in wearable EM coatings and devices.

4.7 Acknowledgements

The work was partially supported by the National Science Foundation under the grant ECCS-0954765, the Iowa Department of Transportation, the Iowa Highway Research Board, and the China Scholarship Council. The work at Ames Laboratory was partially supported by the US Department of Energy, Office of Basic Energy Science, Division of Materials Sciences and Engineering. Ames Laboratory is operated for the US Department of Energy by Iowa State University under Contract No. DE-AC02-07CH11358.

4.8 References

[1]D.-H. Kim, J.-H. Ahn, W. M. Choi, H.-S. Kim, T.-H. Kim, J. Song, Y. Y. Huang, Z. Liu, C. Lu, and J. A. Rogers, *Science* **320,** 507 (2008).

[2]D.-H. Kim, Z. Liu, Y.-S. Kim, J. Wu, J. Song, H.-S. Kim, Y. Huang, K.-c. Hwang, Y. Zhang, and J. A. Rogers, *Small* **5,** 2841 (2009).

[3]J.-H. Ahn, H.-S. Kim, K. J. Lee, S. Jeon, S. J. Kang, Y. Sun, R. G. Nuzzo, and J. A. Rogers, *Science* **314,** 1754 (2006).

[4]Y. Sun and J. A. Rogers, *Adv. Mater.* **19,** 1897 (2007).

[5]J. Yoon, S. Y. Hong, Y. Lim, S.-J. Lee, G. Zi, and J. S. Ha, *Adv. Mater.* **26,** 6580 (2014).

[6]M. Kubo, X. Li, C. Kim, M. Hashimoto, B. J. Wiley, D. Ham, and G. M. Whitesides, *Adv. Mater.* **22,** 2749 (2010).

[7]J.-H. So, J. Thelen, A. Qusba, G. J. Hayes, G. Lazzi, and M. D. Dickey, *Adv. Funct. Mater.* **19,** 3632 (2009).

[8]M. R. Khan, G. J. Hayes, J.-H. So, G. Lazzi, and M. D. Dickey, *Appl. Phys. Lett.* **99,** 013501 (2011).

[9]Y. Yang, G. Ruan, C. Xiang, G. Wang, and J. M. Tour, *J. Am. Chem. Soc.* **136,** 6187 (2014).

[10]A. C. Arias, S. E. Ready, R. Lujan, W. S. Wong, K. E. Paul, A. Salleo, M. L. Chabinyc, R. Apte, R. A. Street, Y. Wu, P. Liu, and B. Ong, *Appl. Phys. Lett.* **85,** 3304 (2004).

[11]K. Hong, S. H. Kim, K. H. Lee, and C. D. Frisbie, *Adv. Mater.* **25,** 3413 (2013).

[12]A. Pierre, M. Sadeghi, M. M. Payne, A. Facchetti, J. E. Anthony, and A. C. Arias, *Adv. Mater.* **26,** 5722 (2014).

[13]A. d. l. F. Vornbrock, D. Sung, H. Kang, R. Kitsomboonloha, and V. Subramanian, *Org. Electron.* **11,** 2037 (2010).

[14]W. Wu, X. Wen, and Z. L. Wang, *Science* **340,** 952 (2013).

[15]H.-T. Chen, J. F. O'Hara, A. K. Azad, A. J. Taylor, R. D. Averitt, D. B. Shrekenhamer, and W. J. Padilla, *Nature Photon.* **2,** 295 (2008).

[16]H.-T. Chen, W. J. Padilla, J. M. O. Zide, A. C. Gossard, A. J. Taylor, and R. D. Averitt, *Nature* **444,** 597 (2006).

[17]A. Jain, P. Tassin, T. Koschny, and C. M. Soukoulis, *Phys. Rev. Lett.* **112,** 117403 (2014).

[18]D. R. Smith, D. C. Vier, T. Koschny, and C. M. Soukoulis, *Phys. Rev. E* **71,** 036617 (2005).

[19]D. Schurig, J. J. Mock, B. J. Justice, S. A. Cummer, J. B. Pendry, A. F. Starr, and D. R. Smith, *Science* **314,** 977 (2006).

[20]D. Shin, Y. Urzhumov, Y. Jung, G. Kang, S. Baek, M. Choi, H. Park, K. Kim, and D. R. Smith, *Nat. Commun*. **3,** 1213 (2012).

[21]W. Cai, U. K. Chettiar, A. V. Kildishev, and V. M. Shalaev, *Nature Photon.* **1,** 224 (2007).

[22]J. Hao, J. Wang, X. Liu, W. J. Padilla, L. Zhou, and M. Qiu, *Appl. Phys. Lett.* **96,** 251104 (2010).

[23]N. I. Landy, S. Sajuyigbe, J. J. Mock, D. R. Smith, and W. J. Padilla, *Phys. Rev. Lett.* **100,** 207402 (2008).

[24]J. B. Pendry, D. Schurig, and D. R. Smith, *Science* **312,** 1780 (2006).

[25]I. M. Pryce, Y. A. Kelaita, K. Aydin, and H. A. Atwater, *Acs Nano* **5,** 8167 (2011).

[26]X. Zhang and Z. Liu, *Nature Mater*. **7,** 435 (2008).

[27]Q. Zhou, Y. Shi, A. Wang, L. Li, D. Zhao, J. Liu, H. Sun, and C. Zhang, *J. Opt.* **13,** 125102 (2011).

[28]R. A. Shelby, D. R. Smith, and S. Schultz, *Science* **292,** 77 (2001).

[29]D. R. Smith, W. J. Padilla, D. C. Vier, S. C. Nemat-Nasser, and S. Schultz, *Phys. Rev. Lett.* **84,** 4184 (2000).

[30]A. A. Zharov, I. V. Shadrivov, and Y. S. Kivshar, *Phys. Rev. Lett.* **91,** 37401 (2003).

[31]N. Katsarakis, T. Koschny, M. Kafesaki, E. N. Economou, and C. M. Soukoulis, *Appl. Phys. Lett.* **84,** 2943 (2004).

[32]K. Aydin and E. Ozbay, *J. Appl. Phys.* **101,** 024911 (2007).

[33]I. Gil, J. Bonache, J. Garcia-Garcia, and F. Martin, *IEEE Trans. Microw. Theory Techn.* **54,** 2665 (2006).

[34]D. Wang, L. Ran, H. Chen, M. Mu, J. A. Kong, and B.-I. Wu, *Appl. Phys. Lett.* **91,** 164101 (2007).

[35]J. Han, A. Lakhtakia, and C.-W. Qiu, *Opt. Express* **16,** 14390 (2008).

[36]G. He, R.-x. Wu, Y. Poo, and P. Chen, *J. Appl. Phys.* **107,** 093502 (2010).

[37]Y. Poo, R.-x. Wu, G.-h. He, P. Chen, J. Xu, and R.-f. Chen, *Appl. Phys. Lett.* **96,** 161902 (2010).

[38]R. Pratibha, K. Park, I. I. Smalyukh, and W. Park, *Opt. Express* **17,** 19459 (2009).

[39]D. H. Werner, D.-H. Kwon, and I.-C. Khoo, *Opt. Express* **15,** 3342 (2007).

[40]Q. Zhao, L. Kang, B. Du, B. Li, J. Zhou, H. Tang, X. Liang, and B. Zhang, *Appl. Phys. Lett.* **90,** 011112 (2007).

[41]T. S. Kasirga, Y. N. Ertas, and M. Bayindir, *Appl. Phys. Lett.* **95,** 214102 (2009).

[42]F. Zhang, Q. Zhao, L. Kang, D. P. Gaillot, X. Zhao, J. Zhou, and D. Lippens, *Appl. Phys. Lett.* **92,** 193104 (2008).

[43]Y. H. Fu, A. Q. Liu, W. M. Zhu, X. M. Zhang, D. P. Tsai, J. B. Zhang, T. Mei, J. F. Tao, H. C. Guo, X. H. Zhang, J. H. Teng, N. I. Zheludev, G. Q. Lo, and D. L. Kwong, *Adv. Funct. Mater.* **21,** 3589 (2011).

[44]M. Lapine, D. Powell, M. Gorkunov, I. Shadrivov, R. Marques, and Y. Kivshar, *Appl. Phys. Lett.* **95,** 084105 (2009).

[45]M. Lapine, I. V. Shadrivov, D. A. Powell, and Y. S. Kivshar, *Nature Mater*. **11,** 30 (2012).

[46]W. M. Zhu, A. Q. Liu, X. M. Zhang, D. P. Tsai, T. Bourouina, J. H. Teng, X. H. Zhang, H. C. Guo, H. Tanoto, T. Mei, G. Q. Lo, and D. L. Kwong, *Adv. Mater.* **23,** 1792 (2011).

[47]D. Bouyge, A. Crunteanu, M. Duran-Sindreu, A. Pothier, P. Blondy, J. Bonache, J. C. Orlianges, and F. Martin, *J. Opt.* **14,** 114001 (2012).

[48]H. Tao, A. C. Strikwerda, K. Fan, W. J. Padilla, X. Zhang, and R. D. Averitt, *J. Infrared Millim. Terahertz Waves* **32,** 580 (2011).

[49]W. M. Zhu, W. Zhang, R. F. Huang, S. K. Ting, G. Q. Lo, D. L. Kwong, and A. Q. Liu, in *IEEE MEMS 2013*, Taipei, TAIWAN, 2013, p. 725.

CHAPTER 5

FROM FLEXIBLE META-ATOM TO METAMATERIAL: A WEARABLE MICROWAVE META-SKIN WITH TUNABLE FREQUENCY SELECTIVE AND CLOAKING EFFECTS

A paper published in Scientific Reports

Siming Yang,[#] Peng Liu,[#] Mingda Yang, Qiugu Wang, Jiming Song, and Liang Dong

S. Y. and P. L. are co-first authors

5.1 Abstract

This paper reports a flexible metamaterial-based "skin" or meta-skin with tunable frequency selective and cloaking effects in microwave frequency regime. The meta-skin is composed of an array of liquid metallic split ring resonators (SRRs) embedded in a stretchable elastomer. When stretched, the meta-skin performs as a tunable frequency selective surface with a wide resonance frequency tuning range. When wrapped around a curved dielectric material, the meta-skin functions as a flexible "cloaking" surface to significantly suppress scattering from the surface of the dielectric material along different directions. We studied frequency responses of multilayer meta-skins to stretching in a planar direction and to changing the spacing between neighboring layers in vertical direction. We also investigated scattering suppression effect of the meta-skin coated on a finite-length dielectric rod in free space. This meta-skin technology will benefit many electromagnetic applications, such as frequency tuning, shielding, and scattering suppression.

5.2 Introduction

Metamaterials have attracted considerable attention due to their inaccessible electromagnetic (EM) properties that can be hardly found in natural materials. The unique

properties of negative permittivity, negative refractive index, and index close to zero[1-12], allow metamaterials to be employed in many emerging applications such as sub-wavelength resolution imaging[13,14], filtering[15], and cloaking[16-19]. Compared to conventional microwave filters, metamaterial-based counterparts have demonstrated the potential to obtain compact sub-wavelength size and left-handed behaviors. Different kinds of sub-wavelength resonators have been researched to achieve selective frequency responses. Among them, split ring resonator (SRR) is a widely proposed magnetic resonant structure[20,21]. While numerous research efforts have been made to push the operating wavelength of the SRR-based filters from the microwave to the visible region, the significance of the microwave filters would be tremendously increased if their response characteristics can be dynamically tuned. Therefore, a variety of frequency tuning mechanisms have been reported. Methods include changing unit cell's effective parameter by varying conductance or inductance[22-24], configuring constituent material by using phase changeable material as the constituent material[25-27], and altering geometry through distorting the structure or tilting the conducting elements[28-30].

Recently, inclusion of liquid metal as active components has opened up new ways to realize flexible electronics. By injecting liquid metal into a template, the metal can take on a specific shape to form stretchable electronic devices, such as electrical interconnectors[31], electrical probes[32], antennas[33-35], microelectrodes in microfluidic devices[36], switchable metamaterial microfluidic platforms[25], and artificial skin sensors[37]. We previously developed a stretchable single meta-atom in microwave regime, where eutectic gallium-indium (EGaIn: 75.5 % gallium and 24.5 % indium), a liquid metal at room temperature, was patterned as the SRR structure and embedded inside a stretchable silicone elastomer. As the shape of the

liquid SRR was changed via mechanical stretching, the split gap capacitance and the inductance of the resonator were adjusted[30].

In this paper we report a flexible microwave meta-skin and its frequency selective and cloaking effects. The meta-skin consists of an array of liquid metal SRR meta-atoms encased inside an elastomer. We demonstrate that by stretching multiple layers of the meta-skins along their surfaces in a planar direction and by changing the spacing between the meta-skin layers in a vertical direction, the meta-skins can perform as a high performance tunable frequency selective surface with a broad tuning range. Furthermore, the meta-skin is able to wrap an interaction object with any arbitrary shapes. We demonstrate that by wrapping it on a dielectric cylindrical rod, a significant scattering suppression or "cloaking" effect is observed. The scattered field from the dielectric rod at different angles is suppressed in a designed frequency region. Therefore, this meta-skin technology is different from traditional stealth technologies that often only reduce the backscattering, i.e., the power reflected back to a probing radar[38].

5.3 Design and Fabrication

Fig. 5.1a shows the structure of the proposed SRR array operated in X-Band regime. The device has the inner radius of a = 2.0 mm, the outer radius of b = 2.5 mm, the thickness of h = 0.5 mm, the gap of g = 1.0 mm, and the lattice constant of p = 7.5 mm. The SRR array is made of EGaIn and encased by a silicone elastomer (Ecoflex). The thickness of the Ecoflex is d = 1.45 mm. We conducted EM simulations to estimate a resonance frequency of the array using Ansys High Frequency Structure Simulator (HFSS) software. As shown in Fig. 5.1a, the SRR array is fixed in the x-y plane, and the magnetic field (**H**) is parallel to the z direction and penetrates through the SRRs, thus exciting a magnetic resonance. With the

aforementioned geometrical parameters, the simulated resonance frequency for the SRR array is 9.84 GHz. The surface current distribution at the resonance frequency is shown in Fig. 5.1a. By stretching the meta-skins (Fig. 5.1b), the lattice constant, the shape of the SRRs, and the mutual interaction between the resonators will be modulated. Accordingly, the resonance frequency of the meta-skins will be shifted.

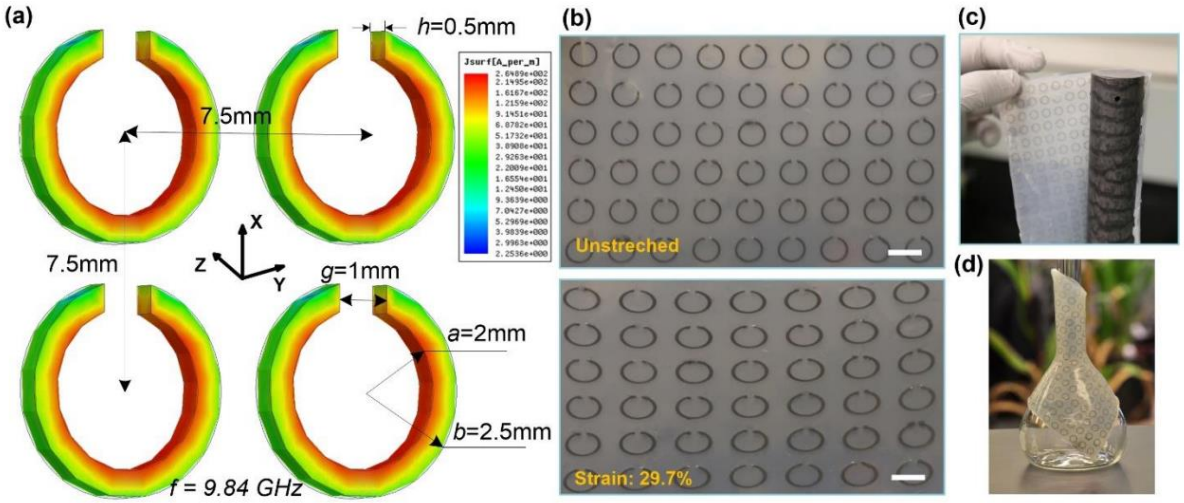

Fig. 5.1: (a) Geometry and simulated surface current distribution of the meta-skin. (b) Photos of the unstretched and stretched meta-skin. Scale bars represent 5 mm. (c) A photo of a 30.48 cm long, 3.175 cm diameter dielectric nylon rod wrapped by the meta-skin. (d) Flexibility demonstration with a glass flasks wearing the meta-skin.

We manufactured the proposed meta-skin with 225 identical SRR meta-atoms arranged in 15 columns and 15 rows. Fig. 5.2 shows the fabrication process flow. First, an aluminum master mold with the area of 14 cm × 14 cm was manufactured by using a high precision CNC milling machine. Subsequently, an Ecoflex layer L1 with the thickness of 800 µm was cast upon the master mold and then was fully cured on a hotplate at 60 ^{o}C for 30 mins. Simultaneously, another Ecoflex layer L2 was spin-coated on a 3 mm-thick poly(methyl methacrylate) or PMMA plate pretreated with a silane coupling agent. The spin-coated L2 was only partially cured at 50 ^{o}C for 1 min. After that, L1 was peeled off from the

master mold and then was adhered to L2, followed by baking on the hotplate at 150 ºC for 1 min. Thus, the SRR-shaped channels were formed in the elastomer. To inject liquid metal into the channels, an inlet and an outlet were mechanically punched at the two ends of each channel. After the liquid metal was manually injected into the channels by using a syringe (10 mL, Becton-Dickinson) with a needle (20 Gauge), the liquid metal residues were cleaned by a cotton swab dipped with a solution of hydrochloric acid (50%, v/v). Lastly, the whole device was immersed in a prepolymer solution of Ecoflex and then was fully cured at 80 ºC for 30 mins. The total thickness of the Ecoflex elastomer was 1.45 mm. The SRRs were located in nearly half the thickness of the elastomer.

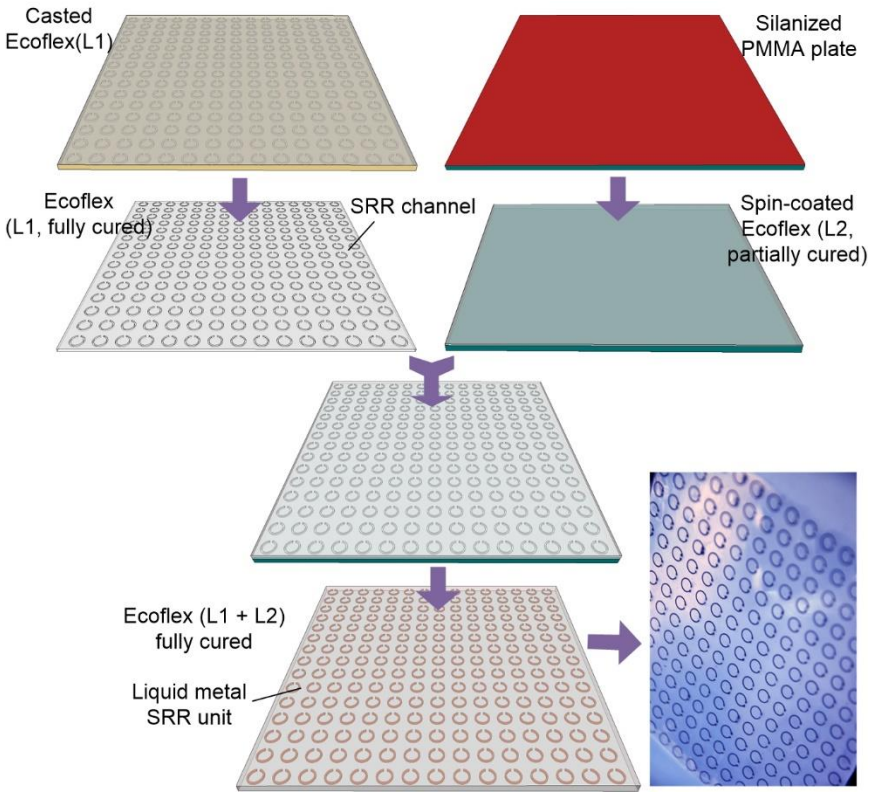

Fig. 5.2: Fabrication process flow for the meta-skin.

5.4 Results and Discussion

EM measurements were conducted in free space. Six of the meta-skins were stacked with the initial spacing d = 3 mm between neighboring meta-skins. A programmable vector network analyzer (VNA, Agilent E8364) was used to measure spectral responses of the sample. To generate a quasi-plane wave illumination, the meta-skins were placed between two horn antennas (one as a transmitter and the other as a receiver) within the far field regions. As the meta-skins were located in the electric field E-plane of the antenna, the magnetic field H could be coupled to the magnetic resonance from the current loop in the SRR (see inset of Fig.5.3).

Due to the stretchable feature of the meta-skin, the dimensions of the SRRs can be altered through stretching along different directions. Our previous research showed that the stretch-induced dimensional changes of the SRR can influence the equivalent inductance and capacitance of the SRR, thus shifting its resonance frequency[30]. In the present work, as the multilayers of the meta-skins were stretched along the wave propagation (k) direction with the stretch ratio of 0%, 15.9%, 29.7%, 36.4%, and 50%, the resonances of the meta-skins were observed at 9.84 GHz, 9.76 GHz, 9.47 GHz, 9.27 GHz, and 9.15 GHz, respectively. The measurement results are shown in Fig. 5.3 with dashed lines. To verify the measured results, an HFSS-based full wave EM simulation was carried out by applying the periodic boundary condition on the SRR units. The simulation results with different stretch ratios are shown in Fig. 5.3 with solid lines. The simulated and experimental results achieved a good agreement in the trend of shifting resonance frequency. The minor difference in the resonance frequency and bandwidth may be attributed to the accuracy of the model.

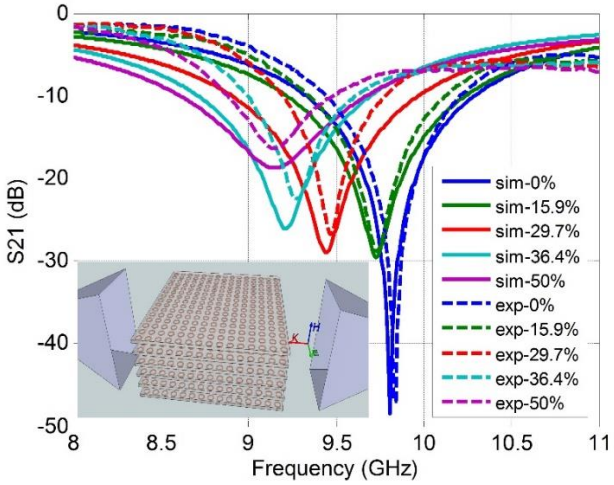

Fig. 5.3: Simulated and experimental transmittance spectra of the tunable 6-layer meta-skins. In this experiment the spacing between the neighboring layers is d = 3 mm. Inset shows a schematic for the setup.

By changing the spacing d between two neighboring layers, the resonance of the 6-layer meta-skins could also be tuned. Here, the spacing was defined by inserting foams (relative permittivity close to one). Fig. 5.4a and b shows the spectral responses of the meta-skins to different stretching levels for the spacing of d_1=13 mm and d_2=17 mm, respectively. As the meta-skins moved farther away from each other, the mutual inductance between the resonators in the neighboring layers reduced[39]. Consequently, an increase in resonance frequency of the meta-skins is expected. Indeed, for the unstretched sample, the resonance frequency was shifted from 9.84 GHz to 11.9 GHz as the vertical spacing increased from 3 mm to 13 mm. As we further increased *d* to 17 mm, the resonance frequency was shifted to 12.4 GHz. Similarly, by stretching the multilayer metal-skins along their surfaces in the horizontal direction, the resonance frequency was also observed to move towards lower frequencies. Therefore, by varying the spacing between the meta-skins in the vertical direction and stretching the metal-skins in a planar direction, the resonance frequency tuning range of the meta-skins can be largely broadened.

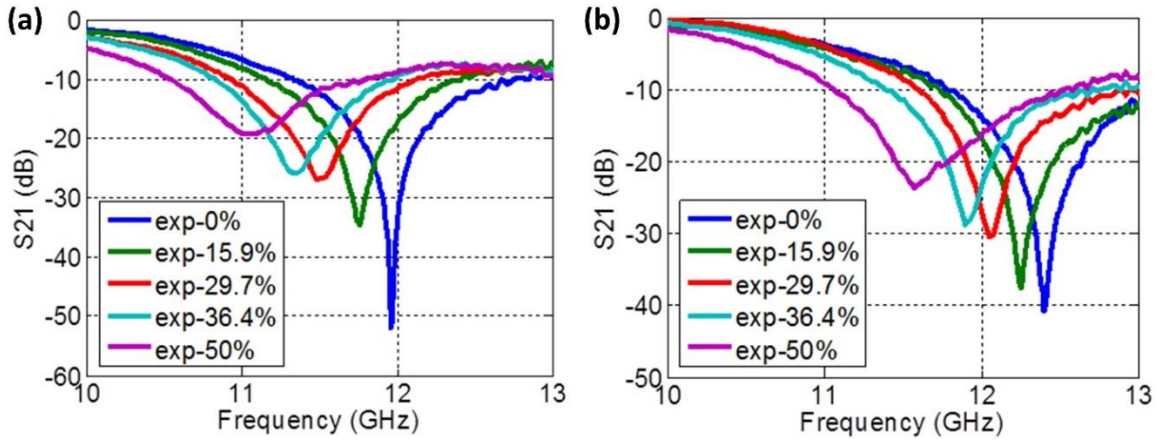

Fig. 5.4: Experimental transmittance spectra of the tunable 6-layer meta-skins as a function of mechanical stretch ratio for two different spacing between neighboring layers: d_1 = 13 mm (a) and d_2 = 17 mm (b).

The fully flexible nature of the meta-skin makes it possible to wrap on an interaction object with any arbitrary shapes. Here, we used a single layer of meta-skin to wrap on a 30.48 cm long, 3.175 cm diameter dielectric nylon rod (dielectric constant: $\varepsilon_r = 3.8$). We investigated how this wrapping material could influence the scattered field from the rod. The far-field measurement was thus conducted to measure scattering strength from a bare nylon rod, a nylon rod wrapped by a pure Ecoflex sheet, and a nylon rod wrapped by the meta-skin. In the measurement setup (Fig. 5.5), the sample hangs from a cotton thread at a designated origin to minimize unwanted scattering signals from the support constructs. The two horn antennas were placed at an equal distance of L = 80 cm from the sample. This ensured that the object was in the far-field region (according to the far-field condition $2D^2 / \lambda$, where D = 9.8 cm is the diagonal of the horn antenna and λ = 3 cm is estimated from the center operating frequency). The transmitter antenna was fixed during the measurement, while the receiver antenna was moved around the sample to receive scattering signals from different angles θ with respect to the transmitter. The two horn antennas were inset into the EM absorbing material to minimize the scattering from the background. The aforementioned

VNA was used to measure scattering parameters between the two antennas. The objective azimuthal bistatic measurements were conducted to obtain the s-parameter for further data processing.

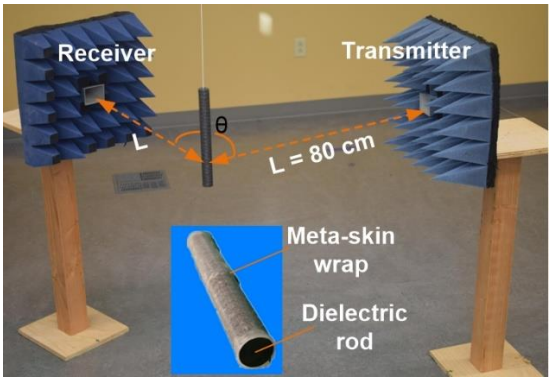

Fig.5.5: Experimental setup for measuring scattering from the meta-skin wrapped nylon rod (inset).

The scattered field was obtained by subtracting the incidence field ($S21\_i$) from the total field ($S21\_t$). This operation can not only derive the field scattered from the sample, but minimize clutters from background in the experiment. Two consecutive measurements were conducted. First, the sample was placed in the designated position and $S21\_t$ was measured. Then, the sample was removed and $S21\_i$ was recorded. The original scattering parameter for the scattered field can be expressed as $S21\_o(S(\omega)) = S21\_t - S21\_i$. It should be noted that because the real testing environment was complicated, the $S(\omega)$ derived from subtracting the incidence field from the total field may not entirely remove the clutter component from the objective signal. As shown in Fig. 5.6a, the spectral response of $S(\omega)$ (solid blue line) contains complex stray signal. To efficiently remove the clutters, we applied fast Fourier transform for the post processing, where a Gaussian window function ($G(\omega)$) was adopted due to its high resolution in time domain. By multiplying $G(\omega)$ by $S(\omega)$, a new signal in frequency domain was generated, denoted as $H(\omega)$. To reveal the signal

response in the time domain, an inverse fast Fourier transform (ifft(·)) was implemented over $H(\omega)$ to generate $h(t)$. Further, $h(t)$ was multiplied by a designated rectangular window function $w(t)$. In time domain, the signals from clutters were late arrived. Applying the rectangular window function in time domain allows filtering out the scattering from the clutters. The gated time domain signal is shown in Fig. 5.6b. Finally, the fast Fourier transform (fft(·)) was implemented over this processed time domain signal ($w(t) \cdot h(t)$), yielding $G(\omega) \cdot S'(\omega)$, where $S'(\omega)$ solely represents the interaction with the sample in the frequency domain. This entire process can be expressed

$$H(\omega) = G(\omega) \cdot S(\omega) \qquad (5.1.a)$$

$$h(t) = \text{ifft}(H(\omega)) \qquad (5.1.b)$$

$$S'(\omega) = \text{fft}(w(t) \cdot h(t))/G(\omega) \qquad (5.1.c)$$

Using Equation 5.1, we obtained the scattered field from the aforementioned three different samples. The processed scattered field for the sample covered by the meta-skin is shown in Fig. 5.6(a) with red solid line. Compared to $S(\omega)$, $S'(\omega)$ becomes smooth after the removal of the clutter from $S(\omega)$, while the scattering information still is contained.

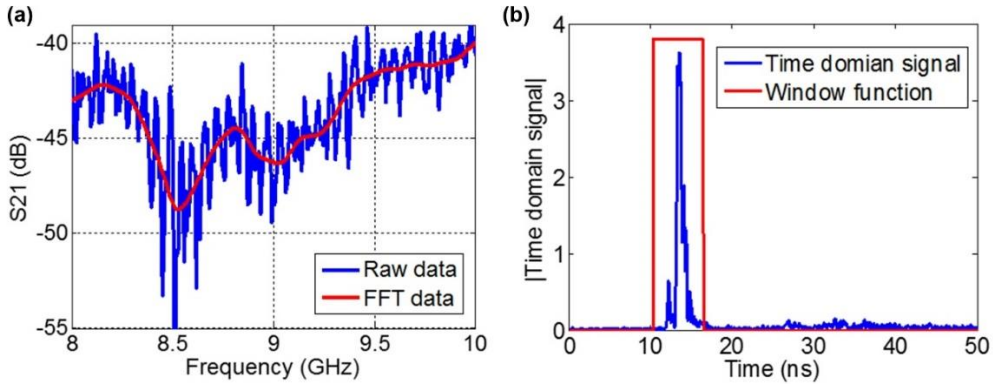

Fig. 5.6. (a) Raw and processed scattering gain for the meta-skin coated nylon rod at the angle of θ = 90°. (b) Gated time domain signal.

The post-processed scattering gains for the meta-skin covered, the polymer covered, and the uncovered rods are presented in Fig. 5.7a-e. The results show that the scattering gain from the meta-skin covered rod was significantly reduced in the frequency band from 8 GHz to 10 GHz at five different measurement angles $\theta = 37.5^o$, 45^o, 60^o, 90^o, and 105^o. Specifically, compared with the uncovered case, at $\theta = 37.5^o$ the meta-skin was able to suppress the scattering gain in over 33% of frequency band between 8-10 GHz. At other angles the suppression effect of the meta-skin is more significant and the scattering grain was suppressed in over 70% of the same frequency range. The largest suppression of 20 dB was found at around 9 GHz at 37.5^o. The overall scattering suppression effect of the meta-skin is illustrated by averaging the scattering gain with different angles (Fig. 5.7f). It is observed that the meta-skin was able to suppress the scattering gain by about 75% in the band of 8-10 GHz. The scattering suppression is mainly attributed to the cloaking effect of the embedded SRRs around the designed frequency, where the destructive interference between the resonance of the SRRs and the scattering from the dielectric rod occurred. We also noted that the scattering gain spectra of the meta-skin wrap in Fig. 5.7 do not have exactly the same resonance frequency as the transmittance spectra of the multilayer meta-skins in the unstretched state in Fig. 5.3. The factors below may be attributed to this observation: first, the scattering suppression gain was measured at different angles, which actually is angle-dependent due to different phases of multiple reflections and interactions over the interfaces; second, only one layer of the meta-skin was coated on the surface of the nylon rod with the dielectric constant of 3.8, while multiple layers of the meta-skins were used in the frequency selective surface application and spaced by foam with the dielectric constant of close to one.

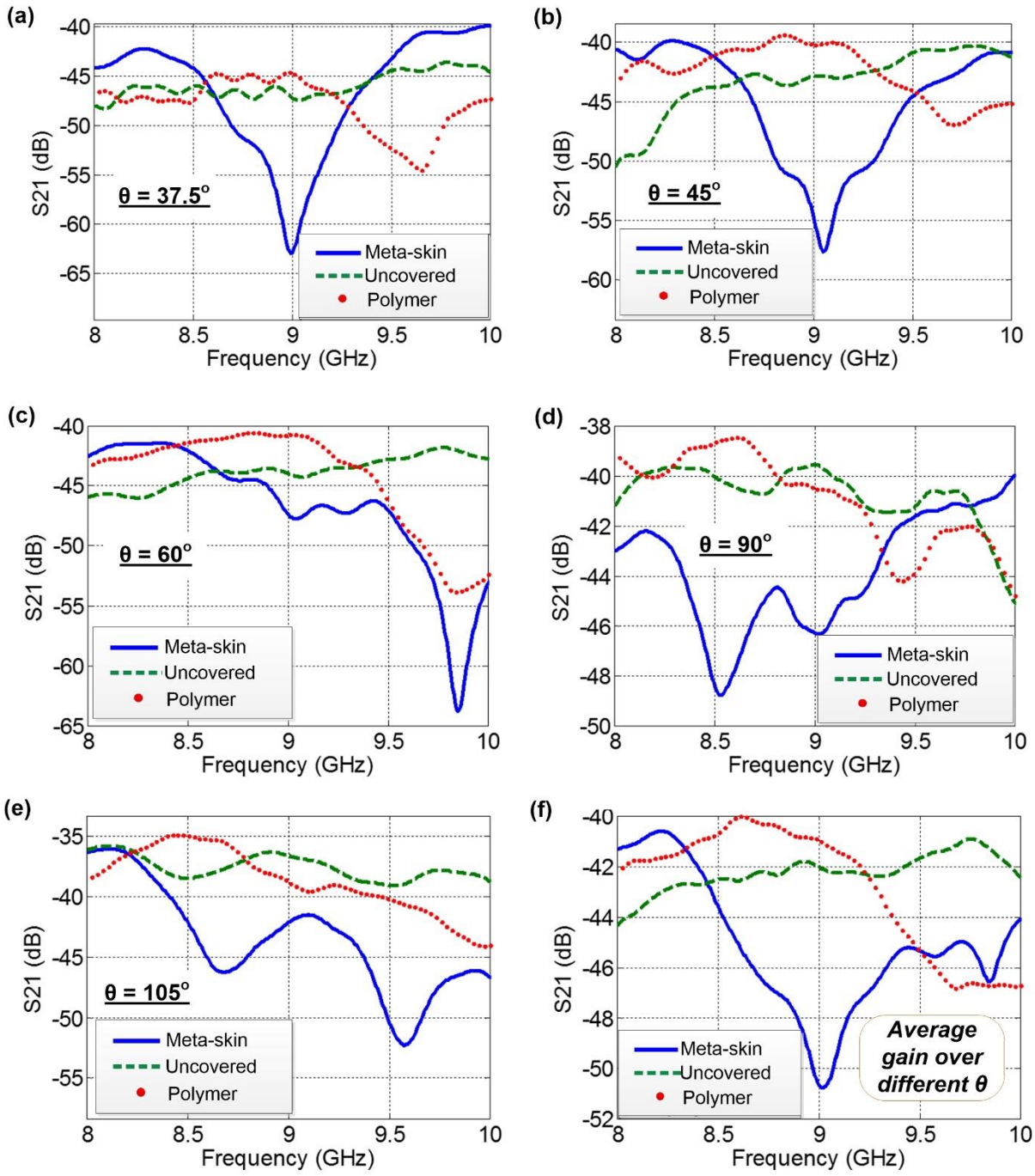

Fig. 5.7. Measured scattering gain for the bare dielectric rod (green - uncovered), the rod wrapped with the Ecoflex polymer (red - polymer), and the rod wrapped with the metal-skin (blue – meta-skin) at the angles of $\theta = 37.5^{o}$ (a), 45^{o} (b), 60^{o} (c), 90^{o} (d), and 105^{o} (e). The average scattering gain over the different angles is given in (f).

The whole meta-skin remained fully functional without fatigue or cracking after repeated measurements. This is because the liquid metal SRRs can flow and reshape responding to applied strains. Besides the single circular SRR, many other magnetic resonance structures may be used in the meta-skin setting to realize frequency selection and scattering suppression[40]. Furthermore, in addition to the magnetic resonators, liquid metal-based electric resonant structures, such as wires, can be integrated into the same elastomer. This will make it possible to achieve negative index for cloaking applications. Moreover, other different stretchable and flexible dielectric host media could be used to embed these liquid metal-based resonant structures. This will provide us with more flexibility to control loss tangent of the meta-skin. In the microwave frequency regime the dielectric losses are dominant and different substrate dielectric materials can affect the loss tangent. For higher frequencies, such as terahertz, as the ohmic losses become significant, other types of liquid metal or conducting materials are required to form the resonating units.

5.5 Conclusions

A flexible and wearable microwave meta-skin was developed by embedding an array of liquid metal SRRs into a highly flexible elastomer. We demonstrated the strong ability of the meta-skin to tune the resonance of the frequency selective surface and to suppress the scattering from the curved surface of a dielectric material along different directions. By combining the planar stretching and the vertical spacing, the resonance frequency of the multilayer meta-skins was tuned from 9.15 GHz to 12.38 GHz. By wrapping a finite-length dielectric rod with the meta-skin, the scattering from the surface of the rod was suppressed by about 75% in 8-10 GHz. It is believed that the present meta-skin technology will find many applications in EM frequency tuning, shielding, and scattering suppression.

5.6 References

1 Cai, W., Chettiar, U. K., Kildishev, A. V. & Shalaev, V. M. Optical cloaking with metamaterials. *Nat. Photonics* **1**, 224-227 (2007).

2 Chen, H.-T. *et al.* Experimental demonstration of frequency-agile terahertz metamaterials. *Nat. Photonics* **2**, 295-298 (2008).

3 Chen, H.-T. *et al.* Active terahertz metamaterial devices. *Nature* **444**, 597-600 (2006).

4 Hao, J. *et al.* High performance optical absorber based on a plasmonic metamaterial. *Appl. Phys. Lett.* **96**, 251104 (2010).

5 Jain, A., Tassin, P., Koschny, T. & Soukoulis, C. M. Large Quality Factor in Sheet Metamaterials Made from Dark Dielectric Meta-atoms. *Phys. Rev. Lett.* **112**, 117403 (2014).

6 Landy, N. I., Sajuyigbe, S., Mock, J. J., Smith, D. R. & Padilla, W. J. Perfect metamaterial absorber. *Phys. Rev. Lett.* **100**, 207402 (2008).

7 Pendry, J. B., Schurig, D. & Smith, D. R. Controlling electromagnetic fields. *Science* **312**, 1780-1782 (2006).

8 Pryce, I. M., Kelaita, Y. A., Aydin, K. & Atwater, H. A. Compliant Metamaterials for Resonantly Enhanced Infrared Absorption Spectroscopy and Refractive Index Sensing. *Acs Nano* **5**, 8167-8174 (2011).

9 Shin, D. *et al.* Broadband electromagnetic cloaking with smart metamaterials. *Nat. Commun.* **3**, 1213 (2012).

10 Smith, D. R., Vier, D. C., Koschny, T. & Soukoulis, C. M. Electromagnetic parameter retrieval from inhomogeneous metamaterials. *Phys. Rev. E* **71**, 036617 (2005).

11 Zhang, X. & Liu, Z. Superlenses to overcome the diffraction limit. *Nat. Mater.* **7**, 435-441 (2008).

12 Zhou, Q. *et al.* Ultrafast optical modulation of terahertz metamaterials. *J. Opt.* **13**, 125102 (2011).

13 Szabo, Z., Kiasat, Y. & Li, E. P. Subwavelength imaging with composite metamaterials. *J. Opt. Soc. Am. B* **31**, 1298-1307 (2014).

14 Zhu, J. *et al.* A holey-structured metamaterial for acoustic deep-subwavelength imaging. *Nat. Phys.* **7**, 52-55 (2011).

15 Gil, M., Bonache, J. & Martín, F. Metamaterial filters: A review. *Metamaterials* **2**, 186-197 (2008).

16 Burgos, S. P., de Waele, R., Polman, A. & Atwater, H. A. A single-layer wide-angle negative-index metamaterial at visible frequencies. *Nat. Mater.* **9**, 407-412 (2010).

17 Edwards, B., Alu, A., Silveirinha, M. G. & Engheta, N. Experimental Verification of Plasmonic Cloaking at Microwave Frequencies with Metamaterials. *Phys. Rev. Lett.***103**, 153901 (2009).

18 Landy, N. & Smith, D. R. A full-parameter unidirectional metamaterial cloak for microwaves. *Nat. Mater.* **12**, 25-28 (2013).

19 Schurig, D. *et al.* Metamaterial electromagnetic cloak at microwave frequencies. *Science* **314**, 977-980 (2006).

20 Falcone, F. *et al.* Babinet principle applied to the design of metasurfaces and metamaterials. *Phys. Rev. Lett.* **93**, 197401 (2004).

21 Pendry, J. B., Holden, A. J., Robbins, D. J. & Stewart, W. J. Magnetism from conductors and enhanced nonlinear phenomena. *IEEE Trans. Microw. Theory Techn.* **47**, 2075-2084 (1999).

22 Aydin, K. & Ozbay, E. Capacitor-loaded split ring resonators as tunable metamaterial components. *J. Appl. Phys.* **101**, 024911 (2007).

23 Gil, I., Bonache, J., Garcia-Garcia, J. & Martin, F. Tunable metamaterial transmission lines based on varactor-loaded split-ring resonators. *IEEE Trans. Microw. Theory Techn.* **54**, 2665-2674 (2006).

24 Wang, D. *et al.* Active left-handed material collaborated with microwave varactors. *Appl. Phys. Lett.* **91**, 164601 (2007).

25 Kasirga, T. S., Ertas, Y. N. & Bayindir, M. Microfluidics for reconfigurable electromagnetic metamaterials. *Appl. Phys. Lett.* **95**, 214102 (2009).

26 Poo, Y. *et al.* Experimental verification of a tunable left-handed material by bias magnetic fields. *Appl. Phys. Lett.* **96**, 161902 (2010).

27 Zhang, F. *et al.* Magnetic control of negative permeability metamaterials based on liquid crystals. *Appl. Phys. Lett.* **92**, 193104 (2008).

28 Lapine, M. *et al.* Structural tunability in metamaterials. *Appl. Phys. Lett.* **95**, 084105 (2009).

29 Lapine, M., Shadrivov, I. V., Powell, D. A. & Kivshar, Y. S. Magnetoelastic metamaterials. *Nat. Mater.* **11**, 30-33 (2012).

30 Liu, P. *et al.* Tunable meta-atom using liquid metal embedded in stretchable polymer. *J. Appl. Phys.* **118**, 014504 (2015).

31 Kim, H.-J., Son, C. & Ziaie, B. A multiaxial stretchable interconnect using liquid-alloy-filled elastomeric microchannels. *Appl. Phys. Lett.* **92**, 011904 (2008).

32 Chiechi, R. C., Weiss, E. A., Dickey, M. D. & Whitesides, G. M. Eutectic gallium-indium (EGaIn): A moldable liquid metal for electrical characterization of self-assembled monolayers. *Angew. Chem. Int. Ed.* **47**, 142-144 (2008).

33 Jobs, M., Hjort, K., Rydberg, A. & Wu, Z. A Tunable Spherical Cap Microfluidic Electrically Small Antenna. *Small* **9**, 3230-3234 (2013).

34 Kubo, M. *et al.* Stretchable Microfluidic Radiofrequency Antennas. *Adv. Mater.* **22**, 2749-2752 (2010).

35 Wang, M., Trlica, C., Khan, M. R., Dickey, M. D. & Adams, J. J. A reconfigurable liquid metal antenna driven by electrochemically controlled capillarity. *J. Appl. Phys.* **117**, 194901 (2015).

36 So, J.-H. & Dickey, M. D. Inherently aligned microfluidic electrodes composed of liquid metal. *Lab Chip* **11**, 905-911 (2011).

37 Park, Y.-L., Chen, B.-R. & Wood, R. J. Design and Fabrication of Soft Artificial Skin Using Embedded Microchannels and Liquid Conductors. *IEEE Sensors J.* **12**, 2711-2718 (2012).

38 Ufimtsev, P. Y. New insight into the classical Macdonald physical optics approximation. *IEEE Antennas Propag. Mag.* **50**, 11-20 (2008).

39 Shadrivov, I. V., Powell, D. A., Morrison, S. K., Kivshar, Y. S. & Milford, G. N. Scattering of electromagnetic waves in metamaterial superlattices. *Appl. Phys. Lett.* **90**, 201919 (2007).

40 Aydin, K. *et al.* Investigation of magnetic resonances for different split-ring resonator parameters and designs. *New J. Phys.* **7**, 168 (2005).

5.7 Acknowledgement

The work was partially supported by National Science Foundation under the Grant No. ECCS-0954765, Iowa Department of Transportation, Iowa Highway Research Board, and China Scholarship Council.

CHAPTER 6

CONCLUSION AND FUTURE ASPECTS

6.1 Summary and Conclusion

In this dissertation, the background of microfluidic platform technology is introduced. The advantages of integrating microfluidic platform technologies with multiple technologies, especially electronics and optics, are discussed. The ideas behind two important fused technology, optofluidic and electrofluidic are illustrated. Further, a comprehensive literature review of current cutting-edge trends about these two technologies is illustrated in Chapter 1. Each technology is divided to two categories depending upon the direction of fusion. Many inspiring pioneer work are presented with their applications and integration advantages. As a result, challenges and opportunities are discovered. While for different applications, different approaches may be adopted even for solving the same problem. Thus we dedicated ourselves to application-orientated technique polishing and improvement. For different applications, we will consider cons and pros for each integrated technology and make the right choice in order to make the full use of those chosen technologies.

The first application we studied is measuring muscular force of microscopic nematodes. The current technologies have some disadvantages such as requiring a high-resolution microscope, or need a complicated strain gauge force sensor. Our approach is to integrate a relatively simple design with fiber optics into an elaborately designed microfluidic channel. Physical contacts between a moving nematodes and the single-mode fiber (SMF) cantilever at the detection points bent the SMF cantilever, reducing light coupling from the SMF to the receiving multi-mode fiber. Thus, the SMF cantilever transduced the normal

force of the worm into optical transmission signals. The ability of the present device can benefit and advance the current whole animal assays. The technology will have the potential to provide a more direct measure of the effectiveness of drugs by qualifying the muscular force of parasitic nematode species.

The second application we investigated is tracking the locomotion of microscopic nematodes. The mostly common observation technology is utilizing high resolution microscope with a decent algorithm to post process the images. Almost all existing on chip technologies essentially use optical effects such as shadow and interference patterns due to the presence of microorganism and thus require a sophisticated imaging sensor chip, along with a light source. We present a lens-less, image-sensor-less approach for real-time on-chip monitoring the locomotion of the nematodes. 24 × 24 detection units were formed by fabricating two identical arrays of micro electrodes orthogonally on two sides of a microfluidic chamber. We found that as a worm moved closer to the detection unit, the electrical resistance of this unit increased. Our approach overcomes the limited field of view of conventional optical microscopy, with relatively low cost, good spatial resolution and high portability.

The third application is to fabricate a tunable meta-atom towards to EM metamaterial. The existing tuning technology usually relies on changing effective circuit parameters via incorporating variable capacitors and switches; varying constituent material property by using liquid crystal; or changing geometry using MEMS technology. However, almost all the technologies require complicated tuning mechanism and the fabricated metamaterial is not flexible enough and not able to withstand large deformation. Our approach is to incorporate a SRR shaped microfluidic channel made of super flexible elastomer and inject the channel

with liquid metal. The novel stretchable SRR-based meta-atom is capable of continuous tuning its EM response over more than 70% of the whole X-band frequency range via simple mechanical stretching. The metamaterials made of such meta-atom potential will find many applications in wearable EM coatings and devices.

As an extension of the stretchable meta-atom, we developed a flexible and wearable microwave meta-skin. We demonstrated the strong ability of the meta-skin to tune the resonance of the frequency selective surface and to suppress the scattering from the curved surface of a dielectric material along different directions. It is believed that the present meta-skin technology will find many applications in EM frequency tuning, shielding, and scattering suppression.

In summary, as emerging technologies, optofluidics and electrofludics are still newly developing areas. Efforts are required to support a future technical revolution from researchers from different backgrounds, and in particular, from their parent fields: microfluidics, optics and electronics.

6.2 Future Aspects

The general outlook of the integration of microfluidics platform technology with optics and electronics including improving integration, reducing the cost, effective fabrication and increase applicability. I will detail the future aspects for different applications presented in this dissertation.

For fiber-optic microfluidic device, we can further increase the integration and miniaturize the device by using on chip waveguide directly fabricated along with the microfluidic channel. The detection resolution and reliability can be further improved by increasing the amount of detection points. For micro-electro-fluidic grids device, with

MEMS-IC integration, we can replace the commercial FPGA board with a customized IC control chip and thus, improve the portability. We can further increase the resolution by reducing the width of microelectrodes. For tunable meta-atom, we can utilize some better fabrication techniques such as the 3D-printing or direct writing I reviewed in section 1.2.4. With those advanced fabrication technique, the liquid metal waste can be reduced and the processing time can be dramatically reduced especially for large-scale meta-skin device. And with the demonstration of the meta-atom and meta-skin, further miniaturization of the device can push the operating wavelength of the SRR-based filters from the microwave to the visible region.

APPENDIX

SUPPORTING INFORMATION FOR

TUNABLE META-ATOM USING LIQUID METAL

EMBEDDED IN STRETCHABLE POLYMER

The capacitance across the SRR gap region is given by

$$C_{gap} = \varepsilon_o \varepsilon_r \frac{wh}{g} \qquad \text{(A.1)}$$

where g is the gap distance, and w and h are the width and thickness, respectively, of the split. The main geometric parameters of the SRR are denoted in Figure 4.1a.

The self-inductance of a circular ring is given by

$$L_0 = 4\pi a \left[\ln\left(\frac{8a}{h}\right) - 2\right] \qquad \text{(A.2)}$$

where a and h are the inner radius and cross-section thickness, respectively, of the SRR.

After stretched, the circular SRR becomes an elliptical SRR. The self-inductance of the elliptical SRR is given by

$$L_e = 8E(\Omega)r_a\left[\ln\left(\frac{16E(\Omega)r_a}{\pi h}\right) - 2 - 0.4375\Omega^2 - 0.14454\Omega^4 - \cdots\right] \qquad \text{(A.3)}$$

where h is the thickness of the cross section of the split, and $E(\Omega)r_a$ is the product of complete elliptical integral of the second kind and the semi-major axis. $E(\Omega)r_a = \int_0^{\pi/2} \sqrt{1-(\Omega sin\theta)^2}\, d\theta$, where θ is the eccentric angle of point on ellipse and $\Omega = ({r_a}^2 - {r_b}^2)/({r_a}^2 + {r_b}^2)$ where r_a and r_b are the semi-major and semi-minor axis of the elliptical SRR, respectively.

Figure S1, Figure S2 and Figure S3 show the measured transmittance and reflectance spectrum of proposed stretchable meta-atom for all three configurations (Figure 4.4, 4.5 and 4.6) correspondingly.

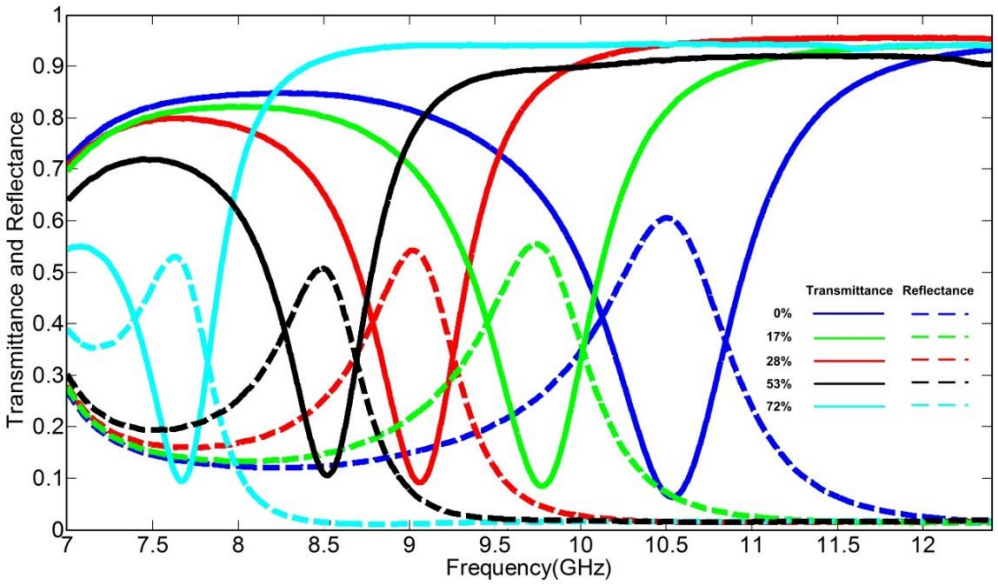

Figure S1. Measured transmittance and reflectance spectrum for a SRR meta-atom of third configuration at different stretching ratios of 0, 17%, 28%, 53%, and 72%

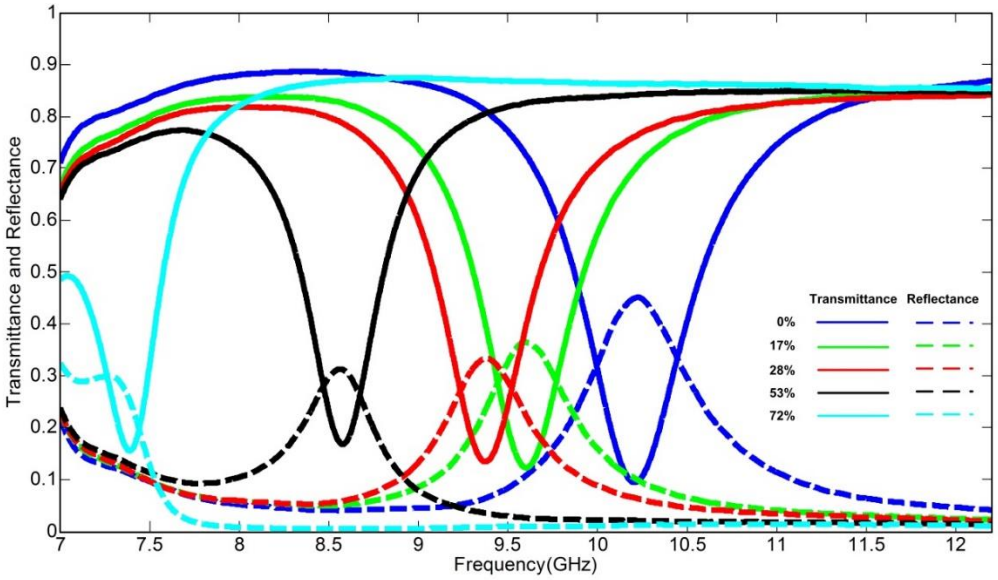

Figure S2. Measured transmittance and reflectance spectrum for a SRR meta-atom of second configuration at different stretching ratios of 0, 17%, 28%, 53%, and 72%

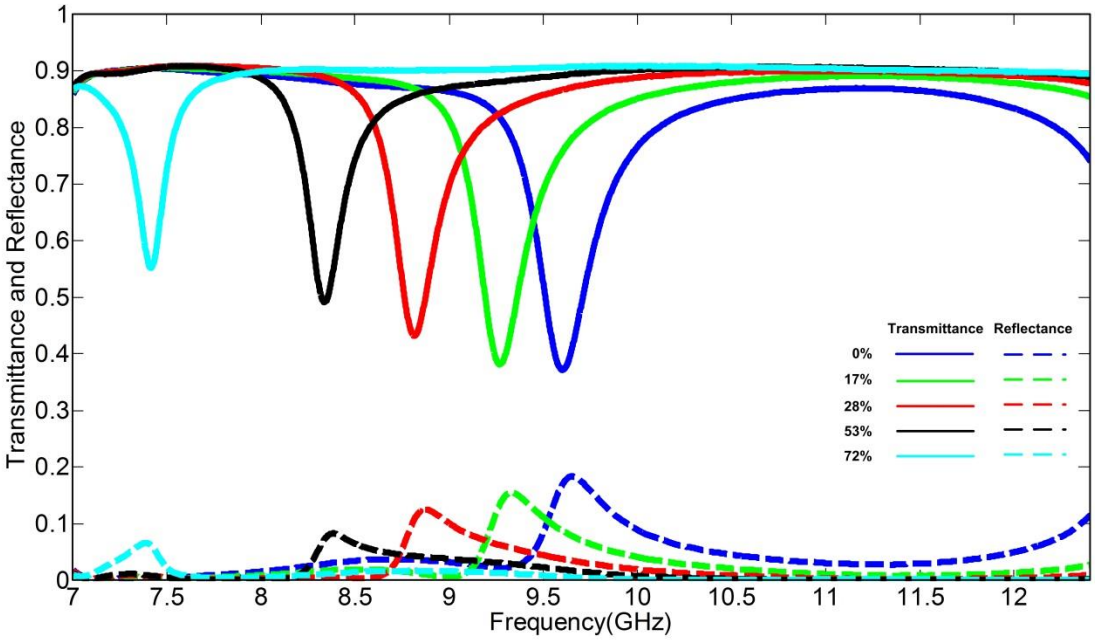

Figure S3. Measured transmittance and reflectance spectrum for a SRR meta-atom of third configuration at different stretching ratios of 0, 17%, 28%, 53%, and 72%